Inversion of seismic AVA data for porosity and saturation

Brikt Apeland

Thesis for the degree
Master of Science

Department of Earth Science

University of Bergen

27th June 2013

Abstract

Rock physics serves as the link between reservoir parameters and the effective elastic reservoir properties, and Amplitude Variation with Angle (AVA) modelling serves as the link between elastic properties and reflection coefficients. AVA inversion is one of the techniques that is being used to estimate subsurface physical parameters such as saturation and porosity. A non-interacting compliance model is used to find the effective elastic parameters of the dry rock. Woods equation is then used along with Gassman-Biot theory to calculate the effective elastic parameters of a fluid saturated rock. This information is used as input for AVA modelling from elastic properties to reflection coefficients using the Zoeppritz equations or Aki-Richards approximation.

The modelling error introduced by Aki-Richards approximation is investigated for two-layer models that differ according to reservoir models with varying saturations and porosities. Further, the effect of this modelling error is investigated in a one-step unbiased inversion algorithm from AVA data to saturation and porosity. Also, the implications of assuming constant crack density in a spatial varying reservoir is investigated. Inversion tests indicate that Aki-Richards approximation may give valid porosity estimates in a less computationally expensive manner than the Zoeppritz equations.

A time-continuous formulation of Aki-Richards approximation is adopted for AVA modelling from a stratified earth model with a reservoir section. It is used along with the rock physics model in two-step inversion algorithms. The first step is from AVA data to the elastic properties of the stratified earth models and the second step is from effective elastic reservoir properties to saturation and porosity. Well logs may serve as additional information as prior models into the inversion algorithms. Two-step inversion algorithms with prior models within the framework of both a frequentist and Bayesian interpretation of probability theory are demonstrated.

Acknowledgements

First and foremost, I would like to express my gratitude towards my supervisor, Professor Morten Jakobsen, and my co-supervisor Principal Researcher Trond Mannseth. Thanks to Morten for introducing me to rock physics, AVA modelling and inversion. His enthusiasm, patience and excellent guidance has been greatly appreciated. Thanks to Trond for introducing me to inversion theory and good discussions about its application.

I also wish to acknowledge all the professors at the Department of Earth Science that taught me courses during my studies at the University of Bergen. They have always been willing to share their time and knowledge. I especially wish to thank Associate Professor Henk Keers for the guidance he has given me on programming in Matlab during my master thesis. I am also happy that I have been given the opportunity to work as student assistant for Associate Professor Mathilde Sørensen, Professor Harald Walderhaug, Professor Ritske Huismans and Professor Patience Cowie.

Further, I would like to thank my fellow students that made my time as a student both memorable and very enjoyable. I especially want to thank the MSc students in geophysics at my study hall for helpful discussions and advice.

Finally, I wish to thank my parents for moral support and helpful advice. They have been a great source of encouragement throughout my time as a student.

Contents

List of Tables

List of Figures

Chapter 1

Introduction

Acquisition of reflection seismics is extensively used in exploration for hydrocarbons in clastic depositional settings. A basic procedure uses seismic sources, such as explosives, vibrators and air guns, to generate seismic waves and record the propagated signal in order to build an image of the subsurface. The recorded seismic signal shows the variation in amplitude and phase as a function of source-receiver distance and two-way travel-time. Exploration for hydrocarbons is increasingly challenging and requires more expensive investments. Also, it is a paradox that we know very little about a reservoir during the initial phases when important production plans and investment plans are made. Seismic amplitudes and the degree to which they change with offset, amplitude variation with offset (AVO), have proven substantial risk reduction than using structural information alone. If the seismic data is mapped into angle of incidence, the method is called amplitude variation with angle (AVA). Detailed investigation of the amplitude of reflections on a seismic section can provide important information about the reservoir properties. The presence of gas or oil in a pore space of rocks lowers the velocity as compared to water for instance.

Acquiring estimates of saturation and porosity can enable us to distinguish between commercial and non-commercial quantities of hydrocarbons, or optimize well locations and production plans prior to production. Advances in seismic acquisition and processing enables us to quantify such reservoir properties with increasing accuracy. Amplitude versus angle (AVA) inversion is a quantitative seismic pre-stack technique. The aim is to physically explain the amplitude variation with angle, or equivalently offset, through rock properties. A prerequisite is that sufficient pre-processing has been performed on the seismic sections such that seismic amplitudes can be assumed to represent reflection coefficients. There are three important aspects of a processing sequence tailored for AVA inversion Yilmaz (2001). The relative amplitudes of the seismic data must be preserved throughout the analysis in order to recognize amplitude variation with angle related to lithology and fluid content. Second, the processing sequence must retain the broadest possible signal band in the data with a flat spectrum within the passband. Finally, the pre-stack amplitude inversion need to be related to reflection events in their migrated position.

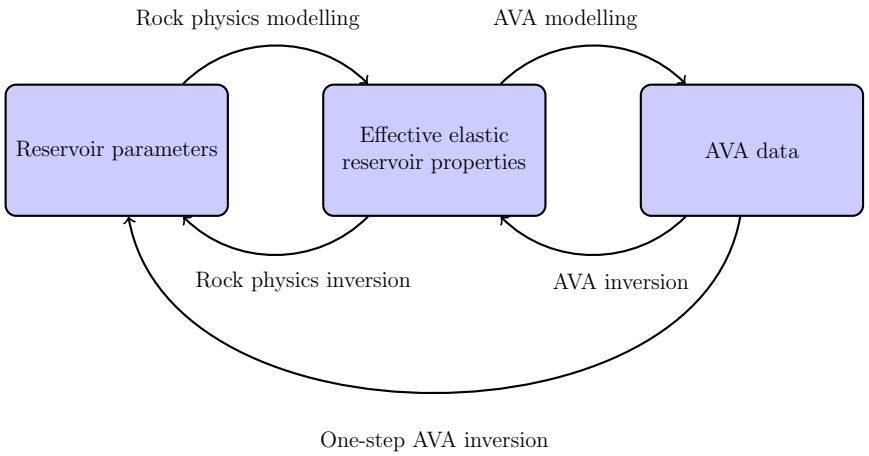

Figure 1.1: Schematic illustration of the relations between AVA data, effective elastic reservoir properties and reservoir parameters.

The Zoeppritz equations and its approximations provide a link between the effective elastic reservoir properties and the amplitudes of transmitted and reflected waves at a given interface. A reservoir model can in turn provide a link between effective elastic properties and reservoir parameters such as saturation and porosity. Using these physical models, one can construct an inverse problem that relates the observed reflection coefficients to accurate information about the effective elastic properties and the corresponding saturation and porosity. The inversion may either be done as a two-step procedure, from AVA data to effective elastic reservoir properties and on to saturation and porosity, or as a one-step procedure from AVA data directly to saturation and porosity.

This thesis is organized as follows:

Chapter 2 gives an introduction to the rock physics principles that are used in the forward modelling. A porous sandstone is modelled with a basis in the non-interacting compliance approachHornby et al. (1994) and the Gassmann-Biot theoryBiot (1956); Gassmann (1951). The model is then calibrated to wells from the Oseberg fieldLarsen (2010). A gas and water saturated reservoir rock and an oil and water saturated rock is then modelled for varying water saturations and porosities.

Chapter 3 gives an introduction to the principles that are used for forward modelling of seismic amplitude versus angle. The Zoeppritz equations and the Aki-Richards linearized approximation to the reflection coefficients are presented. Following this they are compared and their accuracy in forward modelling is investigated. This is done for reservoir models, for either a gas-water pore fluid or an oil-water pore fluid, with varying saturations and porosities for a fixed overburden.

Chapter 4 gives a short introduction to nonlinear and linearized discrete inversion theory. The various inversion algorithms that are used later on are discussed.

Chapter 5 demonstrates how the modelling error in Aki-Richards approximation effects the inversion for water saturation and porosity. The forward modelling for PP-reflection coefficients is either done with the Zoeppritz equations or Aki-Richards approximation. 'Real' AVA data is then synthesized

using the Zoeppritz equations. Following this, the inverse problem is solved in a one-step inversion procedure directly from AVA data to water saturation and porosity. Also, the effects of assuming constant crack density in a reservoir with spatial variability is investigated

Chapter 6 introduces two-step AVA inversion algorithms. Seismic AVA data is first inverted for stratified elastic earth models by linearized inversion algorithms. The elastic properties of the reservoir sections in the inverted elastic earth models are then used for rock physics inversion for water saturation and porosity. A second aim is to compare classical and Bayesian two-step inversion algorithms.

Chapter 7 summarizes the most important conclusions and discuss the possibilities for future work.

Chapter 2

Rock physics

2.1 Effective properties of dry rocks

Rocks can be described by parameters such as the properties of the individual elements of the composite, the volume fractions of the components, the geometric details of the shapes and spatial distributions of components at the micro-scale. They are as such inherently heterogenous materials to some extent. However, the macroscopic physical parameters are controlled by the average of the microscopic parameters. A statistically homogenous medium is heterogenous on a small scale, but appears homogenous on a larger scale. It is possible to describe the physical response of such a statistically homogenous medium in terms of effective properties. The effective properties are introduced by replacing the real discontinuous medium by an effective continuous medium. There are a number of approaches that can be utilized according to the assumptions that are appropriate. They include the T-matrix approach (Jakobsen et al., 2003), Self consistent method (Berryman, 1980; Budansky, 1965; Hornby et al., 1994) which includes scattering between inclusions, and differential medium theory (Bruggeman, 1935; Hornby et al., 1994). An overview of different approaches for averaging is given by Hudson (1991).

The non-interacting compliance approach (Hornby et al., 1994) for the effective elastic properties is based upon the continuum hypothesis and an averaging process. The continuum hypothesis gives a macroscopic description of a volume of heterogenous material that is small compared to the length scale of interest and large compared to the microstructure. Physical quantities like mass and momentum inside the volume can be considered as being continuously distributed over the entire volume, V. The local stress tensor at position $\mathbf{x}$ is denoted by $\boldsymbol{\sigma}_{\mathrm{ij}}(\mathbf{x})$ and the average static stress field within V is given by Hill (1963):

$$\bar{\boldsymbol{\sigma}}_{\mathrm{ij}}(\mathbf{x}) = \frac{1}{V}\int_{V} \boldsymbol{\sigma}_{\mathrm{ij}} dV \tag{2.1}$$

and the average strain field, $\boldsymbol{\epsilon}$:

$$\bar{\boldsymbol{\epsilon}}_{\mathrm{ij}}(\mathbf{x}) = \frac{1}{V}\int_V \boldsymbol{\epsilon}_{\mathrm{ij}} dV \tag{2.2}$$

Hooke's law for the effective elastic medium is defined by introducing an effective stiffness tensor, $\mathbf{c}^*$, or equivalently an effective compliance tensor, $\mathbf{s}^*$ (Hornby et al., 1994). The relation between average stress (2.1) and strain (2.2) can thus be written as:

$$\bar{\boldsymbol{\sigma}} = \mathbf{c}^*\bar{\boldsymbol{\epsilon}} \tag{2.3}$$

$$\bar{\boldsymbol{\epsilon}} = \mathbf{s}^*\bar{\boldsymbol{\sigma}} \tag{2.4}$$

The effective stiffness and compliance does not vary on loading in a linear deformation regime. A composite material of several homogenous phases embedded in a matrix material in such a regime has average stress and average strain relations:

$$\bar{\boldsymbol{\sigma}} = \sum_{n=0}^{N} \mathrm{v}_n \boldsymbol{\sigma}^{(n)} \tag{2.5}$$

$$\bar{\boldsymbol{\epsilon}} = \sum_{n=0}^{N} \mathrm{v}_n \boldsymbol{\epsilon}^{(n)} \tag{2.6}$$

$\mathrm{v_n}$ is the relative volume constituent of the n'th phase, $\boldsymbol{\sigma}^{(n)}$ is the stress imposed on the n' th phase and $\boldsymbol{\epsilon}^{(n)}$ is the strain in the n'th phase. Applying Hooke's law on eq.(2.5) yields:

$$\bar{\boldsymbol{\sigma}} = \sum_{n=0}^{N} \mathrm{v}_n \mathbf{c}^{(\mathrm{n})} \boldsymbol{\epsilon}^{(\mathrm{n})} \tag{2.7}$$

where $\mathbf{c}^{(\mathrm{n})}$ is the stiffness tensor of the n'th phase. The average strain over the matrix material can be eliminated by multiplying eq.(2.6) by the matrix stiffness tensor, $\mathbf{c}^{(0)}$, and subtracting it from eq.(2.7):

$$\left(\mathbf{I} - \mathbf{c}^{(0)}\mathbf{s}^*\right)\bar{\boldsymbol{\sigma}} = \sum_{n=1}^{N} \mathrm{v}_n \left(\mathbf{c}^{(\mathrm{n})} - \mathbf{c}^{(0)}\right)\boldsymbol{\epsilon}^{(\mathrm{n})} \tag{2.8}$$

where $\mathbf{I}$ is the fourth order identity tensor. Further, it is assumed that there exists a tensor, $\mathbf{K}^{(\mathrm{n})}$, that relates the imposed stress, $\bar{\boldsymbol{\sigma}}$, linearly to the average strain in each phase, $\boldsymbol{\epsilon}^{(\mathrm{n})} = \mathbf{K}^{(\mathrm{n})}\bar{\boldsymbol{\sigma}}$ (Hudson and Knopoff, 1989). This expression may in turn be substituted into eq.(2.8) in order to eliminate the strain in each phase:

$$\left(\mathbf{I} - \mathbf{c}^{(0)}\mathbf{s}^*\right)\bar{\boldsymbol{\sigma}} = \sum_{n=1}^{N} \mathrm{v}_n \left(\mathbf{c}^{(\mathrm{n})} - \mathbf{c}^{(0)}\right)\mathbf{K}^{(\mathrm{n})}\bar{\boldsymbol{\sigma}} \tag{2.9}$$

The effective matrix compliance is the inverse of the effective matrix stiffness, $\mathbf{s}^{(0)}$, such that $\mathbf{s}^{(0)}\mathbf{c}^{(0)} = \mathbf{I}$. An expression for the effective compliance may be obtained by multiplying eq.(2.9) by the effective

matrix compliance and eliminating the average stress:

$$\mathbf{s}^* = \mathbf{s}^{(0)} - \sum_{n=1}^{N} v_n \left(\mathbf{s}^{(0)}\mathbf{c}^{(\mathrm{n})} - \mathbf{I}\right) \mathbf{K}^{(\mathrm{n})} \tag{2.10}$$

Eshelby (1957) defined the K-tensor for an imposed stress field for an ellipsoidal inclusion in an infinite homogenous matrix as:

$$\mathbf{K}^{(\mathrm{n})} = \left[\mathbf{c}^{(0)}\left(\mathbf{I} + \mathbf{G}^{(\mathrm{n})}\left(\mathbf{c}^{(\mathrm{n})} - \mathbf{c}^{(0)}\right)\right)\right]^{-1} \tag{2.11}$$

where $\mathbf{G}^{(\mathrm{n})}$ is Green's tensor, $\mathbf{G}^{(\mathrm{n})} = -\mathbf{s}^{(\mathrm{n})}\mathbf{s}^{(0)}$, and $\mathbf{s}^{(\mathrm{n})}$ is a tensor for an ellipsoid inclusion. The components of $\mathbf{s}^{(\mathrm{n})}$ can be calculated analytically for an isotropic matrix material (Torquato, 2002). The resulting $\mathbf{K}^{(\mathrm{n})}$-tensor will be valid for fully aligned non-interacting inclusions. It is necessary to average over a orientation distribution function to make it applicable to isotropic materials. The isotropic average of $\mathbf{K}^{(\mathrm{n})}$ can be expressed in terms of Lames parameters (Sayers, 1994):

$$\begin{aligned} 15\lambda &= \mathrm{k}_{11} + \mathrm{k}_{33} + 5\mathrm{k}_{12} + 8\mathrm{k}_{13} - 4\mathrm{k}_{44} \\ 30\mu &= 7\mathrm{k}_{11} + 2\mathrm{k}_{33} - 5\mathrm{k}_{12} - 4\mathrm{k}_{13} + 12\mathrm{k}_{44} \end{aligned} \tag{2.12}$$

It is straightforward to calculate the corresponding isotropic $\mathbf{K}^{(\mathrm{n})}$-tensor from the Lames parameters (2.12).

When a rock is loaded under an increment of compression, an increment of pore-pressure change is induced, which resists compression and therefore stiffens the rock. The cavities that are modelled by the non-interacting compliance approach are isolated with respect to flow. Fluid inclusions would simulate very-high-frequency saturated rock behavior that is appropriate to ultrasonic laboratory conditions. However, for the lower frequencies used in seismic exploration, there is time for wave-induced pore-pressure increments to flow and equilibrate. Thus, it is more appropriate to use the non-interacting compliance approach to find the effective elastic properties of a dry rock as a starting pointMavko et al. (2003). Empty pores may be described by a setting a vanishing inclusion stiffness, $\mathbf{c}^{(\mathrm{n})} = 0$, in eq.(2.10). The effective dry bulk, $\mathrm{K_d}$ and shear, μ_d, moduli can be written in terms of the elements in the effective stiffness matrix, which is the inverse of the effective compliance matrix (2.10):

$$\mathrm{K_d} = c_{44}^* \qquad\qquad \mu_\mathrm{d} = c_{11}^* - \frac{4}{3}c_{44}^* \tag{2.13}$$

2.2 The effect of saturation on elastic properties

The Gassmann-Biot theory (Biot, 1956; Gassmann, 1951) is the most widely used model to describe the saturated rock properties that is valid for low frequencies from the dry rock properties. It assumes a homogenous matrix and fluid, that the pores are fully saturated and connected, and that there is statistical isotropy of the pore space such that the saturated medium is isotropic. The effective bulk

under these assumptions is given by:

$$\mathrm{K}^* = \mathrm{K_d} + \frac{\alpha^2}{\frac{\phi}{\mathrm{K}_f} + \frac{(\alpha-\phi)}{\mathrm{K}_m}} \tag{2.14}$$

$\mathrm{K_m}$ is the effective bulk modulus of the matrix material, ϕ is the porosity, $\mathrm{K_f}$ is the effective bulk modulus of the fluid, $\mathrm{K_d}$ is the effective bulk modulus of the dry rock, K^* is the effective bulk modulus of the saturated rock and $\alpha = 1 - \frac{\mathrm{K_d}}{\mathrm{K_m}}$. The effective shear modulus, μ^*, will not change from the dry shear modulus, μ_d, since fluids do not have any shear resistance:

$$\mu^* = \mu_d \tag{2.15}$$

The effective fluid modulus of a homogenous mix of several phases can be regarded as an analogue to resistances in series by the equation of Wood (1955):

$$\frac{1}{\mathrm{K_f}} = \sum_{\mathrm{i}=1}^{N} \frac{\mathrm{S_i}}{\mathrm{K_i}} \tag{2.16}$$

where $\mathrm{S_i}$ is the saturation and $\mathrm{K_i}$ is the bulk modulus of the i'th fluid phase. The saturation is given as a fraction of the total fluid volume: $\sum_{\mathrm{i}=1}^{N} \mathrm{S_i} = 1$, and it will need to be equal to the total pore volume for it to be compatible with the Gassmann-Biot theory. The effective fluid density, ρ_f, can be regarded as an analogue to resistances in parallel (Guéguen and Palciauskas, 1994):

$$\rho_\mathrm{f} = \sum_{\mathrm{i}=1}^{N} S_\mathrm{i}\rho_\mathrm{i} \tag{2.17}$$

where ρ_i is the density of each fluid phase. A similar argument is valid for the effective matrix bulk modulus and density, ρ_m, if it consists of several minerals. The effective density of the saturated rock, ρ^*, is straight forward with this in mind:

$$\rho^* = \rho_\mathrm{m}\,(1-\phi) + \rho_\mathrm{f}\phi \tag{2.18}$$

Finally, the effective velocities in the saturated rock are given by:

$$\mathrm{V_S^*} = \sqrt{\frac{\mu^*}{\rho*}} \tag{2.19}$$

and

$$\mathrm{V_P^*} = \sqrt{\frac{\mathrm{K}^* + \frac{4}{3}\mu^*}{\rho*}} \tag{2.20}$$

2.3 Numerical results

2.3.1 The rock physics model

A rock physical model was constructed with the aid of three different components: the matrix material, the geometric structure of the dry rock and the pore fluid. Pure quartz sandstone formed the basis of the matrix material, which is the stiffest part of the reservoir rock, with elastic properties listed in table 2.1. However, the dry rock properties are also greatly influenced by the geometric structure of the porosity. In this thesis, we have used a mixture of spherical inclusions and very low aspect ratio inclusions, representing the pores and the cracks respectively. The non-interacting compliance (2.10) approach was used to add them as empty inclusions into the matrix material. They were modelled as two separate phases and averaged over an orientation distribution function (2.12) such that they would give an isotropic response on a macroscopic scale. Inclusions with very high aspect ratios will give a stiffer rock than low aspect ratios. The dry bulk and shear moduli was found from the effective dry stiffness matrix (2.13). Two different rock physical models with a basis in these dry rock properties were chosen for varying fluid phases. A homogenous mixture of two different fluid phases, chosen to be either gas and water or oil and water, was chosen as pore fluids. The effective bulk modulus of the fluid was calculated by the equation of Wood (2.16), and the effective fluid density was calculated by (2.17). Finally, the pore fluid was introduced into the dry rock in accordance with the Gassmann-Biot theory (2.15, 2.14). An isotropic poroelastic medium can then be characterized by the effective P- and S-wave velocities (2.19, 2.20) as well as the density (2.18). Higher order effects could have been included for other choices of rock physical models such as the T-matrix approach (Jakobsen et al., 2003). However, the non-interacting compliance approach is compatible with simple models for pressure effects (Tod, 2002).

2.3.2 Calibration of the rock physics model

A good understanding of the relevant rock physics plays a central role in the characterization of reservoirs. In order to se the implications of Aki-Richards approximation on reservoir parameters, the rock physics modelling should give us realistic values of effective stiffnesses. However, higher order effects are not modelled by the presented procedure, and it does not incorporate deformation of the inclusions in vicinity of other inclusions and interactions between rocks and fluids. It is sometimes necessary to modify the rock physics parameters in order to be able to use such a simple rock physical model. Well logs are often used to calibrate a set of modified rock physical parameters such that the model match the observed well data. A similar rock physics model has previously been calibrated to wells from the Oseberg (Larsen, 2010). The frame and fluid moduli that was calibrated will also be adopted here, but there have been some slight modifications in the geometric structure of the dry rock. Specifically, the crack density was increased, which softens the rock, whilst the pore aspect ratio was

increased to spherical pores, which stiffens the rock. The adjustments were performed in such a manner that the dry rock properties would on the similar values as for the original choice of parameters. The static parameters used in the rock physics forward modelling are given in table 2.1. A few of the resulting reservoir parameters violate the assumptions that were given about the reservoir model in a strict manner. In particular, this is the case for such a high crack density as in table 2.2, but this was necessary since the reservoir rock would be too stiff otherwise. The choice of this parameter can be justified since the rock physics model perform more in accordance with elastic properties of the in situ reservoir rocks.

2.3.3 The sensitivity of the rock physics model with saturation and porosity

In order to investigate the sensitivity of the effective elastic parameters, we assumed full knowledge of the static parameters given in tables 2.1 and 2.2 such that they could be regarded as a function of saturation and porosity. A range of porosities from 0% to 40% were plotted against water saturations from 0% to 100% in order to investigate this dependence. This was done for two different pore fluids that consisted of either oil-water (figure 2.1) or gas-water (figure 2.2). The upper P-wave velocity was limited to 3500 m/s in the plots in order to demonstrate the sensitivity for a larger range of saturations and porosities because there is a very large increase for low porosities and high water saturations. Increasing porosity caused the effective elastic properties to become more sensitive to changes in saturation. It was also apparent that the P-wave velocity and the density is more sensitive to saturation changes than S-wave velocity. This may be attributed to that the shear modulus does not change with saturation (2.15). A less dense second fluid phase, as in gas instead of oil, causes a greater density change as one would expect. The P-wave velocity has smooth gradient with respect to saturation for an oil-water pore fluid. However, a gas-water pore fluid is very sensitive to high water saturations. The bulk modulus of the gas (table 2.1) yields a low bulk modulus of the fluid (2.16) for low and intermediate water saturations, and thus causes the reservoir rock to soften more rapidly.

Table 2.1: The material parameters used in the rock physics forward modelling. The frame and fluid properties are calibrated to well data from the Oseberg field (Larsen, 2010).

Material	$\kappa\,(GPa)$	$\mu\,(GPa)$	$\rho\,(Kgm^{-3})$
Quartz	37	44	2650
Frame	37	16.6	2670.6
Gas	35.9×10^{-3}	0	221.5
Oil	408.85×10^{-3}	0	671
Water	2173.9×10^{-3}	0	997.9

Table 2.2: The parameters used to describe the pore geometry in the rock physics forward modelling.

Parameter	**Value**
Crack aspect ratio α_{c}	0.001
Pore aspect ratio α_{p}	1
Crack density	0.8533

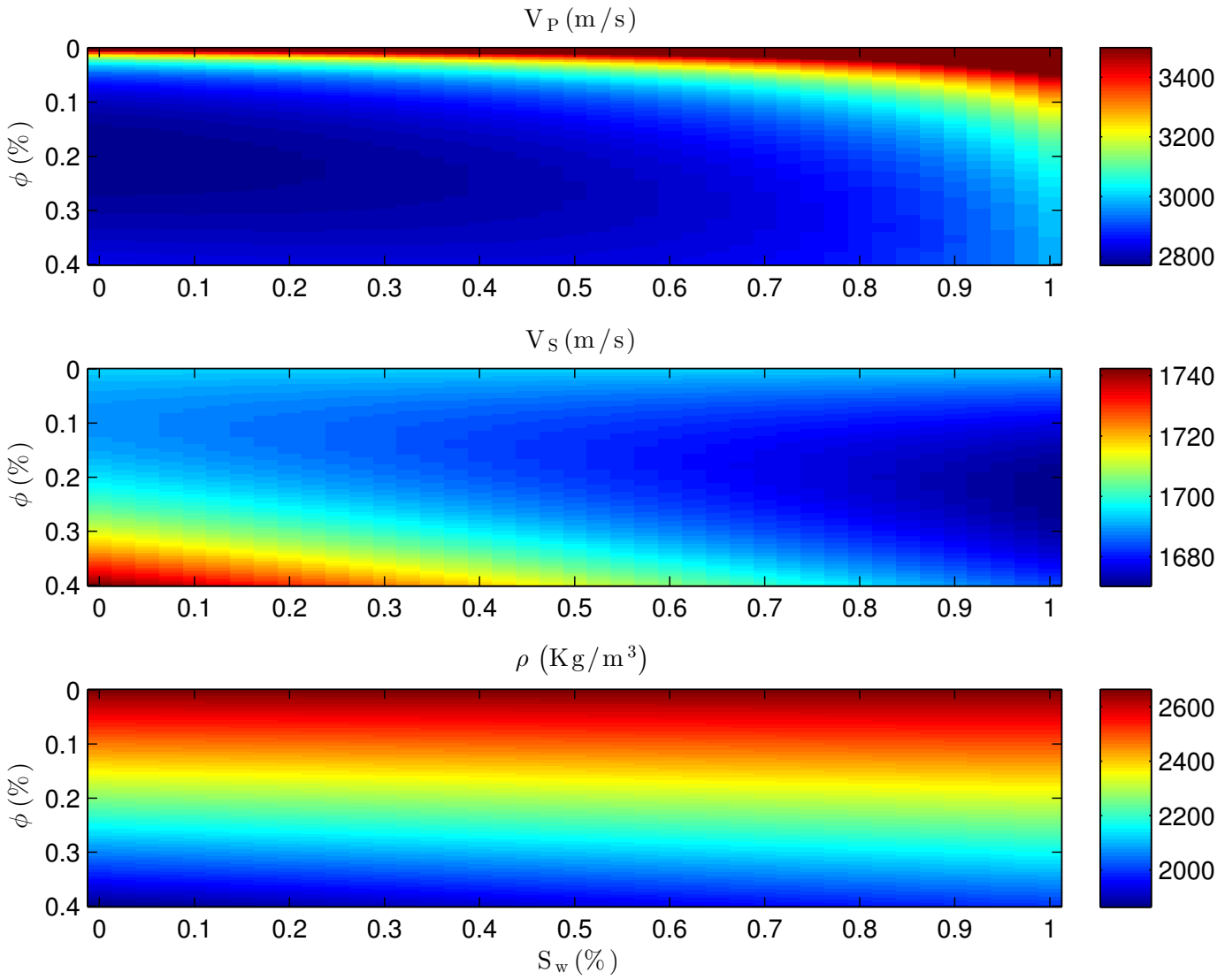

Figure 2.1: The sensitivity of the effective elastic properties to variations in porosity and saturation for an oil-water saturated reservoir rock

.

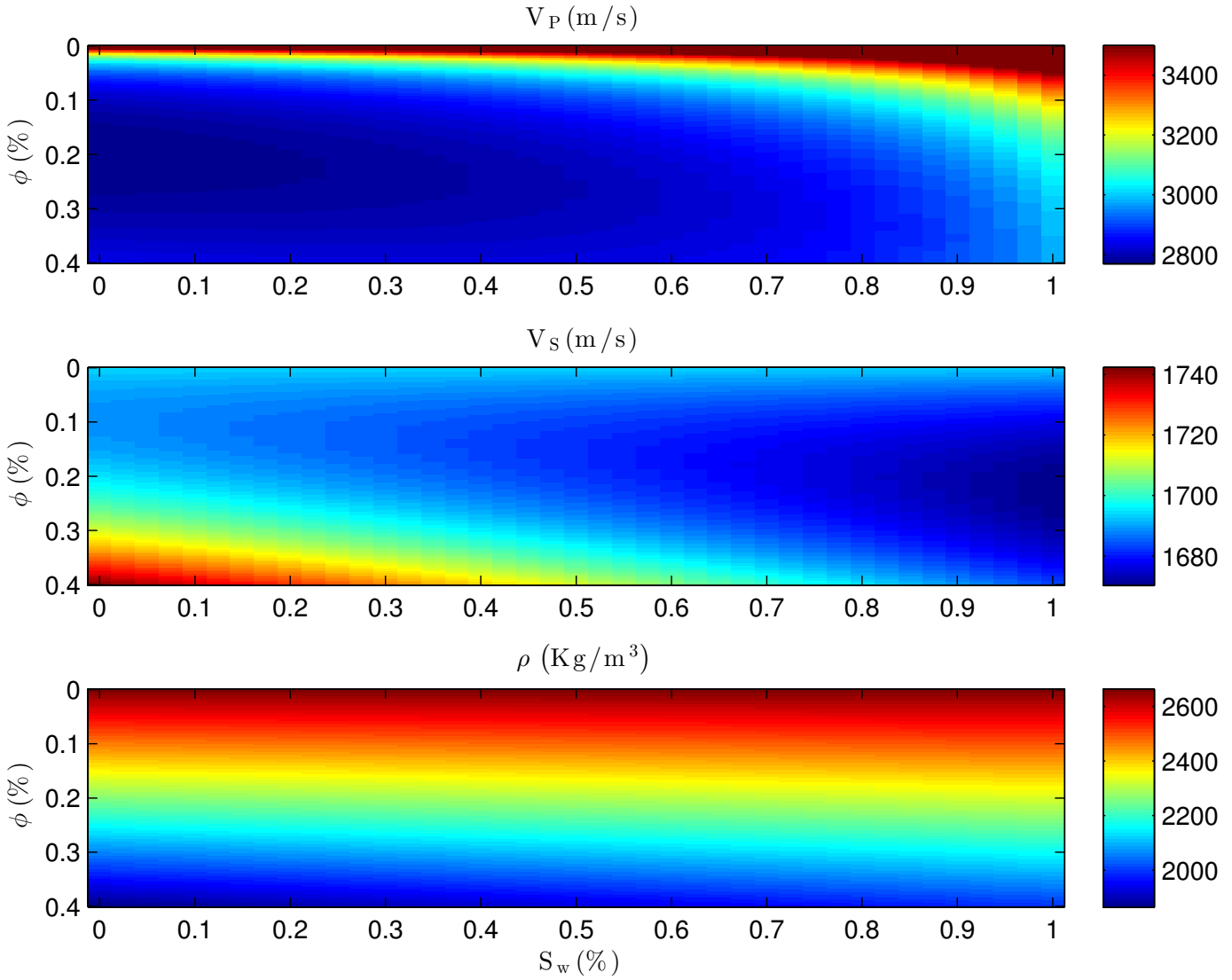

Figure 2.2: The sensitivity of the effective elastic properties to variations in porosity and saturation for a gas-water saturated reservoir rock

.

Chapter 3

Seismic amplitude versus angle

3.1 Reflection coefficients for plane waves

3.1.1 The full Zoeppritz equations

Starting with the equations of motion and Hooke's law, one can derive and solve the wave equations for plane elastic waves in isotropic media. Then, using the equations of continuity for the vertical and tangential components of stress and strain at a layer boundary, plane wave solutions and Snell's law that relates propagation angles to wave velocities, one obtains the Zoeppritz equations (Zoeppritz, 1919) for computing the exact relation between the amplitudes of the reflected and transmitted P- and S- wave. The Zoeppritz equations for an incident P-wave can be written in matrix notation as (Auld, 1990):

$$\begin{bmatrix} \sin\theta_{\mathrm{i}} & \cos\phi_{\mathrm{r}} & -\sin\theta_{\mathrm{t}} & \cos\phi_{\mathrm{t}} \\ \cos\theta_{\mathrm{i}} & -\sin\phi_{\mathrm{r}} & \cos\theta_{\mathrm{t}} & \sin\phi_{\mathrm{t}} \\ \sin 2\theta_{\mathrm{i}} & \mathrm{a}_1\cos 2\phi_{\mathrm{r}} & \mathrm{b}_1\sin 2\theta_{\mathrm{t}} & -\mathrm{c}_1\cos 2\phi_{\mathrm{t}} \\ \cos 2\phi_{\mathrm{r}} & -\mathrm{a}_2\sin 2\phi_{\mathrm{r}} & -\mathrm{b}_2\cos 2\phi_{\mathrm{t}} & -\mathrm{c}_2\sin 2\phi_{\mathrm{t}} \end{bmatrix} \begin{bmatrix} \mathrm{R_{PP}} \\ \mathrm{R_{PS}} \\ \mathrm{T_{PP}} \\ \mathrm{T_{PS}} \end{bmatrix} = \begin{bmatrix} -\sin\theta_{\mathrm{i}} \\ \cos\theta_{\mathrm{i}} \\ \sin 2\theta_{\mathrm{i}} \\ -\cos 2\phi_{\mathrm{r}} \end{bmatrix} \tag{3.1}$$

where:

$$\begin{aligned} \mathrm{a}_1 &= \frac{\mathrm{V_{P1}}}{\mathrm{V_{S1}}} & \mathrm{b}_1 &= \frac{\mathrm{V_{S2}^2 V_{P1}}\rho_2}{\mathrm{V_{S1}^2 V_{P2}}\rho_1} & \mathrm{c}_1 &= \frac{\mathrm{V_{P1}V_{S2}}\rho_2}{\mathrm{V_{S1}^2}\rho_1} \\ \mathrm{a}_2 &= \frac{\mathrm{V_{S1}}}{\mathrm{V_{P1}}} & \mathrm{b}_2 &= \frac{\mathrm{V_{P2}}\rho_2}{\mathrm{V_{P1}}\rho_1} & \mathrm{c}_2 &= \frac{\mathrm{V_{S2}}\rho_2}{\mathrm{V_{P1}}\rho_1} \end{aligned} \tag{3.2}$$

Here $\mathrm{V_{P1}}$, $\mathrm{V_{P2}}$, $\mathrm{V_{S1}}$, $\mathrm{V_{S2}}$, ρ_1, ρ_2 are the P- and S-wave velocities and the densities above and below the boundary, θ_{i} is incident P-wave angle, θ_{t} is transmitted P-wave angle, ϕ_{r} is reflected S-wave angle and ϕ_{t} is transmitted S-wave angle. The different reflection and transmission angles are related to the

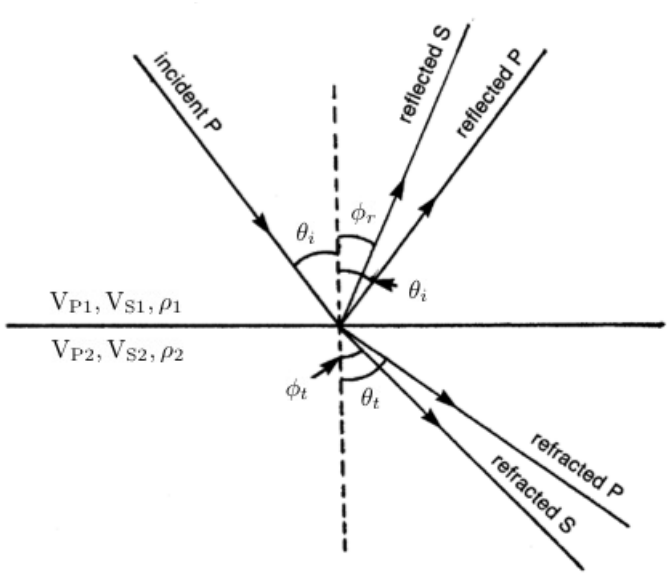

Figure 3.1: Reflection and refraction of an incident P-wave at a layer boundary. Modified from Yilmaz (2001).

incident angle by a ray parameter, p, through Snell's law:

$$\mathrm{p} = \frac{\sin\theta_\mathrm{i}}{\mathrm{V_{P1}}} = \frac{\sin\theta_\mathrm{t}}{\mathrm{V_{P2}}} = \frac{\sin\phi_\mathrm{r}}{\mathrm{V_{S1}}} = \frac{\sin\phi_\mathrm{t}}{\mathrm{V_{S2}}} \tag{3.3}$$

and (3.1) may thus be solved for the reflection and transmission coefficients for an incident P-wave:

$$\begin{bmatrix} \mathrm{R_{PP}} \\ \mathrm{R_{PS}} \\ \mathrm{T_{PP}} \\ \mathrm{T_{PS}} \end{bmatrix} = \begin{bmatrix} \sin\theta_\mathrm{i} & \cos\phi_\mathrm{r} & -\sin\theta_\mathrm{t} & \cos\phi_\mathrm{t} \\ \cos\theta_\mathrm{i} & -\sin\phi_\mathrm{r} & \cos\theta_\mathrm{t} & \sin\phi_\mathrm{t} \\ \sin 2\theta_\mathrm{i} & \mathrm{a}_1\cos 2\phi_\mathrm{r} & \mathrm{b}_1\sin 2\theta_\mathrm{t} & -\mathrm{c}_1\cos 2\phi_\mathrm{t} \\ \cos 2\phi_\mathrm{r} & -\mathrm{a}_2\sin 2\phi_\mathrm{r} & -\mathrm{b}_2\cos 2\phi_\mathrm{t} & -\mathrm{c}_2\sin 2\phi_\mathrm{t} \end{bmatrix}^{-1} \begin{bmatrix} -\sin\theta_\mathrm{i} \\ \cos\theta_\mathrm{i} \\ \sin 2\theta_\mathrm{i} \\ -\cos 2\phi_\mathrm{r} \end{bmatrix} \tag{3.4}$$

3.1.2 Aki-Richards approximation

Over the years, a number of linearized approximations to the Zoeppritz equations have been made (Aki and Richards, 1980; Bortfeld, 1961; Shuey, 1985). Aki and Richards approximation to the reflection coefficients from the exact Zoeppritz equations is among the more popular. The prerequisite is that the contrasts in elastic properties are much less than one over the boundary and that the reflection and transmitted angles do not approach 90° (Aki and Richards, 1980). We may then expect that the converted wave reflection coefficients will be small such that second order terms can be neglected. The PP-reflectivity can be formulated as a linear combination in terms of fractional changes in P-wave velocity ($\mathrm{V_P}$), S-wave velocity ($\mathrm{V_S}$) and density (ρ) across the layer boundary:

$$\mathrm{r_{PP}}\left(\theta\right) = \frac{1}{2}\left(1+\tan^2\theta\right)\frac{\Delta\mathrm{V_P}}{\bar{\mathrm{V}}_\mathrm{P}} - 4\left(\frac{\bar{\mathrm{V}}_\mathrm{S}^2}{\bar{\mathrm{V}}_\mathrm{P}^2}\sin^2\theta\right)\frac{\Delta\mathrm{V_S}}{\bar{\mathrm{V}}_\mathrm{S}} + \frac{1}{2}\left(1-4\frac{\bar{\mathrm{V}}_\mathrm{S}^2}{\bar{\mathrm{V}}_\mathrm{P}^2}\sin^2\theta\right)\frac{\Delta\rho}{\bar{\rho}} \tag{3.5}$$

where $\bar{V}_P = \frac{1}{2}(V_{P1} + V_{P2})$, $\bar{V}_S = \frac{1}{2}(V_{S1} + V_{S2})$, $\bar{\rho} = \frac{1}{2}(\rho_1 + \rho_2)$, $\Delta V_P = V_{P2} - V_{P1}$, $\Delta V_S = V_{S2} - V_{S1}$, $\Delta\rho = \rho_2 - \rho_1$ and $\theta = \frac{1}{2}(\theta_i + \theta_t)$. The average of incident and transmitted P-wave angle, θ, may be approximated as θ_i, the incident P-wave angle, if the reflected and transmitted angles are restricted to the precritical range (Downton and Ursenbach, 2006).

3.2 A comparison of the Zoeppritz equations and Aki-Richards approximation

3.2.1 Amplitude versus angle modelling

The Zoeppritz equations for an incident P-wave (3.4) yield an exact relationship between the contrast in elastic parameters over a boundary and the resulting transmission and reflection coefficients for P- and S-waves for plane waves. However, they do not give us any intuitive understanding of how these reflection coefficients relate to the various elastic parameters. Further more, since they are nonlinear, they do not allow for the less computationally expensive modelling and inversion algorithms (Yilmaz, 2001). As mentioned, a prerequisite for Aki-Richards approximation is that the contrast in elastic properties much less than one over the boundary and that the reflection and transmitted angles do not approach 90°. However, it is not clear how small the contrasts in elastic properties should be.

The variation of PP-reflection coefficients as a function of incidence angle was modelled for a set of pre-critical angles, which also can be referred to as amplitude versus angle (AVA) modelling (Yilmaz, 2001). An isotropic overburden and isotropic reservoir rocks were defined for this purpose. The reservoir models from section 2.3 gave varying effective elastic reservoir properties for different choices of saturation and porosity. Thus, this would also result in varying contrasts in elastic properties across the layer boundary for a fixed overburden. In this section, we investigated how the Zoeppritz equations (3.4) and Aki-Richards approximation (3.5) agree for different contrasts in elastic properties that are controlled by saturation and porosity variations. As Aki-Richards approximation is linearized in terms of contrast in elastic properties, it was expected to agree better for small contrasts. A further aim will be to identify the range of saturations and porosities the Aki-Richards approximation works satisfactory for a given reservoir model and overburden.

3.2.2 Main results and discussion

An overburden was chosen in such a manner that it would give a maximum relative contrast of $|0.25|$ for any of the elastic properties for the range of variation of reservoir parameters. Following this, the PP-reflection coefficients for varying saturations and porosities were plotted for a small angle (0°), an intermediate angle (20°) and a large angle (40°) in order to investigate how the AVA data vary with the reservoir parameters. This is shown for an oil-water pore fluid in figures 3.2 through 3.4 and for

a gas-water pore fluid in figures 3.5 through 3.7. The upper plots show the data obtained by Aki-Richards approximation and the center plots shows the data obtained by the Zoeppritz equations. The lower plots are the corresponding errors, Δ in the approximation, r_{PP}, relative to the exact reflection coefficients, R. The error in percent, Δ, for a given incident angle was defined by:

$$\Delta = \frac{(R - r_{PP})}{r_{PP}} \times 100 \tag{3.6}$$

Reflection coefficients close to zero produced very high values of relative error, and for this reason the upper and lower limit is set to 20% relative error in these plots. On the basis of these figures, a high (30%) and low (10%) porosity case were chosen for three different saturations (10%, 50% and 95%) for each of the pore fluids. The dry rock properties are given in table 3.1, and the different cases that were chosen for oil-water pore fluid and gas-water pore fluid are summarized in table 3.2. In what follows, the following terminology shall be adopted for the relative contrasts in elastic properties: very low ($< |0.05|$), low ($< |0.1|$), intermediate ($< |0.2|$) and high($|0.2| <$). Figures 3.8 to 3.13 show the reflection coefficients and the relative error for each of the cases. In each figure, an oil and water saturated reservoir is shown on the left and a gas and water saturated reservoir is shown on the right for the same set of saturation and porosity.

CASE 1a. The saturation and the porosity in the AVA modelling were ($S_w = 10\%,\ \phi = 10\%$) for an oil and water saturated reservoir. Figure 3.8 shows the reflection coefficients in the upper left plot which correspond to an intermediate relative contrast in P- and S-wave velocities and a very low contrast in relative density (table 3.2). The corresponding bottom left plot shows the error analysis: The Aki-Richards approximation and the Zoeppritz equations are in agreement for incident angles from 0° to 30°, but the error increases steadily up to -10% after that point. *CASE 1b.* The saturation and the porosity in the AVA modelling were ($S_w = 10\%,\ \phi = 10\%$) for a gas and water saturated reservoir. Figure 3.8 shows the reflection coefficients in the upper right plot which correspond to intermediate relative contrasts in velocities and a very low relative contrast in density (table 3.2). In the lower right plot, there is a close match from 0° to 20°, but the error increases steadily to a maximum of -8% at an incidence angle of 40° beyond this.

CASE 2a. The saturation and the porosity in the AVA modelling were ($S_w = 10\%,\ \phi = 30\%$) for an oil and water saturated reservoir. Figure 3.9 shows the reflection coefficients in the upper left plot which correspond intermediate relative contrasts in all the elastic properties (table 3.2). The bottom left plot shows that the reflection coefficients match up to 15°, but then steadily increase to -6%. *CASE 2b.* The saturation and the porosity in the AVA modelling were ($S_w = 10\%,\ \phi = 30\%$) for a gas and water saturated reservoir. Figure 3.9 shows the reflection coefficients in the upper right plot which correspond to a intermediate relative contrast in P-wave velocity and high contrast in density, but low contrast in S-wave velocity. However, the reflection coefficients have a close match for the full range of incident angles, the maximum error is only -3% as shown in the bottom right plot.

CASE 3a. The saturation and the porosity in the AVA modelling were ($S_w = 50\%,\ \phi = 10\%$) for an oil

and water saturated reservoir. Figure 3.10 shows the reflection coefficients in the upper left plot which correspond to intermediate relative contrasts in S-wave velocity, low in P-wave velocity and very low in density. The error is low from 0° to 30°, but then increases rapidly with several orders of magnitude, and this is due to that the reflection coefficients approaches zero. *CASE 3b.* The saturation and the porosity in the AVA modelling were ($S_w = 50\%$, $\phi = 10\%$) for a gas and water saturated reservoir. Figure 3.10 shows the reflection coefficients in the upper right plot which correspond to intermediate relative contrasts in velocities and very low in relative contrast in density. There is a good match between the reflection coefficients between 0° and 20°, but the error increases steadily to a maximum of -8% at an incidence angle of 40° beyond this.

CASE 4a. The saturation and the porosity in the AVA modelling were ($S_w = 50\%$, $\phi = 30\%$) for an oil and water saturated reservoir. Figure 3.11 shows the reflection coefficients in the upper left plot which correspond to intermediate relative contrasts in elastic properties. The error increases steadily from 10° incident angle up to a maximum of -7%. *CASE 4b.* The saturation and the porosity in the AVA modelling were ($S_w = 50\%$, $\phi = 30\%$) for a gas and water saturated reservoir. Figure 3.11 shows the reflection coefficients in the upper right plot which correspond to an intermediate relative contrast in P-wave velocity and density, but low for S-wave velocity. As shown in the bottom right plot, the reflection coefficients have a very good match, the maximum error is only 5%.

CASE 5a. The saturation and the porosity in the AVA modelling were ($S_w = 95\%$, $\phi = 10\%$) for an oil and water saturated reservoir. Figure 3.12 shows the reflection coefficients in the upper left plot which correspond to a intermediate relative contrast in S-wave velocity, but very low (positive) relative contrast in P-wave velocity and very low density. The error increases to a maximum of approximately 6% at 24°, but then declines to about 4% at 40°. *CASE 5b.* The saturation and the porosity in the AVA modelling were ($S_w = 95\%$, $\phi = 10\%$) for a gas and water saturated reservoir. Figure 3.12 shows the reflection coefficients in the upper right plot which correspond to intermediate relative contrasts in velocities and very low relative contrast in density. The error is low from 0° to 30°, but then increases rapidly with several orders of magnitude, and this is due to that the reflection coefficients approaches zero.

CASE 6a. The saturation and the porosity in the AVA modelling were ($S_w = 95\%$, $\phi = 30\%$) for an oil and water saturated reservoir. Figure 3.13 shows the reflection coefficients in the upper left plot which correspond to a intermediate relative contrast in S-wave velocity and density, but low in P-wave velocity. The reflection coefficients have a close match for low to intermediate angles, but the error increases from -5% to -35% in the interval from 28° to 40°. *CASE 6b.* The saturation and the porosity in the AVA modelling were ($S_w = 95\%$, $\phi = 30\%$) for a gas and water saturated reservoir. Figure 3.13 shows the reflection coefficients in the upper right plot which correspond to intermediate relative contrasts in all elastic properties. The reflection coefficients have a close match from 0° to 30°, but it increases steadily to a maximum of about -6% at an incidence angle of 40° beyond this.

It was apparent from the above analysis of the accuracy of Aki-Richards approximation for PP-

reflectivity that the error generally increases with incident angle. Conversions between P- and S-waves were not modeled by the linearized approximation, but such second order effects are more prominent for higher incident angles (Auld, 1990). Also, it can be noted that the equations for converted reflection coefficients in Aki-Richards approximation are insensitive to first-order changes in the P-wave velocity (Aki and Richards, 1980). However, it is possible to rearrange the terms in eq.(3.5) so that they become increasingly important with increasing angle of incidence. Thus, lowering the range of incident angles that is used for the forward modelling would also lower the information content in the data significantly (Smith and Gidlow, 1987). High relative contrasts in density did not seem to increase the error as prominent as for high contrasts in velocities. It is also evident that it is not sufficient to observe the parameters individually, but the deviation from the exact reflection coefficients depend on all three elastic parameters simultaneously. The magnitude of the relative errors, that were not related to zero reflectivity, ranges from -3% to -35%. They may occur insignificant at first sight, but it was not yet clear how this would affect the saturation and porosity estimates in the inverse problem.

Table 3.1: Elastic properties of the overburden and the dry reservoir rocks

	$V_P\,(ms^{-1})$	$V_S\,(ms^{-1})$	$\rho\,(Kgm^{-3})$
Overburden	3150	1900	2500
Dry reservoir rock ($\phi = 10\%$)	2721	1736	2395
Dry reservoir rock ($\phi = 20\%$)	2795	1770	2127
Dry reservoir rock ($\phi = 25\%$)	2843	1794	1994
Dry reservoir rock ($\phi = 30\%$)	2890	1824	1860

Table 3.2: Elastic properties and contrasts for various porosities and water saturations.

Oil-water saturated reservoir rock								
Case	S_w (%)	ϕ (%)	V_P (ms^{-1})	V_S (ms^{-1})	ρ (Kgm^{-3})	$\frac{\Delta V_P}{\bar{V}_P}$	$\frac{\Delta V_S}{\bar{V}_S}$	$\frac{\Delta \rho}{\bar{\rho}}$
1a	0.1	0.1	2822	1688	2467	-0.1098	-0.1182	-0.0133
2a	0.1	0.3	2790	1708	2073	-0.1212	-0.1064	-0.1867
3a	0.5	0.1	2900	1683	2480	-0.0826	-0.1211	-0.0080
4a	0.5	0.3	2806	1692	2113	-0.1155	-0.1158	-0.1678
5a	0.95	0.1	3185	1678	2496	0.0110	-0.1241	-0.0016
6a	0.95	0.3	2948	1675	2158	-0.0663	-0.1259	-0.1468
Gas-water saturated reservoir rock								
Case	S_w (%)	ϕ (%)	V_P (ms^{-1})	V_S (ms^{-1})	ρ (Kgm^{-3})	$\frac{\Delta V_P}{\bar{V}_P}$	$\frac{\Delta V_S}{\bar{V}_S}$	$\frac{\Delta \rho}{\bar{\rho}}$
1b	0.1	0.1	2679	1702	2425	-0.1616	-0.1099	-0.0305
2b	0.1	0.3	2799	1761	1951	-0.1180	-0.0759	-0.24677
3b	0.5	0.1	2675	1691	2457	-0.1631	-0.1164	-0.0173
4b	0.5	0.3	2740	1720	2045	-0.1392	-0.0994	-0.2002
5b	0.95	0.1	2843	1679	2493	-0.1025	-0.1235	-0.0028
6b	0.95	0.3	2756	1677	2151	-0.1334	-0.1247	-0.1501

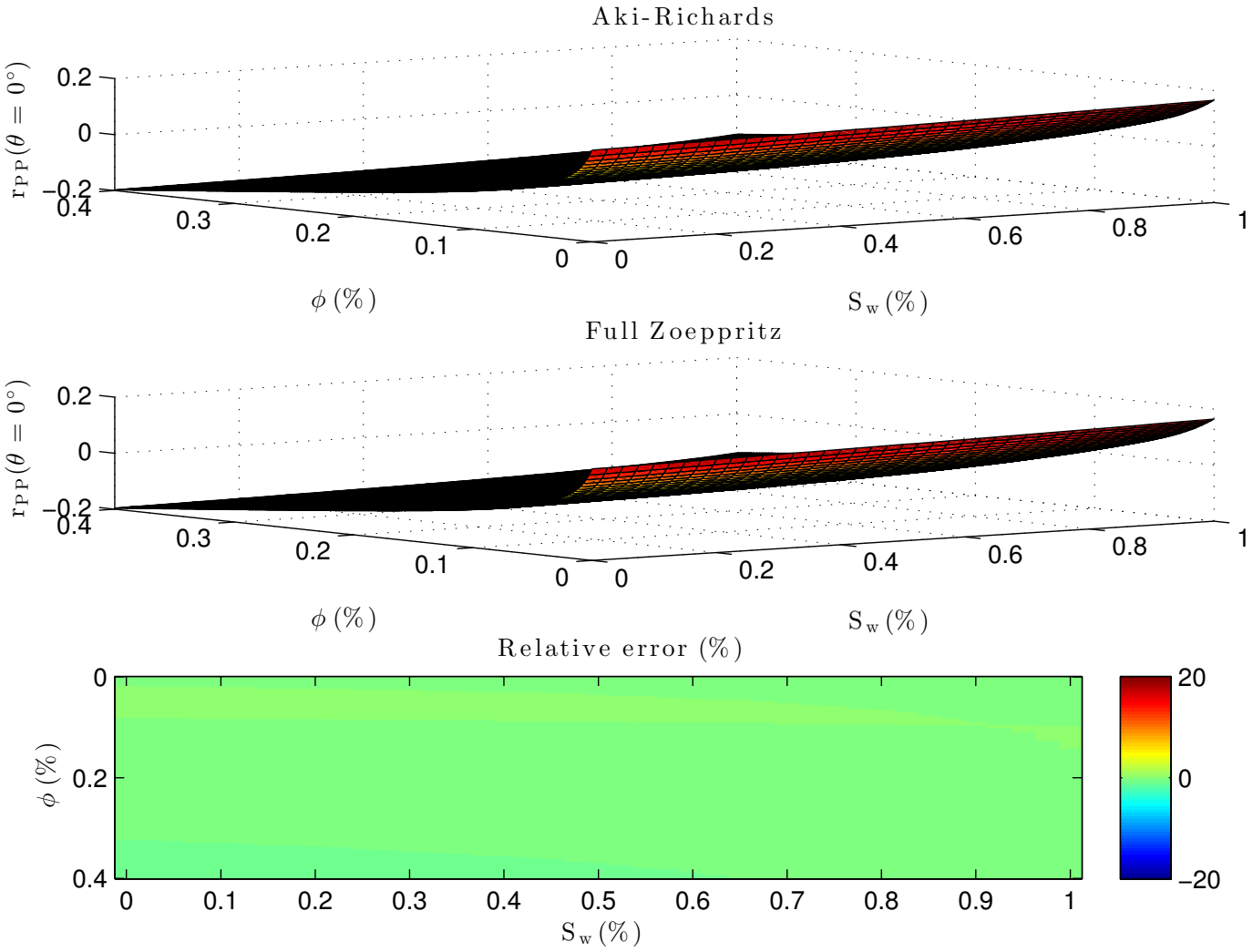

Figure 3.2: The sensitivity of r_{PP} for an oil-water saturated reservoir rock for a fixed incident angle (0°): Aki-Richards (top), Zoeppritz equations (center) and the relative error limited to 20% (bottom). The errors were limited since reflection coefficients close to zero cause very high values of relative error.

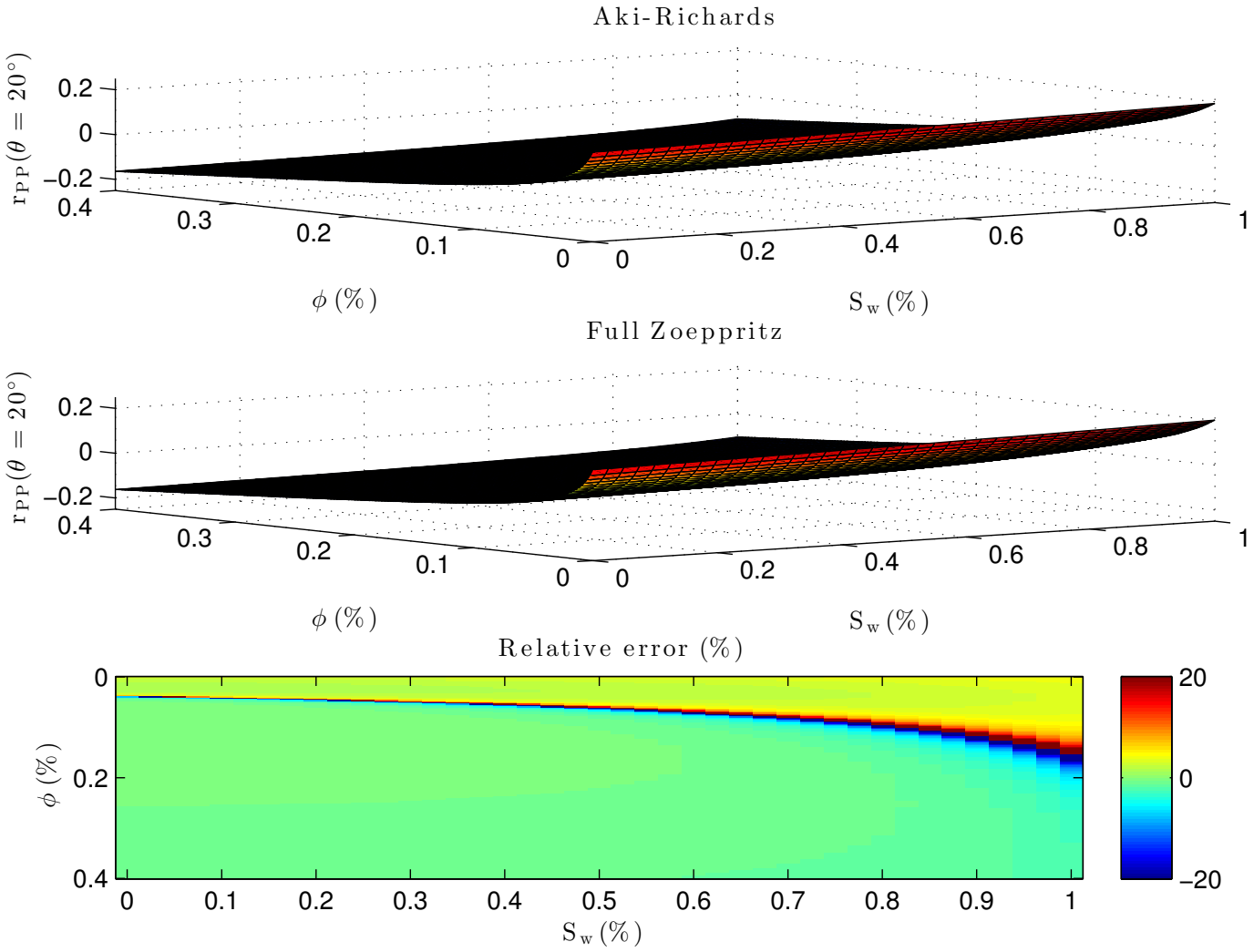

Figure 3.3: The sensitivity of r_{PP} for an oil-water saturated reservoir rock for a fixed incident angle (20°): Aki-Richards (top), Zoeppritz equations (center) and the relative error limited to 20% (bottom). The errors were limited since reflection coefficients close to zero cause very high values of relative error.

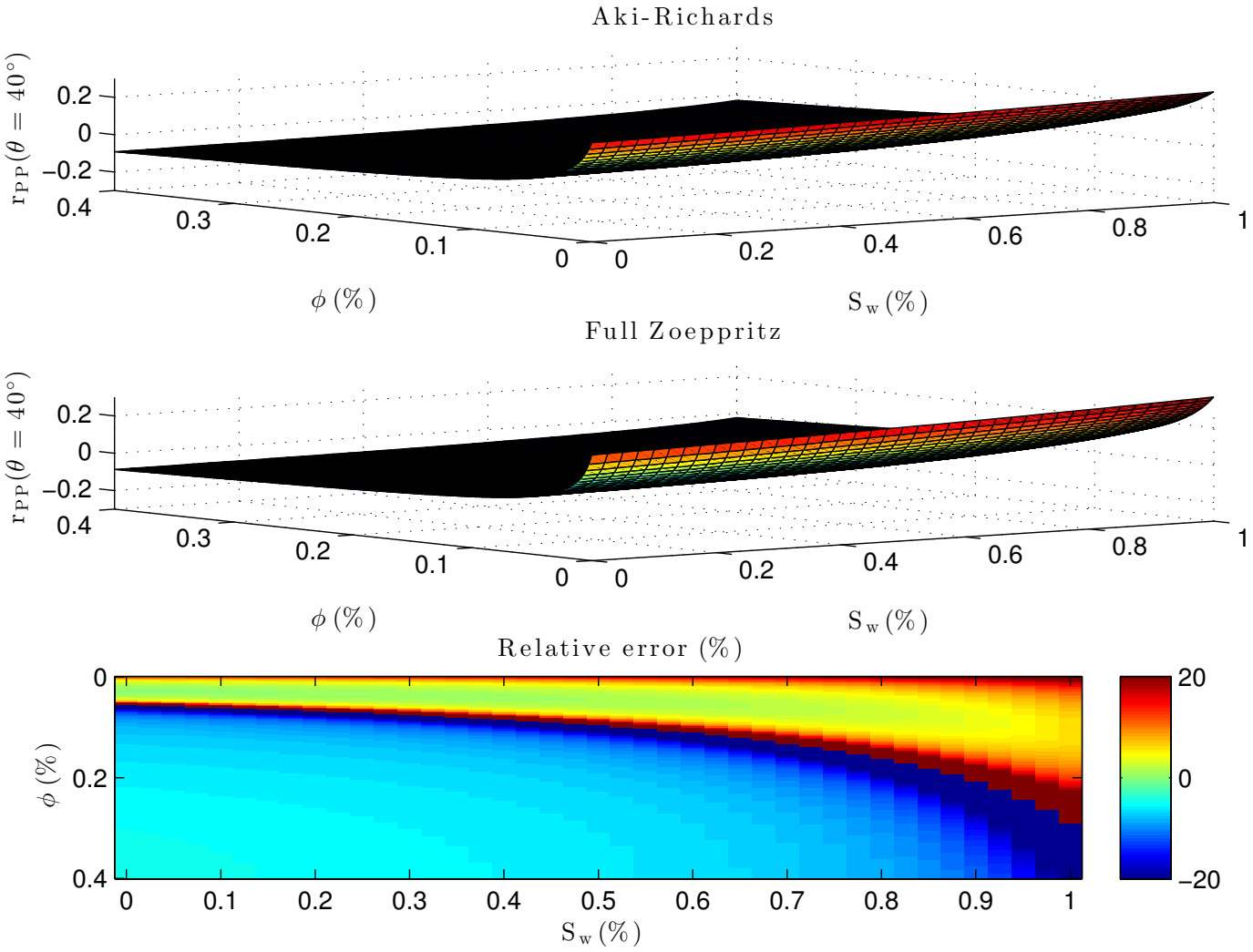

Figure 3.4: The sensitivity of r_{PP} for an oil-water saturated reservoir rock for a fixed incident angle (40°): Aki-Richards (top), Zoeppritz equations (center) and the relative error limited to 20% (bottom). The errors were limited since reflection coefficients close to zero cause very high values of relative error.

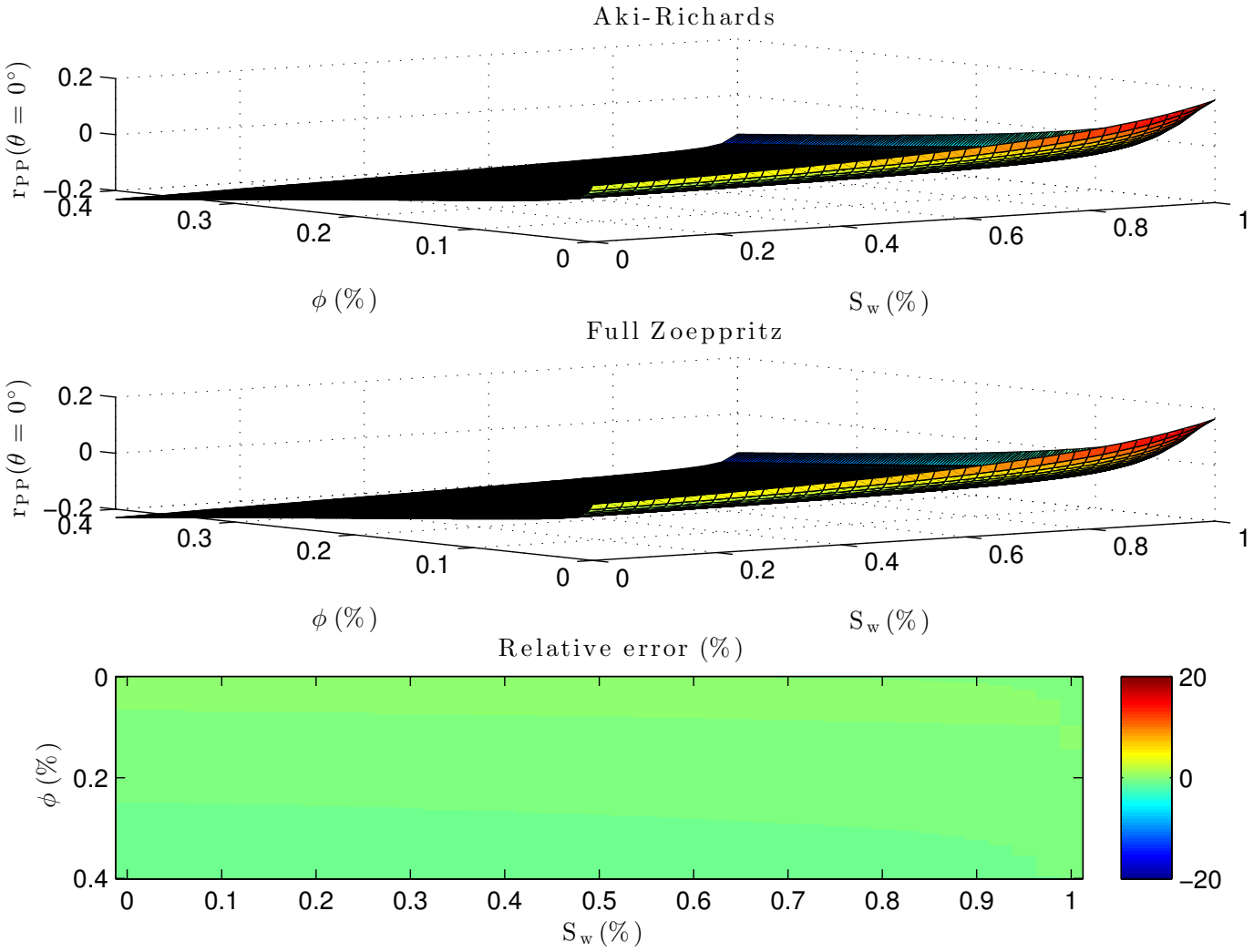

Figure 3.5: The sensitivity of r_{PP} for a gas-water saturated reservoir rock for a fixed incident angle (0°): Aki-Richards (top), Zoeppritz equations (center) and the relative error limited to 20% (bottom). The errors were limited since reflection coefficients close to zero cause very high values of relative error.

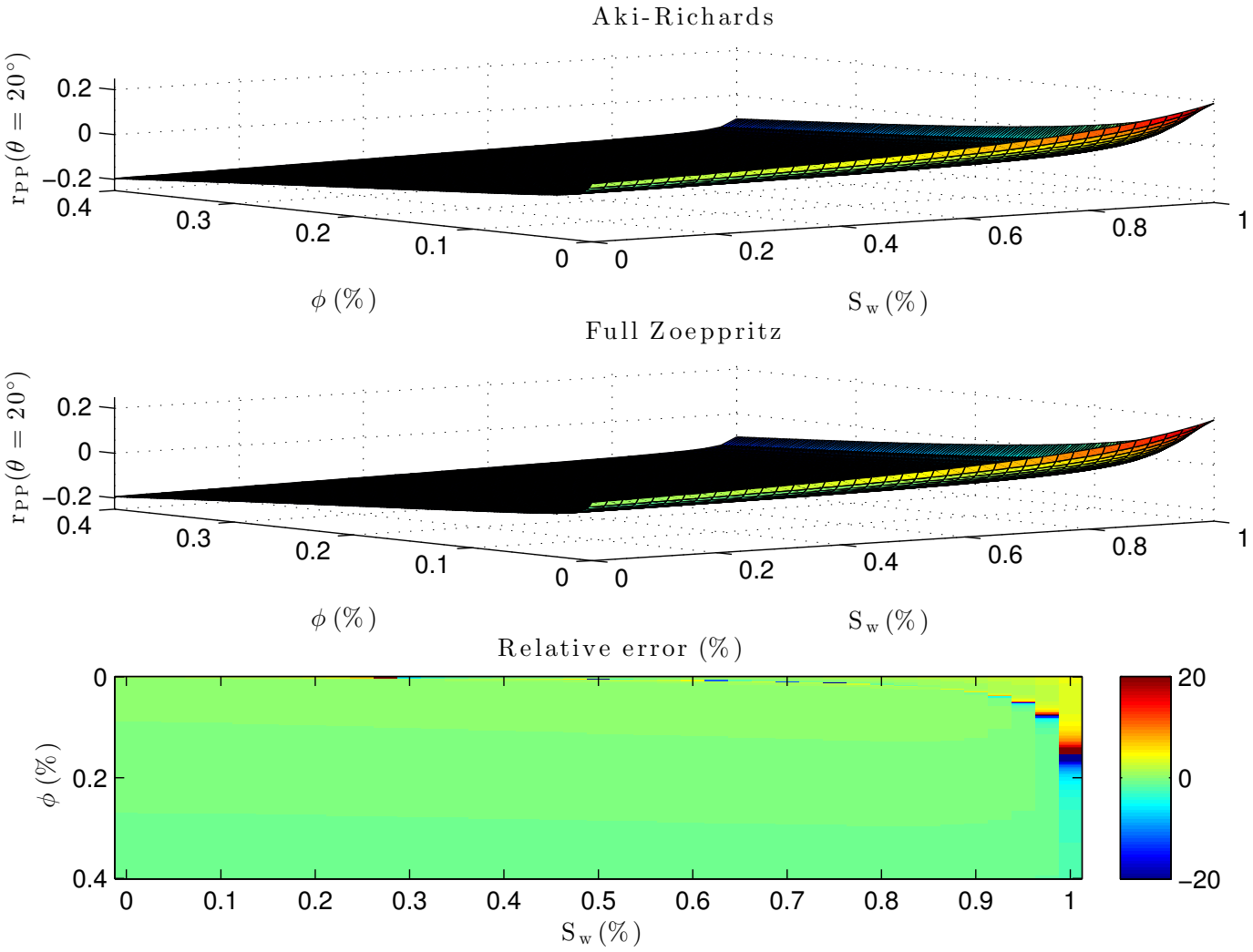

Figure 3.6: The sensitivity of r_{PP} for a gas-water saturated reservoir rock for a fixed incident angle (20°): Aki-Richards (top), Zoeppritz equations (center) and the relative error limited to 20% (bottom). The errors were limited since reflection coefficients close to zero cause very high values of relative error.

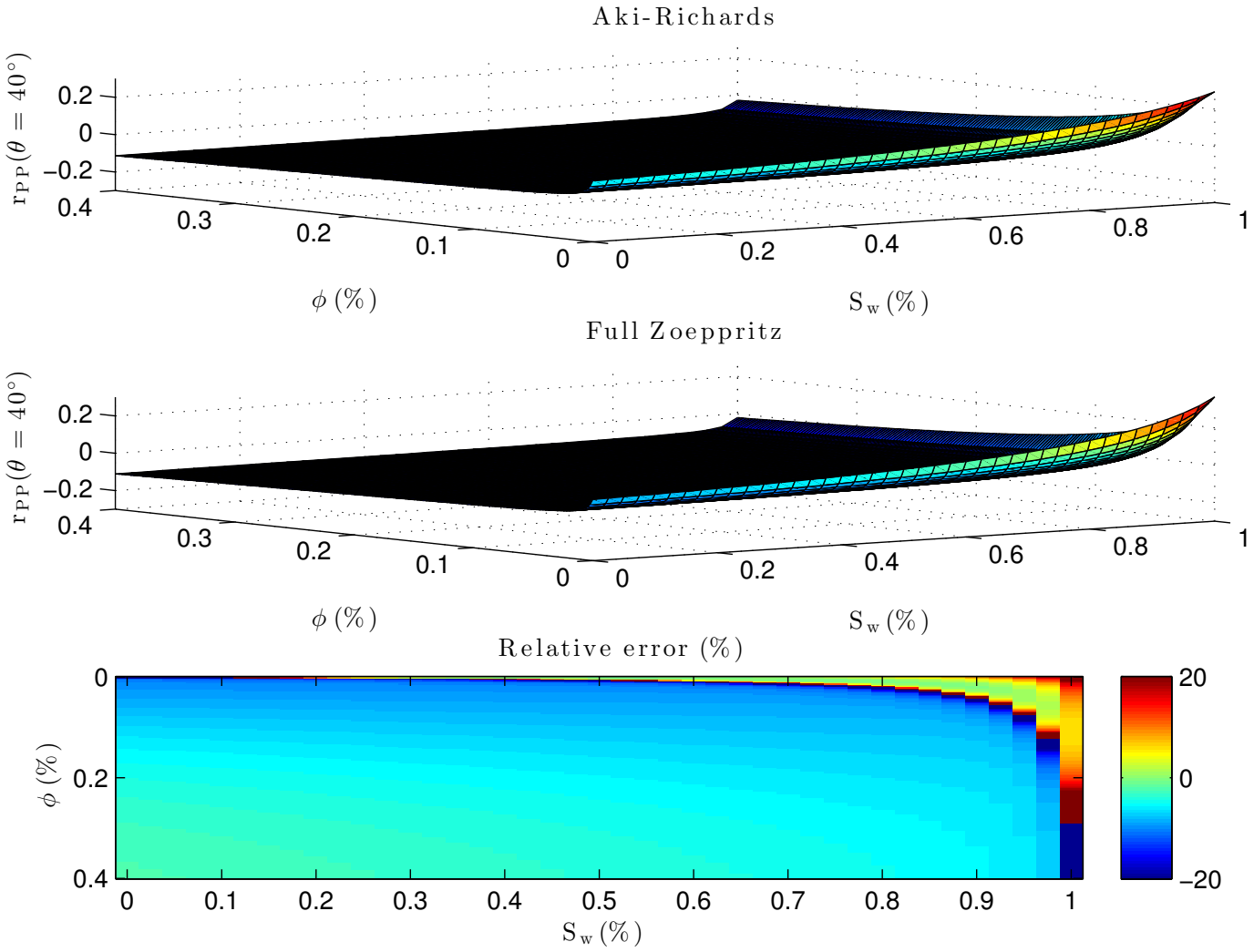

Figure 3.7: The sensitivity of r_{PP} for a gas-water saturated reservoir rock for a fixed incident angle (40°): Aki-Richards (top), Zoeppritz equations (center) and the relative error limited to 20% (bottom). The errors were limited since reflection coefficients close to zero cause very high values of relative error.

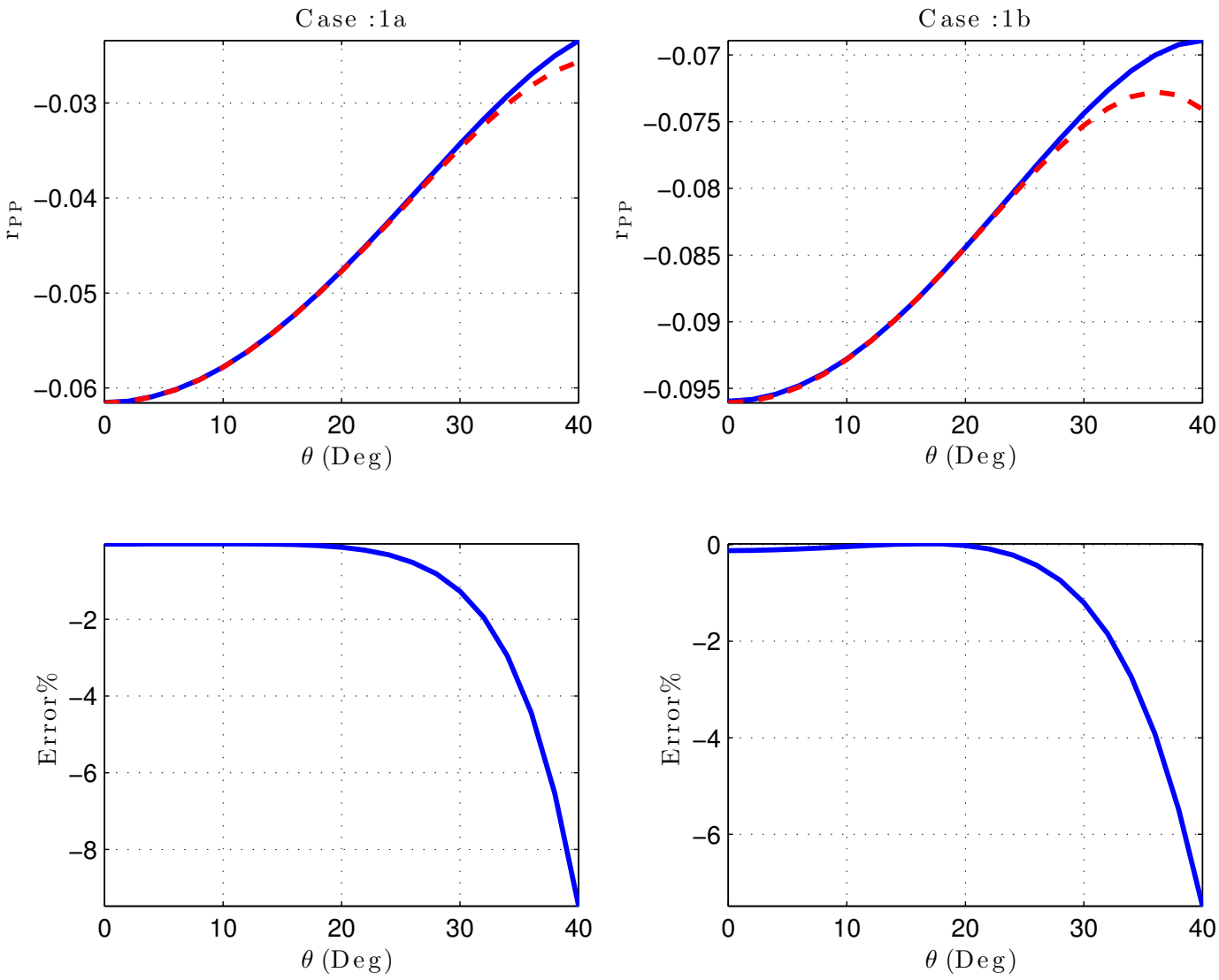

Figure 3.8: Comparison of reflection coefficients as a function of incidence angle using Aki-Richards (dashed red) approximation and exact Zoeppritz (solid blue). The saturation is $S_w = 10\%$ and the porosity is $\phi = 10\%$. An oil and water saturated reservoir on the left and a gas and water saturated reservoir on the right.

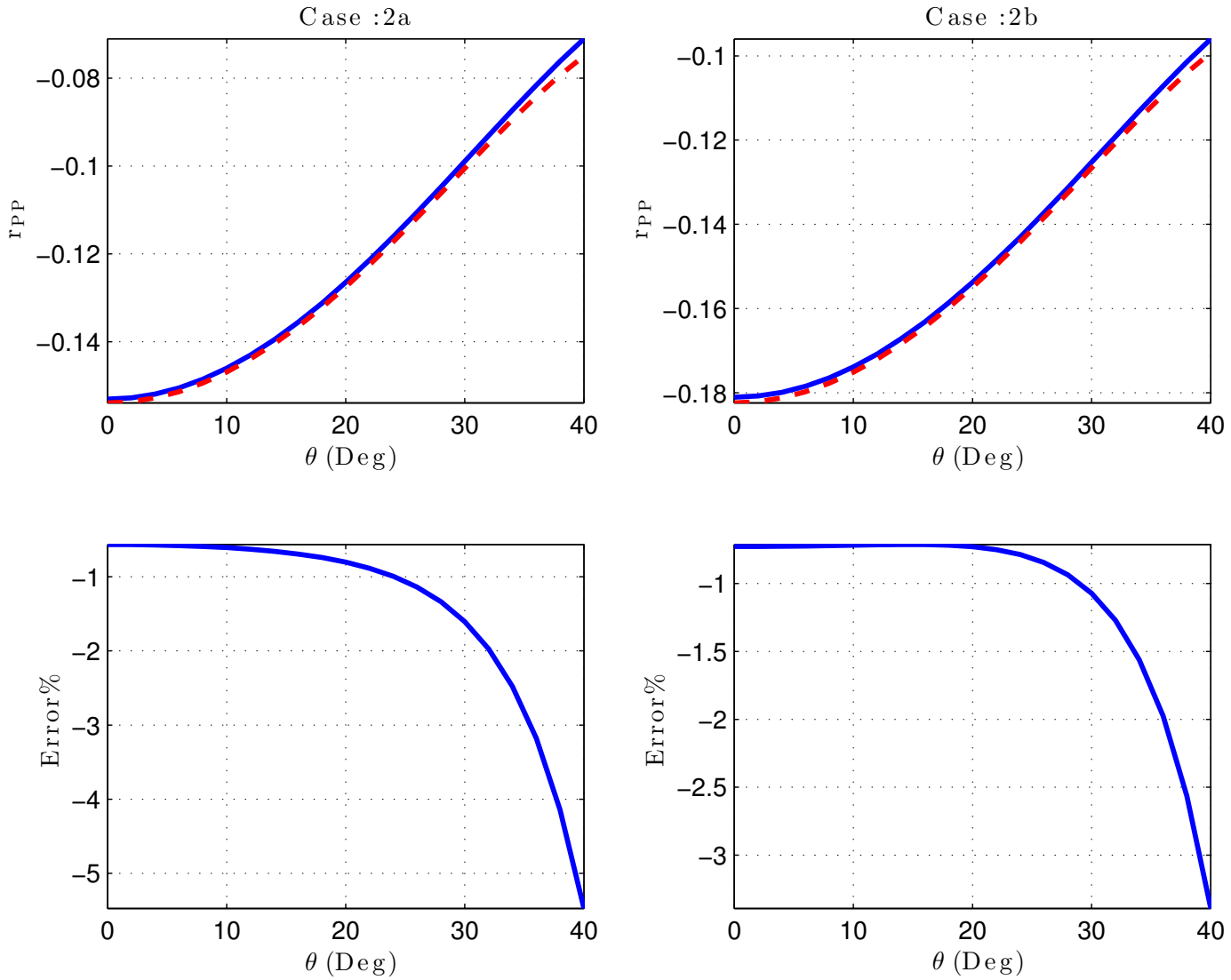

Figure 3.9: Comparison of reflection coefficients as a function of incidence angle using Aki-Richards (dashed red) approximation and exact Zoeppritz (solid blue). The saturation is $S_w = 10\%$ and the porosity is $\phi = 30\%$. An oil and water saturated reservoir on the left and a gas and water saturated reservoir on the right.

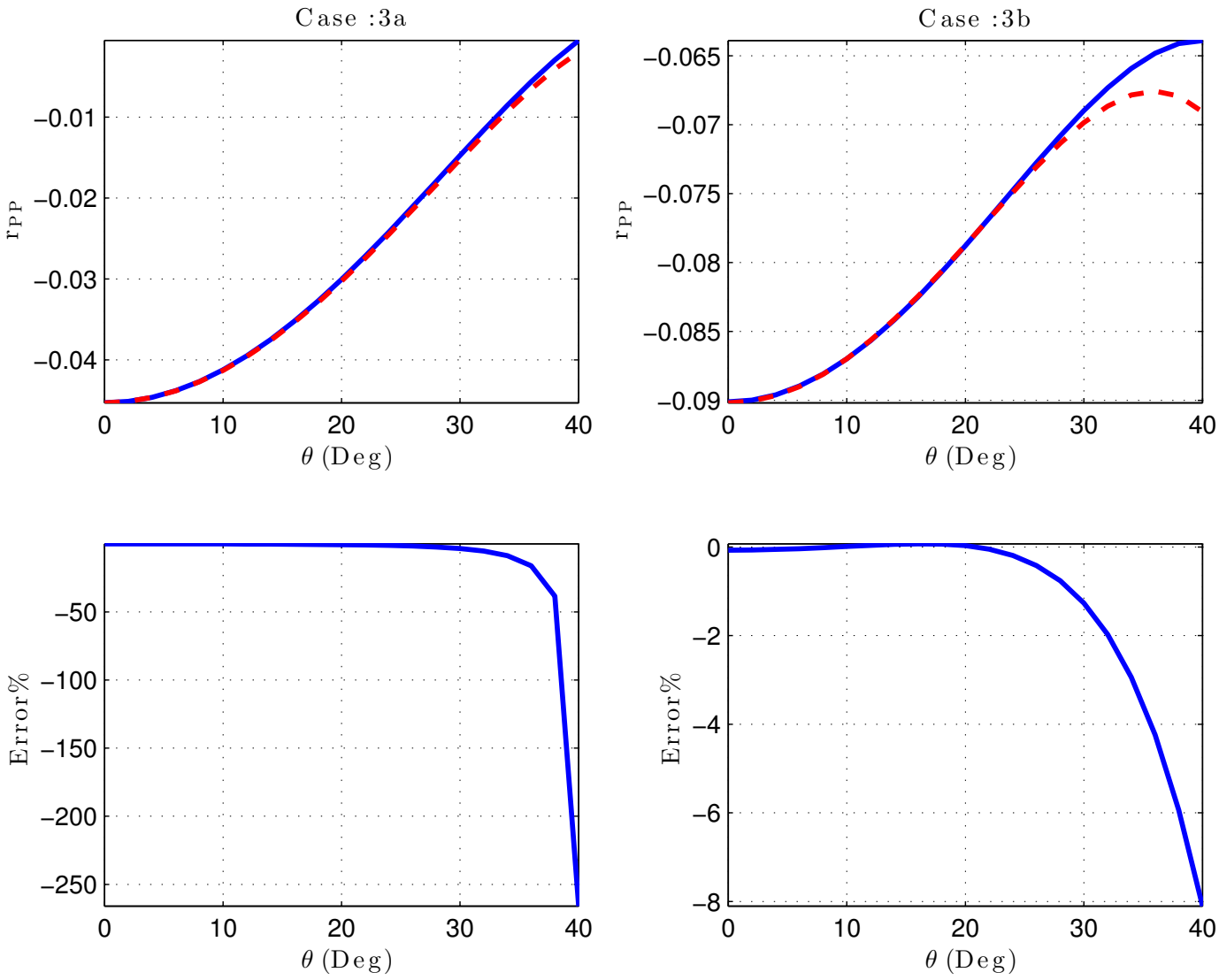

Figure 3.10: Comparison of reflection coefficients as a function of incidence angle using Aki-Richards (dashed red) approximation and exact Zoeppritz (solid blue). The saturation is $S_w = 50\%$ and the porosity is $\phi = 10\%$. An oil and water saturated reservoir on the left and a gas and water saturated reservoir on the right.

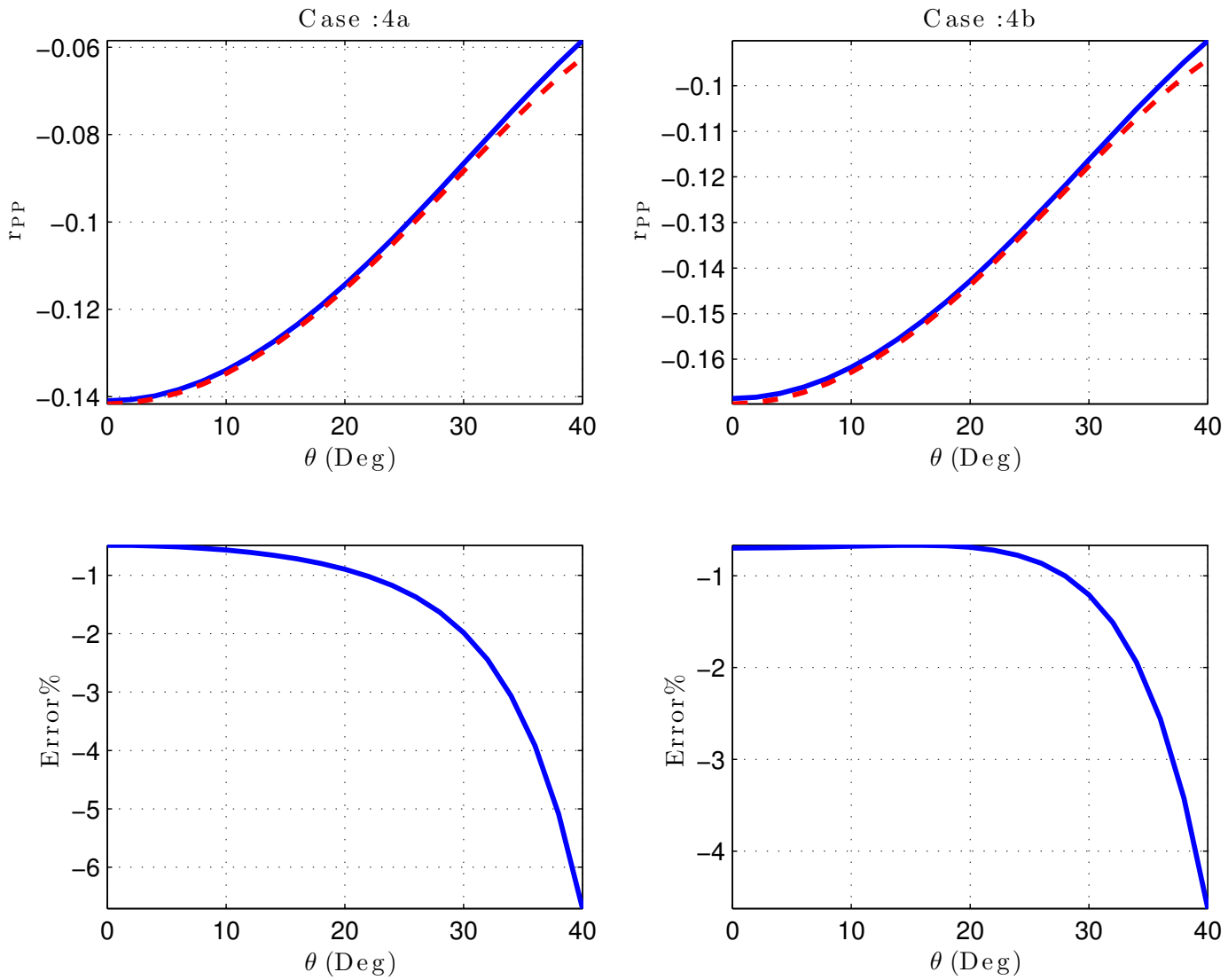

Figure 3.11: Comparison of reflection coefficients as a function of incidence angle using Aki-Richards (dashed red) approximation and exact Zoeppritz (solid blue). The saturation is $S_w = 50\%$ and the porosity is $\phi = 30\%$. An oil and water saturated reservoir on the left and a gas and water saturated reservoir on the right.

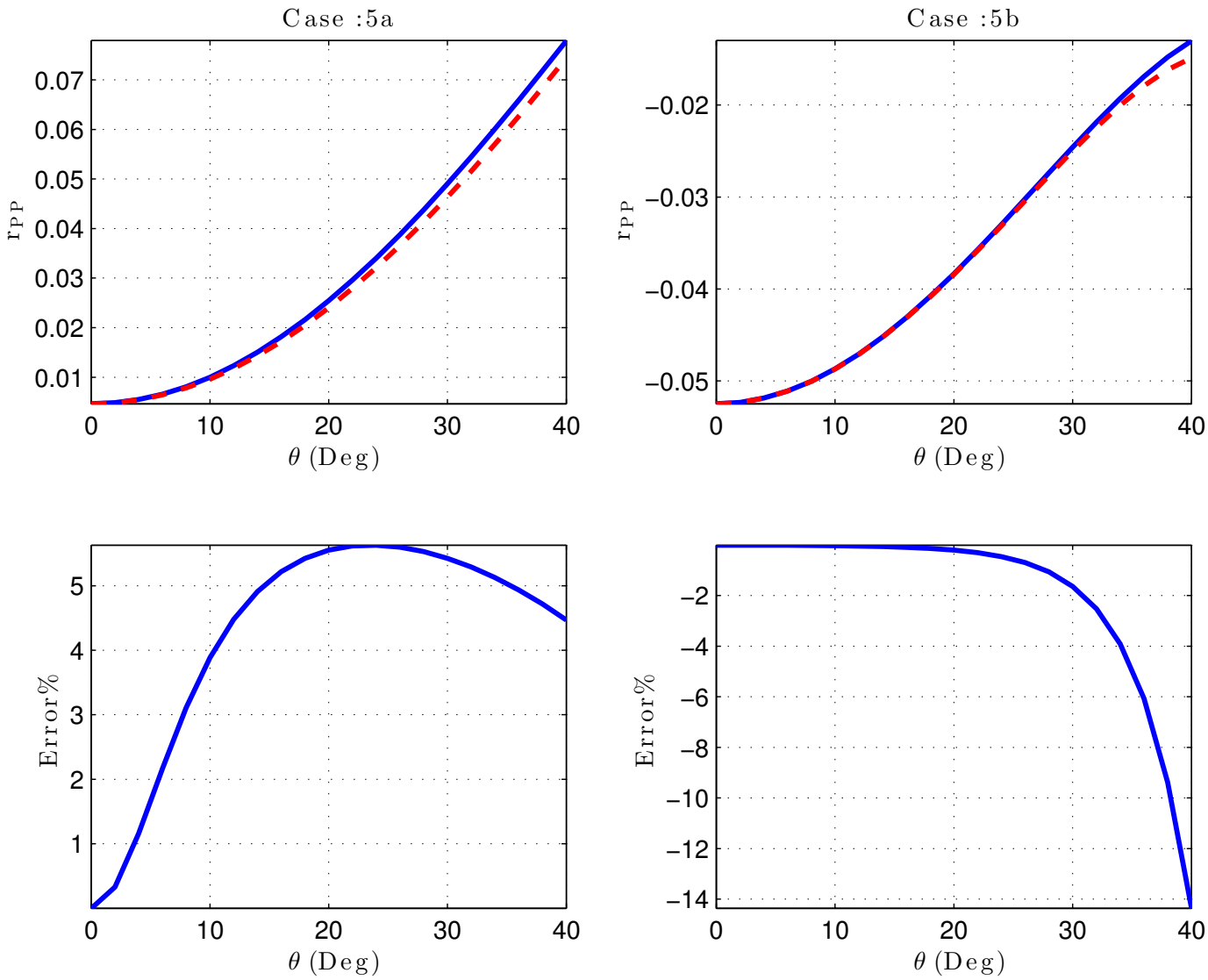

Figure 3.12: Comparison of reflection coefficients as a function of incidence angle using Aki-Richards (dashed red) approximation and exact Zoeppritz (solid blue). The saturation is $S_w = 95\%$ and the porosity is $\phi = 10\%$. An oil and water saturated reservoir on the left and a gas and water saturated reservoir on the right.

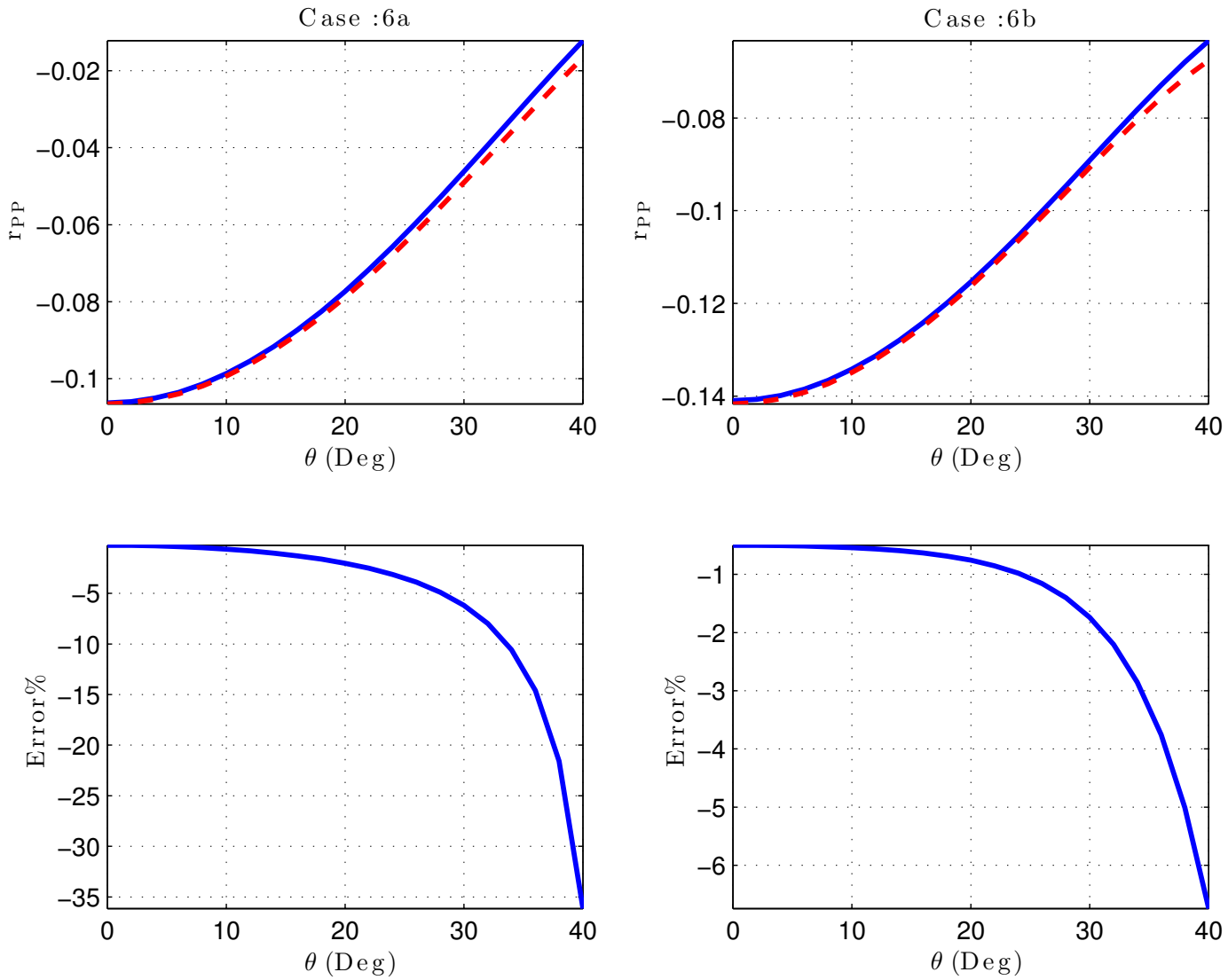

Figure 3.13: Comparison of reflection coefficients as a function of incidence angle using Aki-Richards (dashed red) approximation and exact Zoeppritz (solid blue). The saturation is $S_w = 95\%$ and the porosity is $\phi = 30\%$. An oil and water saturated reservoir on the left and a gas and water saturated reservoir on the right.

Chapter 4

Inversion theory

4.1 Discrete inverse problems

Inverse theory concerns the problem of making quantitative inferences about physical systems from indirect noisy measurements. A model, m, is a mathematical parameterization of those properties of a physical system that is required to predict the data, d. The data that is measured in an experiment always results in a finite number of observations such that we can represent the data as a vector, $\mathbf{d}$. In practice, it is also necessary to approximate the model by discretizing to a finite dimensional vector of parameters, $\mathbf{m}$. Commonly, it is assumed that we understand the fundamental physics adequately such that a forward model operator, $\mathbf{G}$, may be defined that relates the model parameters and the data. The discrete nonlinear inverse problem is as such defined as (Tarantola, 2005):

$$\mathbf{G}(\mathbf{m}) \approx \mathbf{d} \tag{4.1}$$

The noise in the data, $\boldsymbol{\eta}$, will partly consist of unmodelled physics and discretization effects, but it may also be contaminated by random errors, $\mathbf{e}$, that are not deterministically reproducible. Including these uncertainties in (4.1) will give (Aster et al., 2005):

$$\mathbf{G}(\mathbf{m}) = \mathbf{d}+\boldsymbol{\eta}+\mathbf{e} \tag{4.2}$$

However, it is common to assume that the forward model operator is accurate in inverse problems. In the case if discrete linear inverse problems, (4.2) can be written in the form of a linear system of algebraic equations:

$$\mathbf{Gm}=\mathbf{d}+\mathbf{e} \tag{4.3}$$

It is necessary to incorporate probability theory in order to make quantitative inferences about physical systems. However, there are two fundamental different meanings of what is meant by probability. In the frequentist approach, or the classical approach, there exists an unknown, but true model. It is

based solely on the data we acquire from the experiments that have been done. On the contrary, the model is itself a random variable in the Bayesian approach, and the problem is to provide a probability distribution of the model that provides all our available knowledge. Our knowledge about the model before the experiment is also incorporated into the solution. The prior information is expressed through a probability density function, $\mathrm{p}(\mathbf{m})$, and should be independent from the data. The second source of information is given by a conditional probability density function, the likelihood function, $\mathrm{f}(\mathbf{d}|\mathbf{m})$. It is a measure of how likely a model is to produce a set of data. After incorporating the experiment into our prior knowledge we obtain a posterior PDF, $\mathrm{q}(\mathbf{m}|\mathbf{d})$. Bayes' theorem can be stated as follows (Tarantola, 2005):

$$\mathrm{q}(\mathbf{m}|\mathbf{d}) = \frac{\mathrm{f}(\mathbf{d}|\mathbf{m})\mathrm{p}(\mathbf{m})}{\int_{\text{all models}} \mathrm{f}(\mathbf{d}|\mathbf{m})\mathrm{p}(\mathbf{m})\mathrm{d}\mathbf{m}} \tag{4.4}$$

In order to find the solution that best fit our data, we choose the model that minimizes a certain misfit, or objective function. A common basis for the measure of the misfit is the 2-norm of the residual vector. The residual vector is defined as the difference between the data and the theoretical predictions. The unconstrained model that minimize the 2-norm of the residual vector is the least squares solution (Aster et al., 2005). It is calculated by minimizing the following objective function, $\mathrm{J}(\mathbf{m})$:

$$\mathrm{J}(\mathbf{m}) = ||\mathbf{d}-\mathbf{G}(\mathbf{m})||_2^2 \tag{4.5}$$

Ill-posed behavior is a fundamental feature of most inverse problems, and may be characterized by the existence, uniqueness and instability of the solution. Existence refers to that there may be no model that exactly fits the data. Uniqueness implies that no unique solution may exist even if an exact solution exists. Finally, instability is concerned with that a small change in the data may lead to large change in the estimated model, and this is also known as ill-conditioned inverse problems. Regularization is the process of stabilizing the inversion process of such a problem by imposing constraints that bias the solution(Menke, 2012). A consequence of the limitations that are put on the solution is that the model resolution is decreased in order to improve the stability.

4.2 Linearized inversion

The least squares solution for a discrete linearized inverse problem is given by the normal equations:

$$\mathbf{G}^{\mathrm{T}}\mathbf{G}\mathbf{m}=\mathbf{G}^{\mathrm{T}}\mathbf{d} \tag{4.6}$$

$$\mathbf{m}_{\mathrm{L}_2}=\left(\mathbf{G}^{\mathrm{T}}\mathbf{G}\right)^{-1}\mathbf{G}^{\mathrm{T}}\mathbf{d} \tag{4.7}$$

In statistical terms, the least squares solution is said to be unbiased because the expected solution is the true model. However, the unconstrained solution is as mentioned very often ill-conditioned. That is, a small change in the data would give a large change in the estimated model.

4.2.1 Tikhonov regularization

Tikhonov regularization is a popular method, that is based upon the frequentist interpretation of probability, for stabilizing the solution by imposing constraints to it. It is implemented by minimizing a measure of the model, a penalty functional, in addition to the residual norm by the following objective function:

$$\mathrm{J}(\mathbf{m}) = \frac{1}{2}\,||\mathbf{G}\mathbf{m}-\mathbf{d}||_2^2 + \frac{\lambda^2}{2}\,||\mathbf{L}\mathbf{m}||_2^2 \tag{4.8}$$

where $\mathbf{L}$ is an appropriate finite difference operator, or roughening matrix, and λ is a regularization parameter. If the roughening matrix is chosen as the identity matrix it will minimize the norm, if it is a first-order derivative operator it will emphasize flatness of the solution, and a second-order derivative operator will emphasize smoothness. It is also possible to add multiple terms in order to emphasize on several aspects of the solution. The regularization parameter, λ, determines how hard the constraints on the solution should be. There exits an optimal value of the regularization parameter because a higher value will introduce an increasing bias into the solution. The optimal regularization parameter can be identified by methods such as the discrepancy principle, L-curve analysis or generalized cross-validation (Aster et al., 2005). In this thesis, we will find the optimal value of the regularization parameter by Morozovs discrepancy principle (Morozov et al., 1984). One should pick the largest regularization parameter such that the inverted model, $\mathbf{m}_\lambda$, fits the data to some tolerance, δ, based upon the length of the residual vector:

$$||\mathbf{G}\mathbf{m}_\lambda-\mathbf{d}||_2^2 \leq \delta \tag{4.9}$$

The solution of (4.8) is given by:

$$\mathbf{m}_\lambda = \left(\mathbf{G}^{\mathrm{T}}\mathbf{G} + \lambda^2\mathbf{L}^{\mathrm{T}}\mathbf{L}\right)^{-1}\mathbf{G}^{\mathrm{T}}\mathbf{d} \tag{4.10}$$

A generalized inverse matrix, $\mathbf{G}^{\#}$, may be defined from this:

$$\mathbf{G}^{\#} = \left(\mathbf{G}^{\mathrm{T}}\mathbf{G} + \lambda^2\mathbf{L}^{\mathrm{T}}\mathbf{L}\right)^{-1}\mathbf{G}^{\mathrm{T}} \tag{4.11}$$

It relates the inverse model to the data:

$$\mathbf{m}_\lambda = \mathbf{G}^{\#}\mathbf{d} = \mathbf{G}^{\#}\mathbf{d} \tag{4.12}$$

Resolution matrices, $\mathbf{R}_{\mathrm{m}_\lambda}$, are often used to get a qualitative idea of the bias in the solution:

$$\mathbf{R}_{\mathrm{m}_\lambda} = \mathbf{G}^{\#}\mathbf{G} \tag{4.13}$$

The blurring illustrated by the resolution matrix would occur even if the data contained no errors. It illustrates how well the inverse problem could be solved for perfect data for a given generalized inverse

(4.11) and forward model operator. The trace of the resolution matrix can be used as a measure of the bias because an unbiased solution has an identity covariance matrix.

It is also possible to put constraints on the solution that bias it towards an expected value, $\mathbf{m}_0$. A formulation of the optimization problem for a Tikhonov inversion with a prior is given by the following objective function:

$$\mathrm{J}(\mathbf{m}) = \frac{1}{2}||\mathbf{G}\mathbf{m}-\mathbf{d}||_2^2 + \frac{\lambda^2}{2}||\mathbf{L}\mathbf{m} - \mathbf{L}\mathbf{m}_0||_2^2 \tag{4.14}$$

The model that minimizes this objective fundtion is given by:

$$\mathbf{m}_\lambda = \left(\mathbf{G}^{\mathrm{T}}\mathbf{G} + \lambda^2\mathbf{L}^{\mathrm{T}}\mathbf{L}\right)^{-1}\left(\mathbf{G}^{\mathrm{T}}\mathbf{d} + \lambda^2\mathbf{L}^{\mathrm{T}}\mathbf{L}\mathbf{m}_0\right) \tag{4.15}$$

4.2.2 Bayesian linearized inversion

The general problem of Bayesian methods is to calculate the posterior distribution (4.4). There exists analytical solutions for a linear model given that the *a priori* information and data have multivariate normal distributions (Tarantola, 2005). The prior distribution has an expectation vector given by the prior model $\boldsymbol{\mu} = \mathbf{m}_0$, and an associated covariance matrix $\mathbf{C}_{\mathrm{m}_0}$:

$$\mathrm{p}(\mathbf{m}) = e^{-\frac{1}{2}(\mathbf{m}-\mathbf{m}_0)^{\mathrm{T}}\mathbf{C}_{\mathrm{m}_0}^{-1}(\mathbf{m}-\mathbf{m}_0)} \tag{4.16}$$

It is possible to incorporate data points with random errors into the calculation to find the best solution from a statistical point of view. A joint probability density function can be expressed as a conditional PDF for each observation if we have independent measurements. The likelihood function, $\mathrm{L}(\mathbf{d}|\mathbf{m})$, is then given as:

$$\mathrm{L}(\mathbf{d}|\mathbf{m}) = \mathrm{f}_1(\mathrm{d}_1|\mathbf{m}) \cdot \mathrm{f}_2(\mathrm{d}_2|\mathbf{m}) \cdots \mathrm{f}_{\mathrm{m}}(\mathrm{d}_{\mathrm{m}}|\mathbf{m}) \tag{4.17}$$

The Gaussian uncertainties in the data are given by a diagonal covariance matrix, $\mathbf{C}_{\mathrm{d}}$. According to the maximum likelihood principle, which is to select the model that maximizes the likelihood function, it can be written as:

$$\max \mathrm{L}(\mathbf{d}|\mathbf{m}) = \max \mathrm{f}(\mathbf{d}|\mathbf{m}) = e^{-\frac{1}{2}(\mathbf{G}\mathbf{m}-\mathbf{d})^{\mathrm{T}}\mathbf{C}_{\mathrm{d}}^{-1}(\mathbf{G}\mathbf{m}-\mathbf{d})} \tag{4.18}$$

It is possible to find analytical expression for the the maximum a posteriori solution, $\mathbf{m}_{\mathrm{map}}$ and the associated posterior covariance matrix, $\mathbf{C}_{\mathrm{m}'}$. The starting point is to note that it is not necessary to solve the integral in (4.4):

$$\mathrm{q}(\mathbf{m}|\mathbf{d}) \propto \mathrm{f}(\mathbf{d}|\mathbf{m})\mathrm{p}(\mathbf{m}) \tag{4.19}$$

The arguments in the distributions can then be set equal to the posterior distribution:

$$-\frac{1}{2}\left(\mathbf{Gm}-\mathbf{d}\right)^{\mathrm{T}}\mathbf{C}_{\mathrm{d}}^{-1}\left(\mathbf{Gm}-\mathbf{d}\right)-\frac{1}{2}\left(\mathbf{m}-\mathbf{m}_0\right)^{\mathrm{T}}\mathbf{C}_{\mathrm{m}_0}^{-1}\left(\mathbf{m}-\mathbf{m}_0\right)= \\ -\frac{1}{2}\left(\mathbf{m}-\mathbf{m}_{\mathrm{map}}\right)^{\mathrm{T}}\mathbf{C}_{\mathrm{m}'}^{-1}\left(\mathbf{m}-\mathbf{m}_{\mathrm{map}}\right) \tag{4.20}$$

This is equivalent to minimizing an objective function, $\mathrm{J}\left(\mathbf{m}\right)$:

$$\mathrm{J}\left(\mathbf{m}\right)=\frac{1}{2}\left(\mathbf{Gm}-\mathbf{d}\right)^{\mathrm{T}}\mathbf{C}_{\mathrm{d}}^{-1}\left(\mathbf{Gm}-\mathbf{d}\right)+\frac{1}{2}\left(\mathbf{m}-\mathbf{m}_0\right)^{\mathrm{T}}\mathbf{C}_{\mathrm{m}_0}^{-1}\left(\mathbf{m}-\mathbf{m}_0\right) \tag{4.21}$$

It can be shown that this is a standard linear least squares problem (4.7). The maximum a posteriori solution is given by the following expression:

$$\mathbf{m}_{\mathrm{map}}=\left(\mathbf{G}^{\mathrm{T}}\mathbf{C}_{\mathrm{d}}^{-1}\mathbf{G}+\mathbf{C}_{\mathrm{m}_0}^{-1}\right)^{-1}\left(\mathbf{G}^{\mathrm{T}}\mathbf{C}_{\mathrm{d}}^{-1}\mathbf{d}+\mathbf{C}_{\mathrm{m}_0}^{-1}\mathbf{m}_0\right) \tag{4.22}$$

The associated posteriori covariance matrix is given by (Tarantola, 2005):

$$\mathbf{C}_{\mathrm{m}'}=\left(\mathbf{G}^{\mathrm{T}}\mathbf{C}_{\mathrm{d}}^{-1}\mathbf{G}+\mathbf{C}_{\mathrm{m}_0}^{-1}\right)^{-1} \tag{4.23}$$

It is common to interpret the results by calculating confidence intervals from the diagonal elements of the posterior covariance matrix. The 95% confidence intervals are for instance given by (Aster et al., 2005):

$$\mathbf{m}\pm 1.96\cdot\mathrm{diag}\left(\mathbf{C}_{\mathrm{m}'}\right) \tag{4.24}$$

4.3 Bayesian nonlinear inversion

The solution of a posterior PDF (4.4) based on Gaussian statistics is given by:

$$\mathrm{q}\left(\mathbf{m}|\mathbf{d}\right)=\mathrm{N}\mathrm{e}^{-\mathrm{J}(\mathbf{m})} \tag{4.25}$$

where N is a normalization constant. Following a similar argument as for the linearized case, the objective function is given by (Tarantola, 2005):

$$\mathrm{J}\left(\mathbf{m}\right)=\frac{1}{2}\Big[\left(\mathbf{G}\left(\mathbf{m}\right)-\mathbf{d}\right)^{\mathrm{T}}\mathbf{C}_{\mathrm{d}}^{-1}\left(\mathbf{G}\left(\mathbf{m}\right)-\mathbf{d}\right)+\left(\mathbf{m}-\mathbf{m}_{\mathrm{prior}}\right)^{\mathrm{T}}\mathbf{C}_{\mathrm{m}}^{-1}\left(\mathbf{m}-\mathrm{m}_{\mathrm{prior}}\right)\Big] \tag{4.26}$$

If we have an uninformative prior (4.25) reduces to only a term describing the likelihood function multiplied by a normalization constant:

$$\mathrm{q}\left(\mathbf{m}|\mathbf{d}\right)=\mathrm{N}e^{-\frac{1}{2}\left(\mathbf{G}(\mathbf{m})-\mathbf{d}\right)^{\mathrm{T}}\mathbf{C}_{\mathrm{d}}^{-1}\left(\mathbf{G}(\mathbf{m})-\mathbf{d}\right)} \tag{4.27}$$

The posterior PDF is a joint probability density function for the model parameters. In order to quantify the uncertainties in the inverted model parameters, a calculation of marginal PDFs is required (Tarantola, 2005):

$$\mathrm{q_i}\left(\mathrm{m_i}\right) = \int \mathrm{q}\left(\mathbf{m}|\mathbf{d}\right) \mathrm{dm_1} \cdots \mathrm{dm_{i-1}} \mathrm{dm_{i+1}} \cdots \mathrm{dm_n} \tag{4.28}$$

The integral over the entire model space must be equal to unity, and (4.30) can be used to find the normalization constant in (4.25):

$$\int_{\text{all models}} \mathrm{N} \mathrm{e}^{-\mathrm{J}(\mathbf{m})} = 1 \tag{4.29}$$

$$\int_{\text{all models}} \mathrm{e}^{-\mathrm{J}(\mathbf{m})} = \frac{1}{\mathrm{N}} \tag{4.30}$$

Marginal PDFs (4.28) can be found by numerical integration with respect to the other model parameters or by Monte Carlo simulation. Finding the marginal PDFs by numerical integration requires us to discretize the forward model dense enough to incorporate all the features of the posterior PDF (4.25).

Chapter 5

One-step inversion methods

5.1 Introduction

Conventionally, effective elastic reservoir parameters have been obtained by three parameter AVA inversion for a single interface. Following this, a rock physics model can act as a link between reservoir parameters, such as water saturation and porosity, and the effective elastic reservoir properties that is used for a second inversion step (Avseth et al., 2005). The first inversion step from AVA data to elastic properties can be performed by either nonlinear inversion methods (Dahl and Ursin, 1991; Gouveia and Scales, 1998) or linearized inversion methods (Lörtzer and Berkhout, 1992; Smith and Gidlow, 1987). Linearized estimates may simplify the study of the relation between AVA data and effective elastic reservoir properties in the event of weak contrasts in elastic properties across a reflector. The main drawback in using linearized estimates is that the accuracy may not always be satisfactory. An error analysis for the forward modelling of AVA data using the full Zoeppritz equations and Aki-Richards approximation for varying reservoir models was done in chapter 3. However, it was not yet clear what implications the accuracy of Aki-Richards approximation had for determination of water saturation and porosity. In order to investigate this relation, we performed inversion tests from AVA data to saturation and porosity using either Aki-Richards approximation or the full Zoeppritz equations using the same reservoir models as in chapter 3. It was imperative to obtain unbiased estimates of water saturation and porosity in order to identify the effect of the AVA modelling error. Nonlinear inversion approaches are generally more robust than linearized inversion approaches (Sambridge and Mosegaard, 2002). One-step unregularized inversion approaches directly from AVA data to water saturation and porosity were therefore chosen.

5.2 Amplitude versus angle inversion tests

5.2.1 Inversion procedure

A nonlinear Bayesian approach, as discussed in section 4.3, was adopted to do the inversion from AVA data, $\mathbf{r}_{\mathrm{PP}}(\theta)$, to a reservoir model determined by saturation and porosity, $\mathbf{m}_{\mathrm{res}} = (\mathrm{S_w}, \phi)$ in one step. This was done for a know overburden (table 3.1) such that the AVA data only was a function of saturation and porosity, $\mathbf{r}_{\mathrm{PP_{calc}}} = \mathbf{G}(\mathbf{m}_{\mathrm{res}})$. It was assumed that the AVA data were uncorrelated and had Gaussian uncertainties defined by a diagonal covariance matrix, $\mathbf{C}_{\mathrm{d}}$. An uninformative prior was implemented such that the objective function, $\mathrm{J}(\mathbf{m}_{\mathrm{res}})$, was given by:

$$\mathrm{J}(\mathbf{m}_{\mathrm{res}}) = \frac{1}{2}\left(\mathbf{G}(\mathbf{m}_{\mathrm{res}}) - \mathbf{r}_{\mathrm{PP}}\right)^{\mathrm{T}} \mathbf{C}_{\mathrm{d}}^{-1}\left(\mathbf{G}(\mathbf{m}_{\mathrm{res}}) - \mathbf{r}_{\mathrm{PP}}\right) \tag{5.1}$$

A solution to the posterior PDF based on Gaussian statistics is given by (4.25).

$$\mathrm{q}(\mathbf{m}_{\mathrm{res}}|\mathbf{r}_{\mathrm{PP}}) = \mathrm{N}\mathrm{e}^{-\mathrm{J}(\mathbf{m}_{\mathrm{res}})} \tag{5.2}$$

The first step was to calculate the normalization constant (4.30) which in our case was given by:

$$\frac{1}{\mathrm{N}} = \int_{\mathrm{S_w}=0}^{\mathrm{S_w}=1}\int_{\phi=0}^{\phi=0.4} \mathrm{e}^{-\mathrm{J}(\mathbf{m}_{\mathrm{res}})}\mathrm{d}\phi\mathrm{dS_w} \tag{5.3}$$

The model was further discretized into K grid points for ϕ, such that $\Delta\phi = 0.0025$, and into L grid points for $\mathrm{S_w}$, such that $\Delta\mathrm{S_w} = 0.025$. The integral was evaluated by numerical integration by the trapezoidal rule:

$$\frac{1}{\mathrm{N}} \approx \frac{\Delta\mathrm{S_w}\Delta\phi}{4}\sum_{\mathrm{k}=1}^{\mathrm{K}}\sum_{\mathrm{l}=1}^{\mathrm{L}}\left[\mathrm{e}^{-\mathrm{J}\left(\phi_{\mathrm{k}+1},\mathrm{S_{w_{l+1}}}\right)} + \mathrm{e}^{-\mathrm{J}\left(\phi_{\mathrm{k}},\mathrm{S_{w_l}}\right)}\right] \tag{5.4}$$

This was feasible since the number of model parameters we inverted for was only two. Once the normalization constant had been obtained, the posterior PDFs for each of the cases were found by (4.27). The corresponding marginal PDF (4.28) for water saturation is given by:

$$\mathrm{q_{S_w}}(\mathrm{S_w}) \approx \mathrm{N}\cdot\frac{\Delta\phi}{2}\sum_{\mathrm{k}=1}^{\mathrm{K}}\left[\mathrm{e}^{-\mathrm{J}(\phi_{\mathrm{k}+1},\mathbf{S_w})} + \mathrm{e}^{-\mathrm{J}(\phi_{\mathrm{k}},\mathbf{S_w})}\right] \tag{5.5}$$

and for porosity as:

$$\mathrm{q}_{\phi}(\phi) \approx \mathrm{N}\cdot\frac{\Delta\mathrm{S_w}}{2}\sum_{\mathrm{l}=1}^{\mathrm{L}}\left[\mathrm{e}^{-\mathrm{J}\left(\boldsymbol{\phi},\mathrm{dS_{w_{l+1}}}\right)} + \mathrm{e}^{-\mathrm{J}\left(\boldsymbol{\phi},\mathrm{dS_{w_l}}\right)}\right] \tag{5.6}$$

It was thus possible to find global maximum a posteriori solutions for the model parameters since we were able to calculate the exact marginal PDFs.

In what follows, 'true' reflection AVA data was generated by using a combination of the rock physics

models with varying porosity and saturation from chapter 3 (table 3.2) and the Zoeppritz equations. The standard deviations associated with the true data, σ_{i}, were 5% of the corresponding reflection coefficient, and the diagonal elements of the data covariance matrix, $\mathbf{C}_{\mathrm{d}}$, were thus given by:

$$\sigma_{\mathrm{i}}^2 = \left(0.05 \cdot \mathrm{r_{PP}}\left(\theta_{\mathrm{i}}\right)\right)^2 \tag{5.7}$$

The aim was to recover the true reservoir parameters from synthetic reflection coefficient data that was obtained by forward modelling by Aki-Richards approximations as well as the exact Zoeppritz equations. That is, the forward model operator, $\mathbf{G}$, differ for the two methods, but the observed AVA data remained the same. The work flow is summarized in figure 5.1.

5.2.2 Inversion results

Figures 5.2 to 5.13 show the results for cases with varying porosity and saturations listed in table 3.2). The same choice of reservoir parameters is shown for alternating oil-water (case a) and gas-water (case b) pore fluid in order to demonstrate the effect of the sensitivity of the reservoir model. The lower plots in each figure represent the marginal PDFs for the water saturation, $\mathrm{S_w}$, and the porosity, ϕ. Marginal PDFs obtained using the Zoeppritz equations and Aki-Richards approximation, are shown as solid blue lines and the dashed red lines respectively. The corresponding normalized *a posteriori* distributions are shown in the upper plots: The forward model for the upper left plots are calculated by Aki-Richards approximation and the upper right plots are calculated by the Zoeppritz equations.

CASE 1a. The true set of parameters that were inverted for were $\mathrm{S_w} = 10\%$ and $\phi = 10\%$ for an oil-water saturated reservoir rock. Figure 5.2 shows the normalized a posteriori distributions for this particular case and the corresponding marginal PDFs. Clearly, the maximum of the marginal PDFs obtained via the exact reflection coefficients were close to the true values. There was only a very small overestimate for Aki-Richards approximation (dashed red) relative to the exact reflection coefficients (solid blue) for porosity. However, there was a shift in saturation for Aki-Richards approximation such that there was an overestimate in water saturation of about 10%. In this particular case, we may conclude that Aki-Richards approximation introduced significant error for the inversion of water saturation, but the porosity had an acceptable solution with small uncertainty.

CASE 1b. The true set of parameters that were inverted for were $\mathrm{S_w} = 10\%$ and $\phi = 10\%$ for a gas-water saturated reservoir rock. Figure 5.3 shows the normalized a posteriori distributions for this particular case and the corresponding marginal PDFs. Clearly, the maximum of the marginal PDFs obtained via the exact reflection coefficients were close to the true values. However, the for the marginal PDFs obtained via Aki-Richards approximation, the maximum presented a large overestimate in water saturation with a large uncertainty. There was a minor shift to the right for the maximum of the porosity with a relatively small uncertainty. The Aki-Richards approximation introduced significant error for the inversion of water saturation, but the porosity estimate was acceptable in this particular

case.

CASE 2a. The true set of parameters that were inverted for were $S_w = 10\%$ and $\phi = 30\%$ for an oil-water saturated reservoir rock. Figure 5.4 shows the normalized a posteriori distributions for this particular case and the corresponding marginal PDFs. Again, the maximum of the marginal PDFs obtained via the exact reflection coefficients were close to the true values. There was a a very small overestimate in porosity for Aki-Richards approximation with a relatively narrow distribution, although wider than for case 1. However, there was an overestimate of about 20% in water saturation with a wide distribution, which implied large uncertainty in the estimate. We may conclude that the water saturation estimate was unsatisfactory, but the porosity estimate was acceptable in this case.

CASE 2b. The true set of parameters that were inverted for were $S_w = 10\%$ and $\phi = 30\%$ for a gas-water saturated reservoir rock. Figure 5.5 shows the normalized a posteriori distributions for this particular case and the corresponding marginal PDFs. Again, the maximum of the marginal PDFs obtained via the exact reflection coefficients were close to the true values. However, for the marginal PDFs obtained via Aki-Richards approximation, the maximum presented a large overestimate in water saturation with a large uncertainty. There was a minor shift to the right for the maximum of the porosity with a moderate uncertainty. The approximation introduced significant error for the inversion of water saturation, but the porosity estimate was acceptable in this particular case.

CASE 3a. The true set of parameters that were inverted for were $S_w = 50\%$ and $\phi = 10\%$ for an oil-water saturated reservoir rock. Figure 5.6 shows the normalized a posteriori distributions for this particular case and the corresponding marginal PDFs. The maximum of the marginal PDFs for both water saturation and porosity were close to the true values for the exact reflection coefficients. There was a small overestimate in saturation (5%) with a narrow distribution, and a minute shift to the right with a narrow distribution from the true porosity value for Aki-Richards approximation. We may conclude that the results were very satisfactory in this case.

CASE 3b. The true set of parameters that were inverted for were $S_w = 50\%$ and $\phi = 10\%$ for a gas-water saturated reservoir rock. Figure 5.7 shows the normalized a posteriori distributions for this particular case and the corresponding marginal PDFs. The maximum of the marginal PDFs obtained via the exact reflection coefficients were close to the true values, but for the marginal PDFs obtained via Aki-Richards approximation, the maximum had a large overestimate in the case of water saturation with a high uncertainty. A small overestimate with a small uncertainty was observed in the corresponding maximum for porosity. We may conclude that the water saturation estimate was unsatisfactory, but the porosity estimate was satisfactory in this particular case.

CASE 4a. The true set of parameters that were inverted for were $S_w = 50\%$ and $\phi = 30\%$ for an oil-water saturated reservoir rock. Figure 5.8 shows the normalized a posteriori distributions for this particular case and the corresponding marginal PDFs. Clearly, the maximum of the marginal PDFs obtained via the exact reflection coefficients were close to the true values. There was only a very small overestimate for Aki-Richards approximation for porosity with a narrow distribution. However,

there was a shift in saturation for Aki-Richards approximation such that therewas an overestimate in water saturation of about 10% with a relatively wide distribution. We may conclude that the water saturation estimate was unsatisfactory, but the porosity estimate was acceptable in this case.

CASE 4b. The true set of parameters that were inverted for were $S_w = 50\%$ and $\phi = 30\%$ for a gas-water saturated reservoir rock. Figure 5.9 shows the normalized a posteriori distributions for this particular case and the corresponding marginal PDFs. Again, the maximum of the marginal PDFs obtained via the exact reflection coefficients were close to the true values. However, for the marginal PDFs obtained via Aki-Richards approximation, the maximum presented a large overestimate in water saturation with a large uncertainty. There was a minor shift to the right for the maximum of the porosity with a moderate uncertainty. The approximation introduced significant error for the inversion of water saturation, but the porosity estimate was acceptable in this particular case.

CASE 5a. The true set of parameters that were inverted for were $S_w = 95\%$ and $\phi = 10\%$ for an oil-water saturated reservoir rock. Figure 5.10 shows the normalized a posteriori distributions for this particular case and the corresponding marginal PDFs. The maximum of the marginal PDFs for both water saturation and porosity were close to the true values for the exact reflection coefficients. There were only minute shifts to the right from the true porosity and the true water saturation for Aki-Richards approximation. Also, the distributions were very narrow, which implies low uncertainties. We may conclude that the results were very satisfactory in this case.

CASE 5b. The true set of parameters that were inverted for were $S_w = 95\%$ and $\phi = 10\%$ for a gas-water saturated reservoir rock. Figure 5.11 shows the normalized a posteriori distributions for this particular case and the corresponding marginal PDFs. Clearly, the maximum of the marginal PDFs were close to the true values for both saturation and porosity for the exact reflection coefficients. There was only a very small overestimate for Aki-Richards approximation for porosity, and no observable shift in water saturation. Also, there are very low uncertainties in the both the estimates obtained from Aki-Richards approximation and from the exact reflection coefficients. We may conclude that the results were very satisfactory in this case.

CASE 6a. The true set of parameters that were inverted for were $S_w = 95\%$ and $\phi = 30\%$ for an oil-water saturated reservoir rock. Figure 5.10 shows the normalized a posteriori distributions for this particular case and the corresponding marginal PDFs. Again, the maximum of the marginal PDFs for both water saturation and porosity were close to the true values for the exact reflection coefficients, and there were only minute shifts to the right from the true porosity and the true water saturation for Aki-Richards approximation. The distributions were even narrower than for case 5. We may conclude that the results were very satisfactory in this case.

CASE 6b. The true set of parameters that were inverted for were $S_w = 95\%$ and $\phi = 30\%$ for a gas-water saturated reservoir rock. Figure 5.13 shows the normalized a posteriori distributions for this particular case and the corresponding marginal PDFs. Again, the maximum of the marginal PDFs were close to the true values for both saturation and porosity for the exact reflection coefficients. There

was no observable shift in water saturation and a small underestimate in porosity from the maximum of the marginal PDFs for the reflection coefficients obtained by Aki-Richards approximation. The distributions were also narrow for both the exact and approximate reflection coefficients. However, the marginal PDFs for porosity were multimodal, but the smaller peak was relatively insignificant compared to the maximum peak. We may conclude that Aki-Richards approximation did not introduce any significant error for the inversion of the reservoir parameters in this case.

5.3 Synthetic data examples

5.3.1 A random Gaussian reservoir model

Reservoirs are in reality complex media which may exhibit a large degree of spatial variation. The pore geometry that was used in the rock physics model pose an uncertainty for AVA inversion. Calibrations that were done for the rock physics model are maybe exact in the immediate vicinity of the well. A variable crack density would not only affect the dry rock properties, but would also have implications for the spatial variability of saturation through variable permeability (Guéguen and Palciauskas, 1994). The heterogeneity of a reservoir model may be modelled by adding random Gaussian perturbations to the rock physics parameters, $\mathrm{m_{res_i}}$. Spatial correlations may be modelled by an autocorrelation function on the form (Baig and Dahlen, 2004):

$$\mathrm{N_g}\left(||\mathbf{x}-\mathbf{x}'||\right) = \tau^2 {\mathrm{m_{res_i}}}^2 \mathrm{e}^{\left(-\frac{||\mathbf{x}-\mathbf{x}'||}{\mathrm{a}^2}\right)} \tag{5.8}$$

where a is the correlation length and τ is the RMS strength of the percentage heterogeneity in the model parameter given as:

$$\tau = \frac{\delta {\mathrm{m_{res_i}}}^2(\mathbf{x})}{{\mathrm{m_{res_i}}}^2} \tag{5.9}$$

An oil and water saturated reservoir model was constructed using the procedure in chapter 2 with a basis in the reservoir parameters in tables 2.1 and 2.2. The number of grid blocks was set to 51 for an inline and cross line distance from 0 m to 1040 m. A background porosity was chosen as $\phi = 30\%$ and a background crack density was chosen as $\epsilon = 0.8533$. Heterogeneities were added by setting the correlation length to a = 100 meters with RMS strengths of the percentage heterogeneity for porosity set to 0.08 and for crack density to 0.04. Following this, the water saturation was set to either $\mathrm{S_w} = 50\%$ or $\mathrm{S_w} = 10\%$ depending on a higher or lower crack density than the background crack density. Figure 5.14 shows the resulting spatial distributions of the true reservoir parameters. The corresponding effective elastic reservoir properties are shown in figure 5.15.

5.3.2 Inversion tests with variable and constant crack density

'True' PP-reflection coefficient data were generated for each grid block in the reservoir model using the Zoeppritz equations. The overburden (table 3.1) and range of incident angles (0° to 40°) were as before. Also, the Gaussian data uncertainties were set to 5% of the corresponding reflection coefficient as before. The work flow for the AVA inversion (figure 5.1) was the same as for a single grid block with some modifications. Effective elastic properties were calculated for both a reservoir model with the true crack densities and a reservoir model with constant crack density. Synthetic reflection coefficient data was then obtained by forward modelling with the Zoeppritz equations and the Aki-Richards approximation. The aim was to investigate what implications modelling error due to variable crack density would have for the inverse problem. Maximum a posteriori solutions were found for each grid block using the by minimizing the objective function (5.1) by a systematic search method. However, there was not performed any uncertainty analysis in this case.

Figures 5.16 and 5.16 show the inversion results for porosity. In each figure, the top plot is the true model, the centre plot is the inversion results using the true crack density and the bottom plot is the inversion results using a constant crack density equal to the background crack density. The inversion results obtained by forward modelling with the Zoeppritz equations are shown in figure 5.16. Clearly, the inversion results using the exact crack density were very satisfactory. There were only minute differences to the true model. It was apparent that the accuracy of the inversion results using the constant crack density was decreased. Next, the inversion results obtained by forward modelling with Aki-Richards approximation are shown in figure 5.17. Clearly, the inversion results using the exact crack density were satisfactory. Again, the accuracy of the inversion results using the constant crack density was decreased. We may conclude that the modelling errors introduced by assuming constant crack density has a greater effect than the modelling errors introduced by Aki-Richards approximation for porosity estimates.

Figures 5.18 and 5.19 show the inversion results for water saturation. In each figure, the top plot is the true model, the centre plot is the inversion results using the true crack density and the bottom plot is the inversion results using a constant crack density equal to the background crack density. The inversion results obtained by forward modelling with the Zoeppritz equations are shown in figure 5.18. Clearly, the inversion results using the exact crack density were very satisfactory. There were only minute differences to the true model. It was apparent that the accuracy of the inversion results using the constant crack density was decreased. Next, the inversion results obtained by forward modelling with Aki-Richards approximation are shown in figure 5.19. The inversion results using the exact crack density were unsatisfactory. Again, the accuracy of the inversion results using the constant crack density was decreased. We may conclude that the modelling errors introduced by Aki-Richards approximation is sufficient to cause inaccurate water saturation estimates.

5.4 Discussion

In the forward modelling, the effective elastic properties for a choice of reservoir parameters were first calculated. Thus, the relative error in the reflection coefficients obtained from Aki-Richards approximation compared to the exact reflection coefficients depend on the combined change in P-wave velocity, S-wave velocity and density over a boundary. High magnitudes of relative error were caused by intermediate contrasts in all three elastic parameters, or by a high contrast in a single elastic parameter. Therefore there was no direct correlation between the magnitude of the relative error in the reflection coefficients and reservoir properties. However, it was apparent that the relative error increased for higher incident angles.

In the AVA inversion test, the accuracy depends both on the sensitivity of the reservoir model with respect to saturation and porosity and the contrast in elastic properties. A more rapid change in elastic properties will allow for higher relative contrasts in elastic properties while the level of accuracy is maintained. This proved to be the case for both a gas-water and an oil-water saturated pore fluid. Thus, the static reservoir parameters (table 2.1) posed a significant source of error since the accuracy depends on the sensitivity of the reservoir model. The accuracy of the porosity estimates were satisfactory for all the chosen cases. However, the water saturation estimates were generally only satisfactory for high water saturations, for which the reservoir model was especially sensitive. An exemption from this observation was case 3 which had successful water saturation and porosity estimates with low uncertainty. This was due to the especially low contrasts in elastic properties for this case.

The static rock physics parameter may have large implications for the accuracy of saturation and porosity estimates. Assumptions about constant crack density in a reservoir with variable crack density was especially important for porosity estimates. The modelling error in crack density was more dominant than the modelling error introduced by Aki-Richards approximation. Conversely, Aki-Richards approximation dominant to modelling errors in crack density for water saturation estimates.

The main conclusion is that it is generally safer to use the Zoeppritz equations for porosity and water saturation estimates. However, Aki-Richards approximation seems to give satisfactory results for porosity estimates with relatively low uncertainties. This can prove useful since linearized estimates are less computationally expensive.

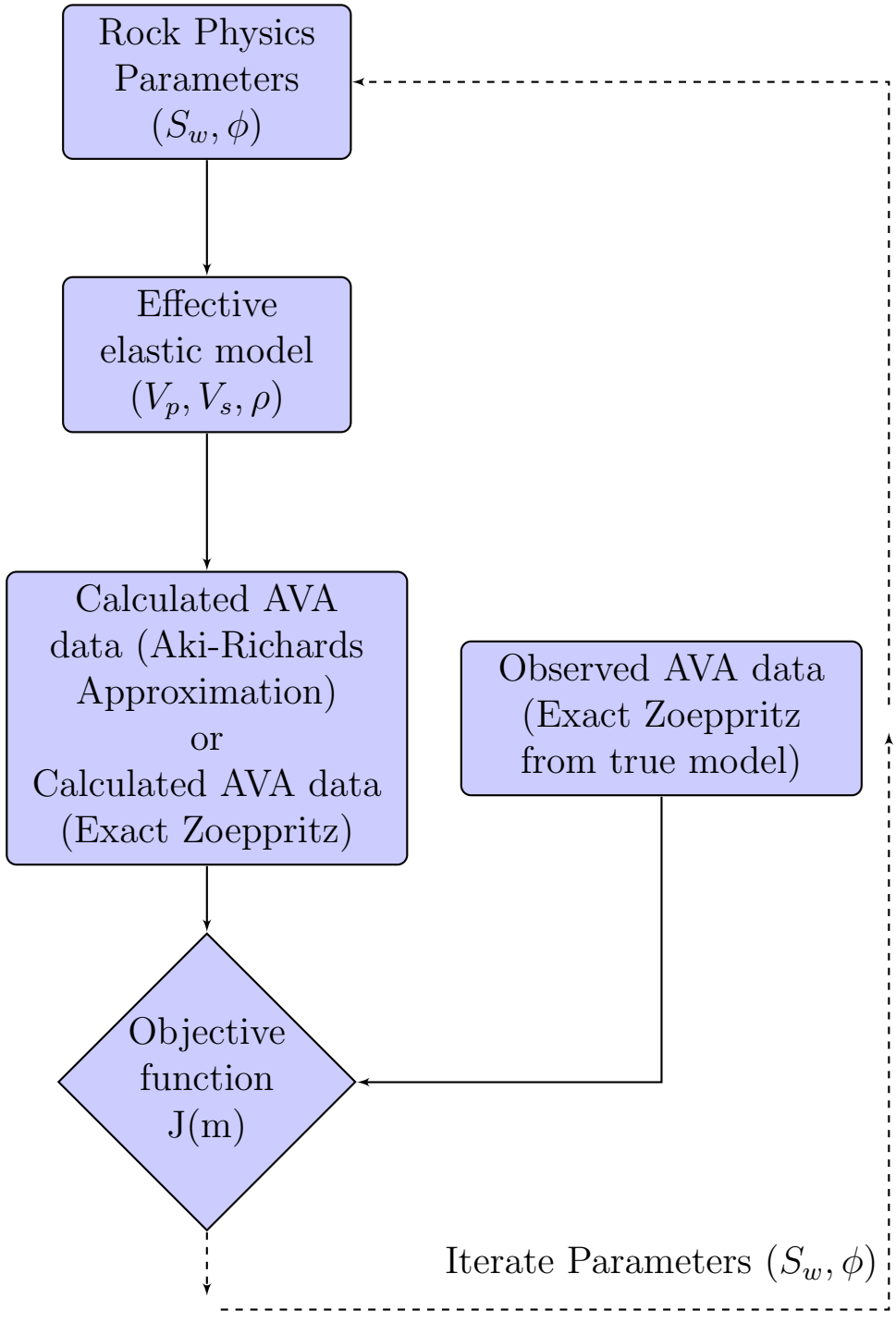

Figure 5.1: Schematic work flow diagram for estimation of porosity and saturation from inversion of AVA data using a rock physics model.

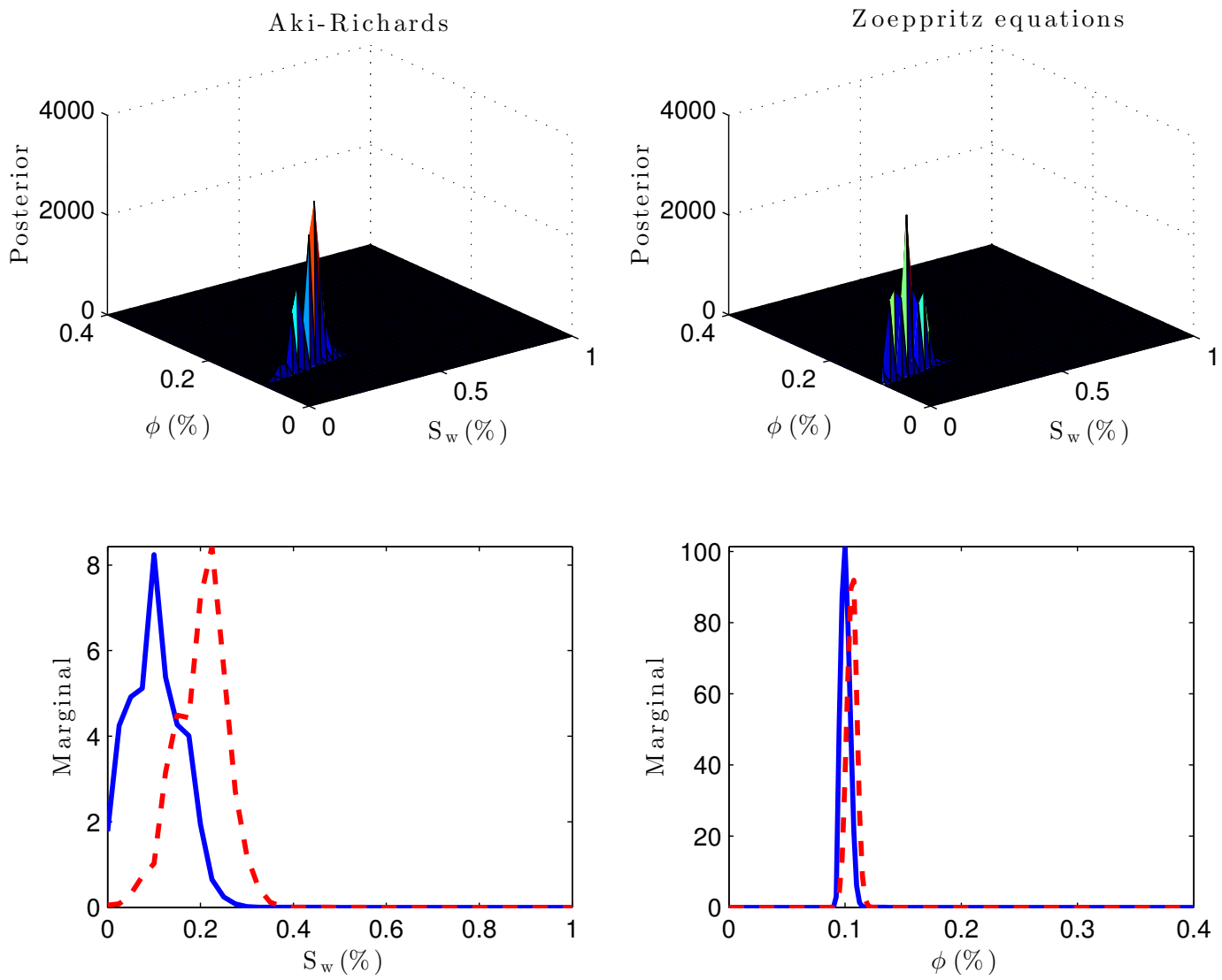

Figure 5.2: An oil and water saturated reservoir ($S_w = 10\%, \phi = 10\%$). The posterior distribution for Aki-Richards approximation (top left) and the Zoeppritz equations (top right). The corresponding marginal distributions for water saturation (bottom left) and porosity (bottom right). The dashed lines are for Aki-Richards approximation and the full line is for the Zoeppritz equations.

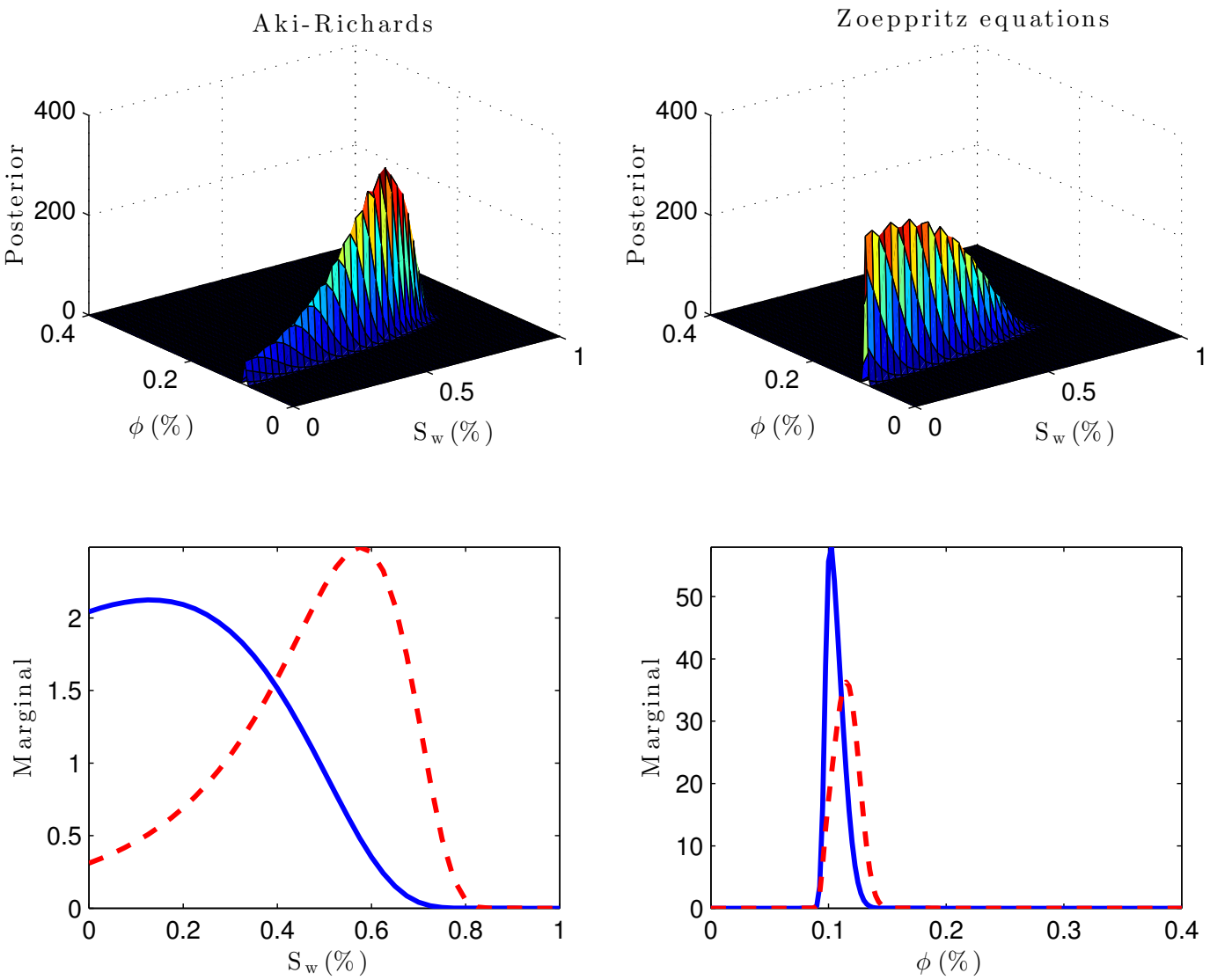

Figure 5.3: A gas and water saturated reservoir ($S_w = 10\%, \phi = 10\%$). The posterior distribution for Aki-Richards approximation (top left) and the Zoeppritz equations (top right). The corresponding marginal distributions for water saturation (bottom left) and porosity (bottom right). The dashed lines are for Aki-Richards approximation and the full line is for the Zoeppritz equations.

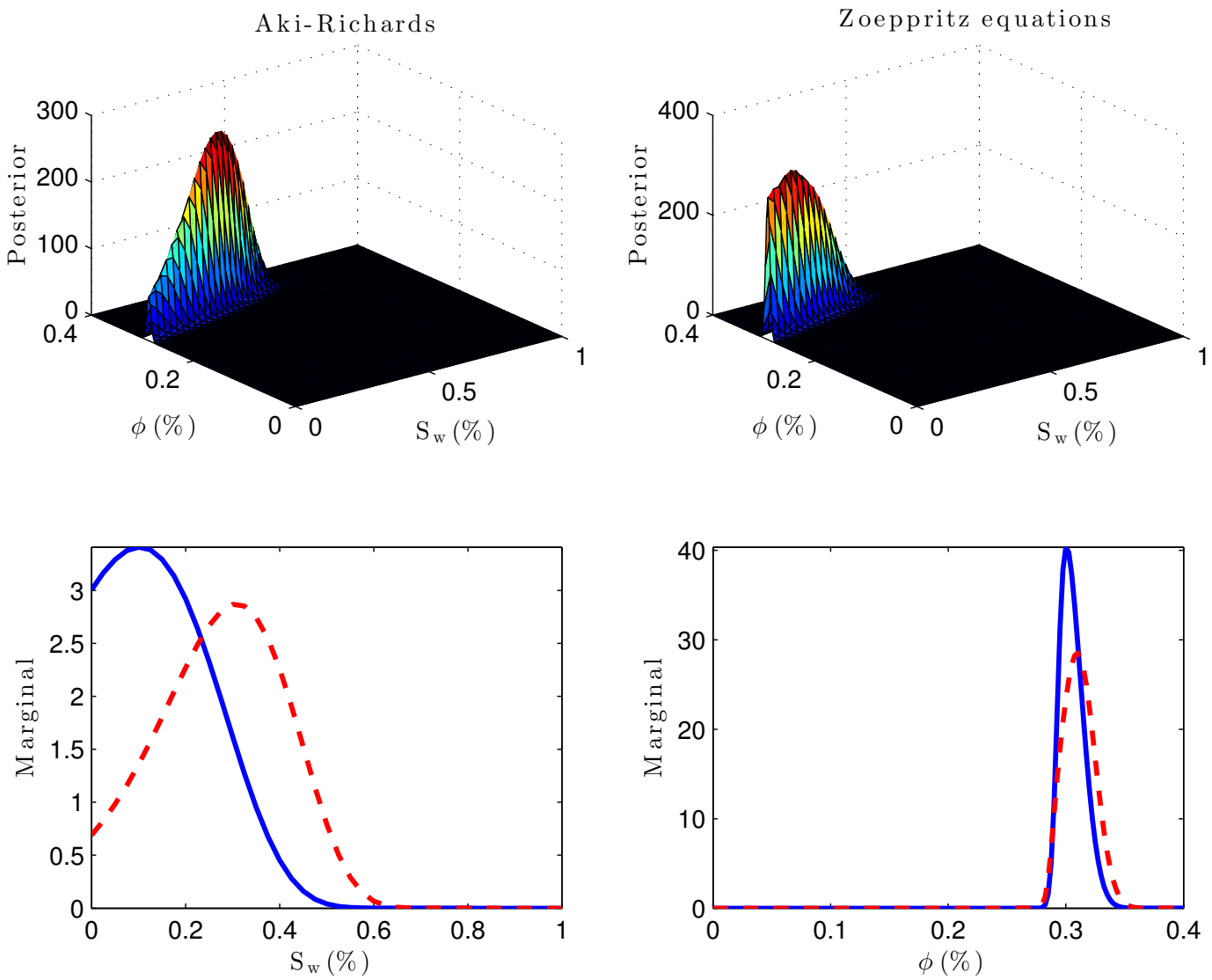

Figure 5.4: An oil and water saturated reservoir ($S_w = 10\%, \phi = 30\%$). The posterior distribution for Aki-Richards approximation (top left) and the Zoeppritz equations (top right). The corresponding marginal distributions for water saturation (bottom left) and porosity (bottom right). The dashed lines are for Aki-Richards approximation and the full line is for the Zoeppritz equations.

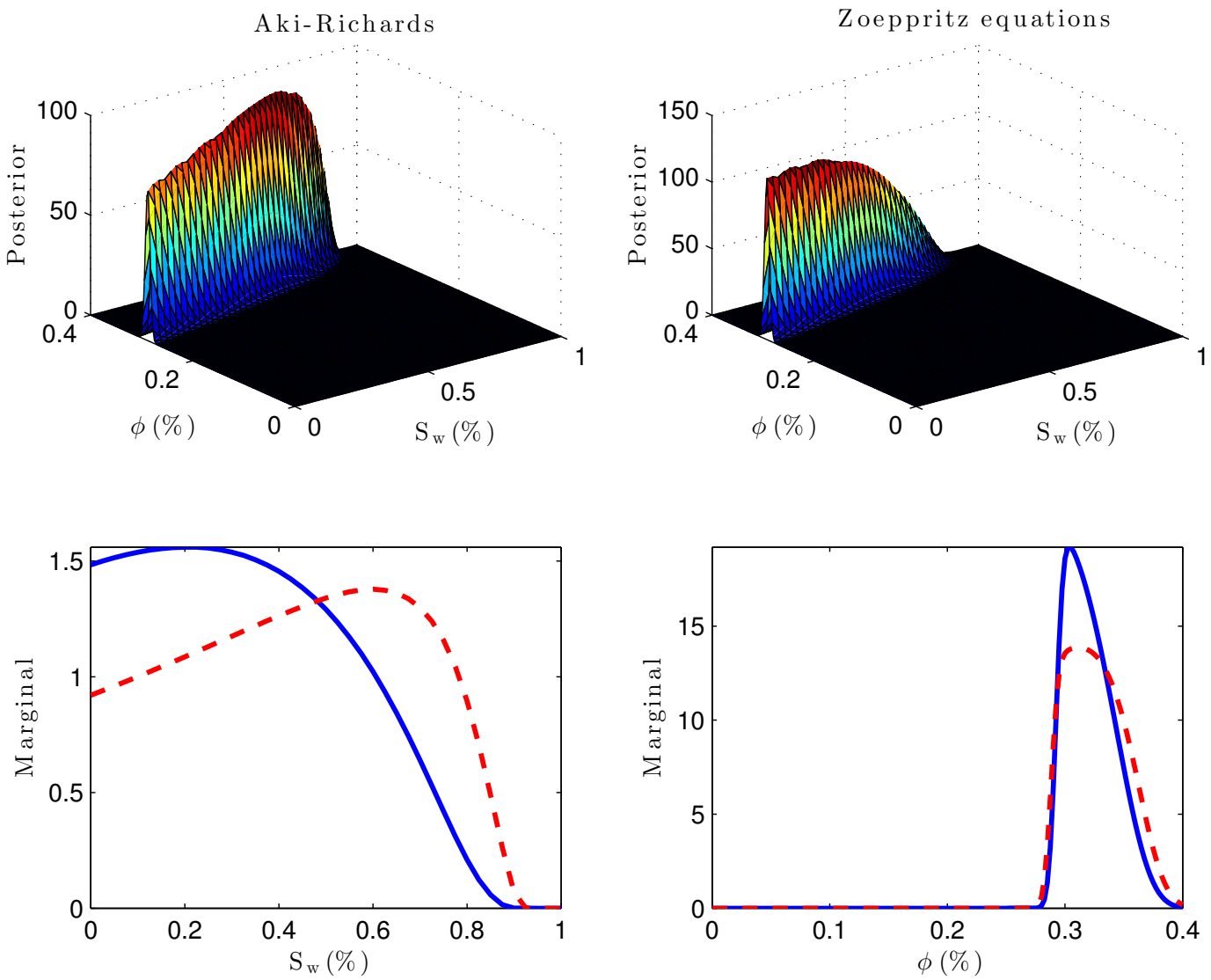

Figure 5.5: A gas and water saturated reservoir ($S_w = 10\%, \phi = 30\%$). The posterior distribution for Aki-Richards approximation (top left) and the Zoeppritz equations (top right). The corresponding marginal distributions for water saturation (bottom left) and porosity (bottom right). The dashed lines are for Aki-Richards approximation and the full line is for the Zoeppritz equations.

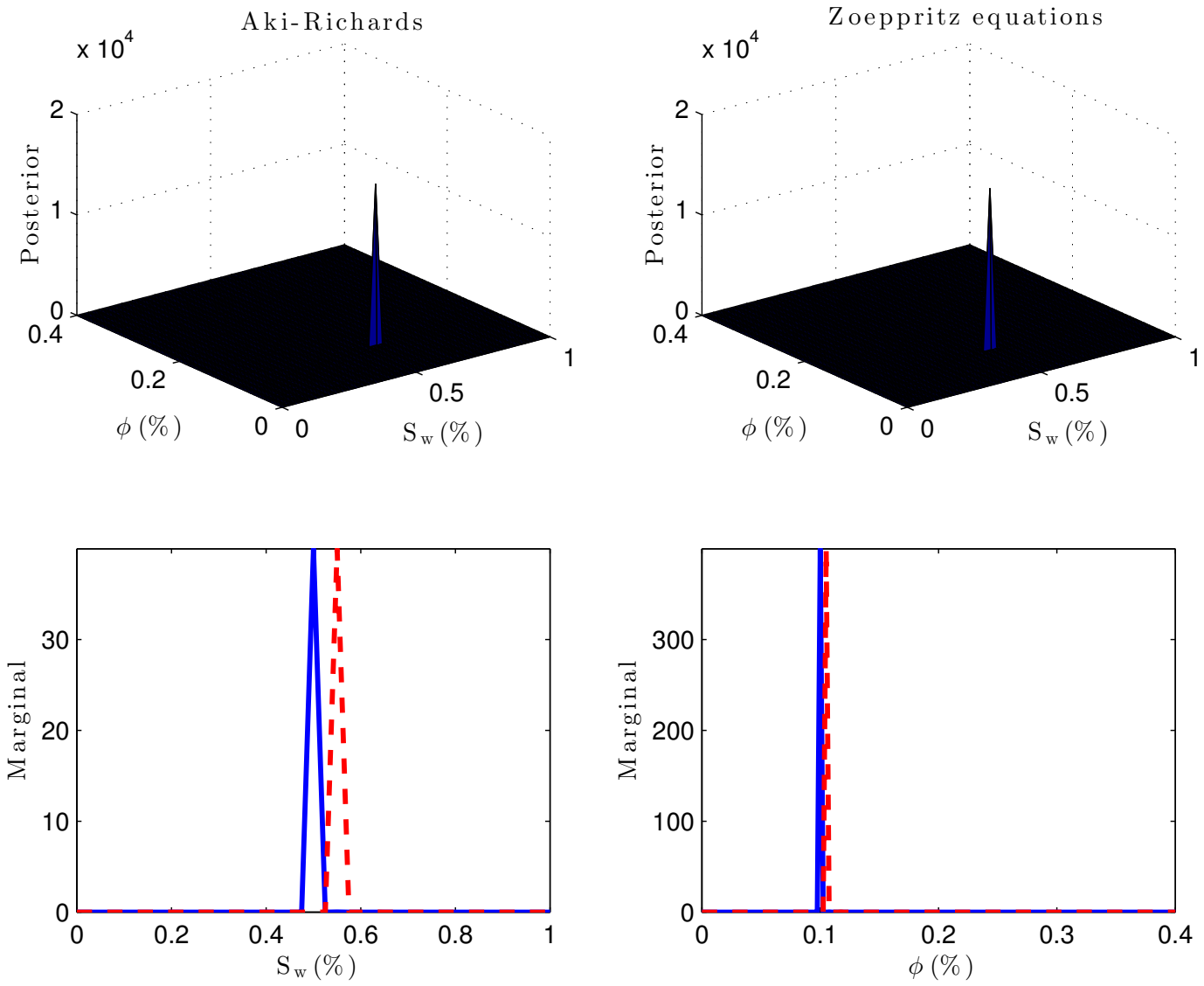

Figure 5.6: An oil and water saturated reservoir ($S_w = 50\%, \phi = 10\%$). The posterior distribution for Aki-Richards approximation (top left) and the Zoeppritz equations (top right). The corresponding marginal distributions for water saturation (bottom left) and porosity (bottom right). The dashed lines are for Aki-Richards approximation and the full line is for the Zoeppritz equations.

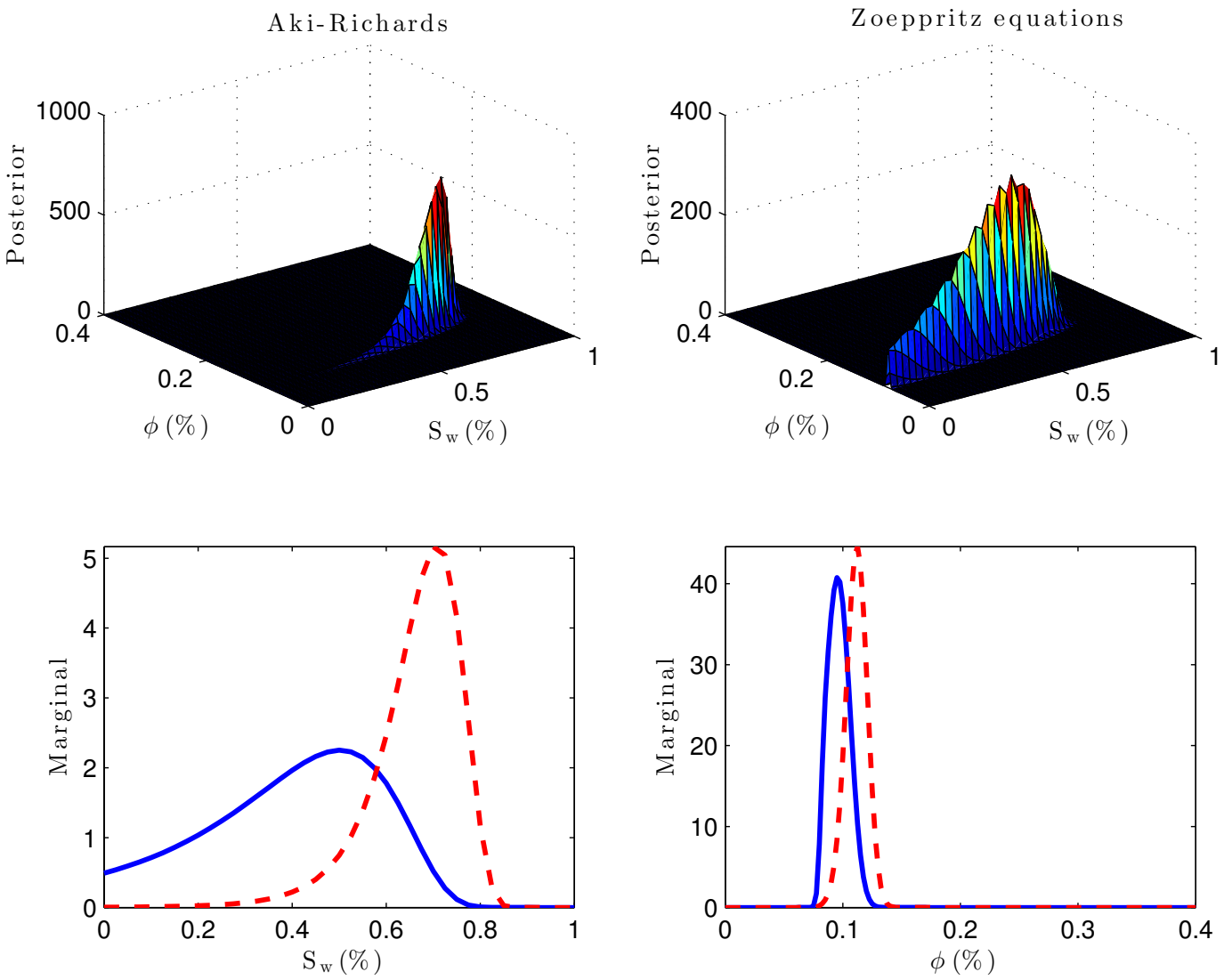

Figure 5.7: A gas and water saturated reservoir ($S_w = 50\%, \phi = 10\%$). The posterior distribution for Aki-Richards approximation (top left) and the Zoeppritz equations (top right). The corresponding marginal distributions for water saturation (bottom left) and porosity (bottom right). The dashed lines are for Aki-Richards approximation and the full line is for the Zoeppritz equations.

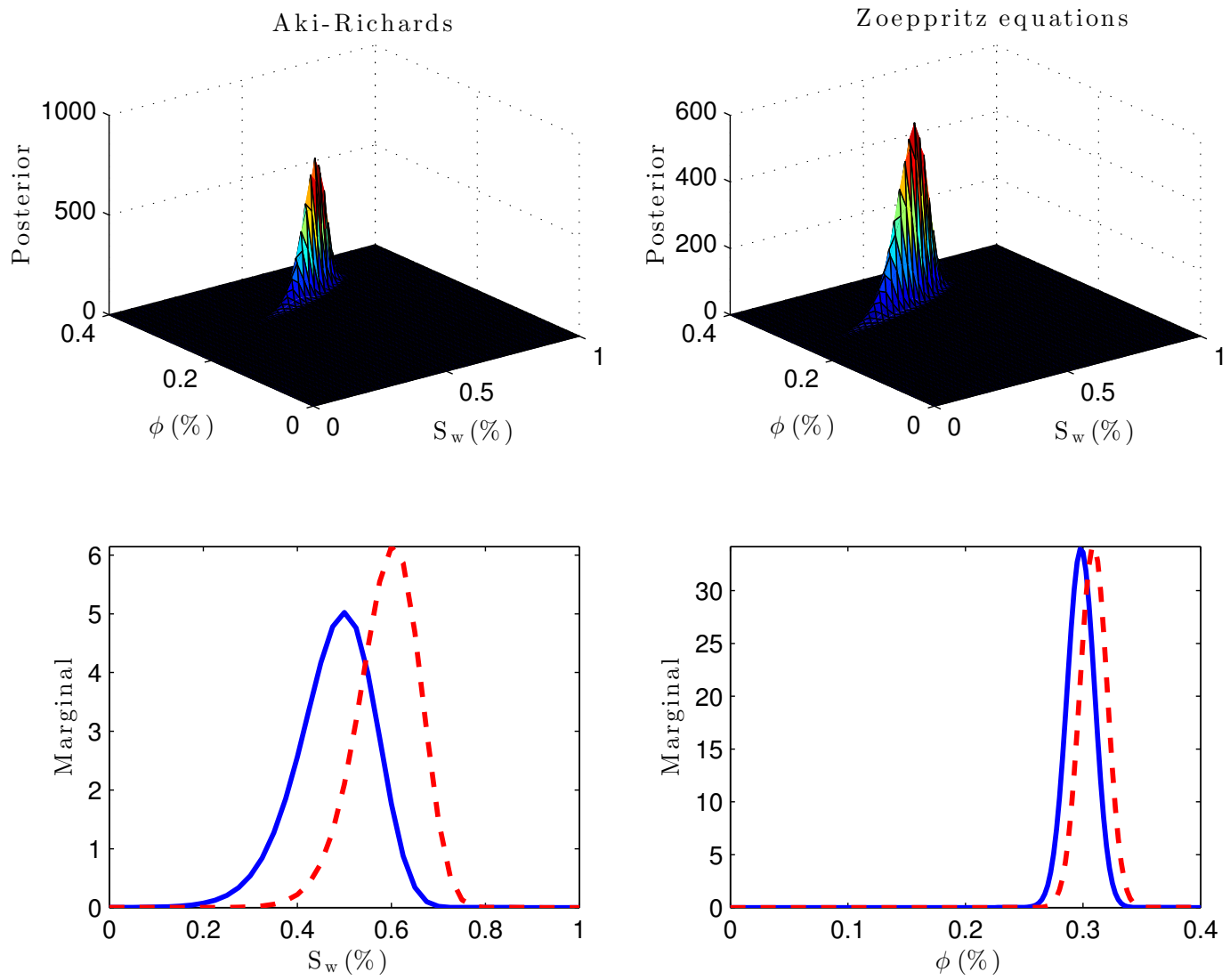

Figure 5.8: An oil and water saturated reservoir ($S_w = 50\%, \phi = 30\%$). The posterior distribution for Aki-Richards approximation (top left) and the Zoeppritz equations (top right). The corresponding marginal distributions for water saturation (bottom left) and porosity (bottom right). The dashed lines are for Aki-Richards approximation and the full line is for the Zoeppritz equations.

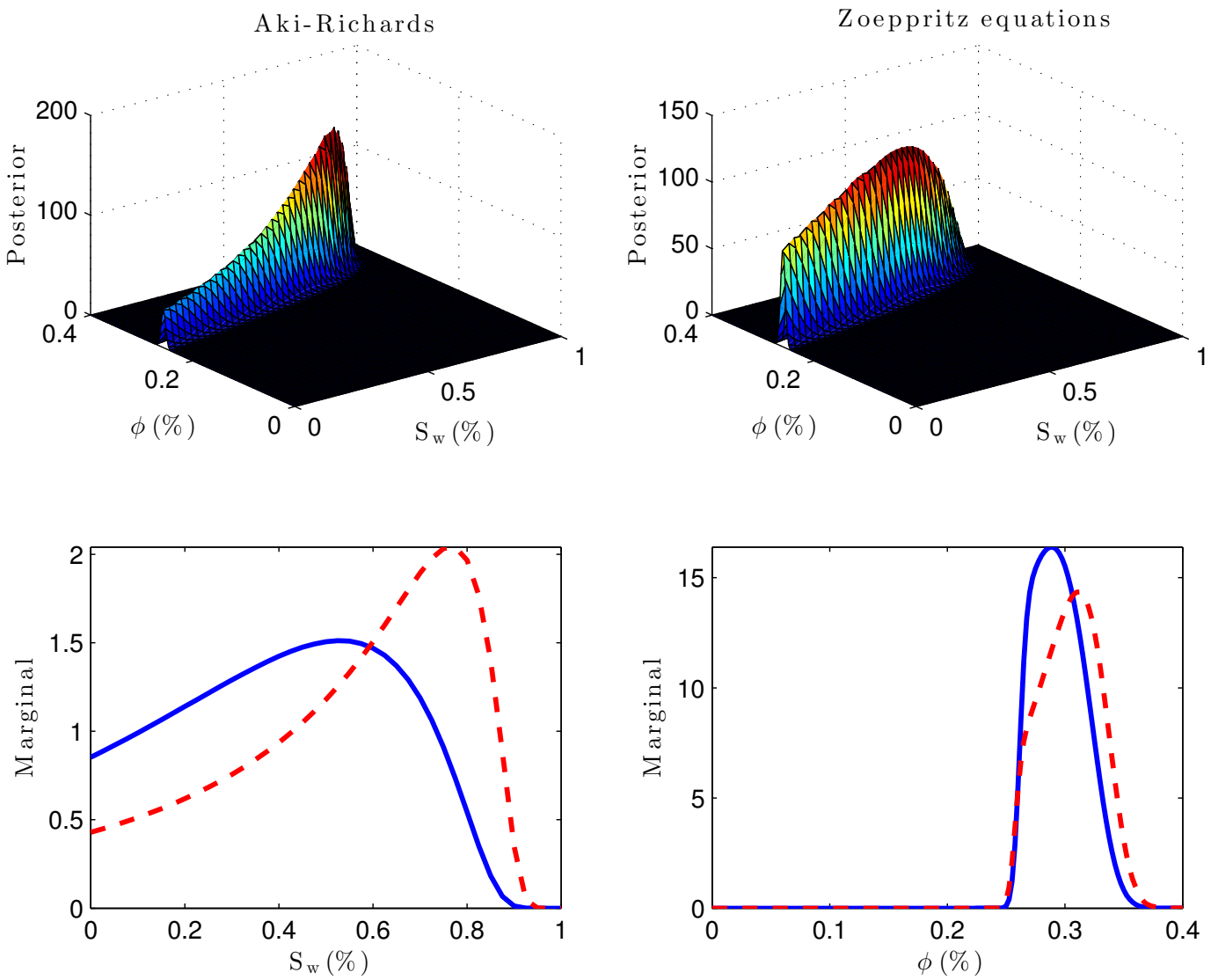

Figure 5.9: A gas and water saturated reservoir ($S_w = 50\%, \phi = 30\%$). The posterior distribution for Aki-Richards approximation (top left) and the Zoeppritz equations (top right). The corresponding marginal distributions for water saturation (bottom left) and porosity (bottom right). The dashed lines are for Aki-Richards approximation and the full line is for the Zoeppritz equations.

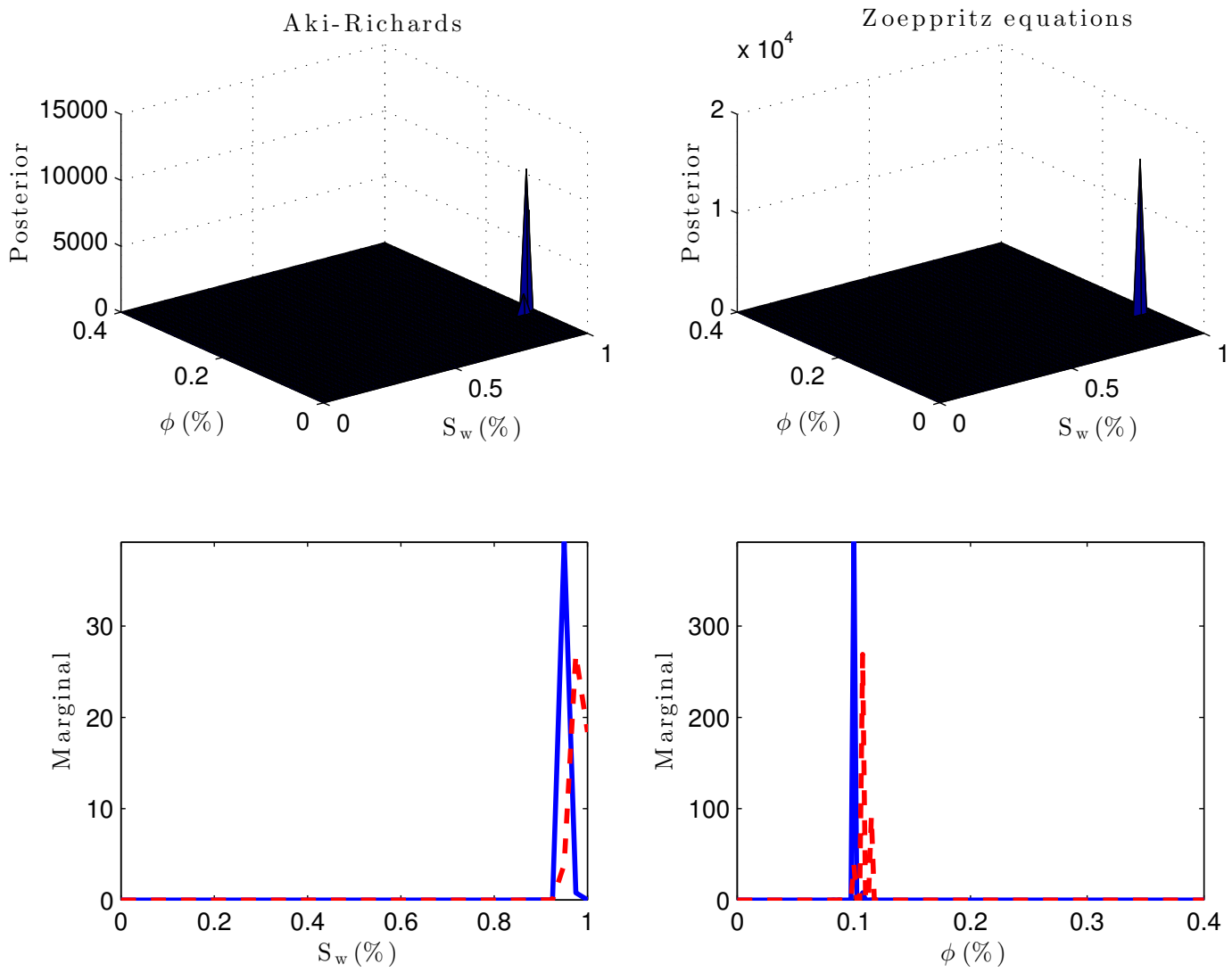

Figure 5.10: An oil and water saturated reservoir ($S_w = 95\%, \phi = 10\%$). The posterior distribution for Aki-Richards approximation (top left) and the Zoeppritz equations (top right). The corresponding marginal distributions for water saturation (bottom left) and porosity (bottom right). The dashed lines are for Aki-Richards approximation and the full line is for the Zoeppritz equations.

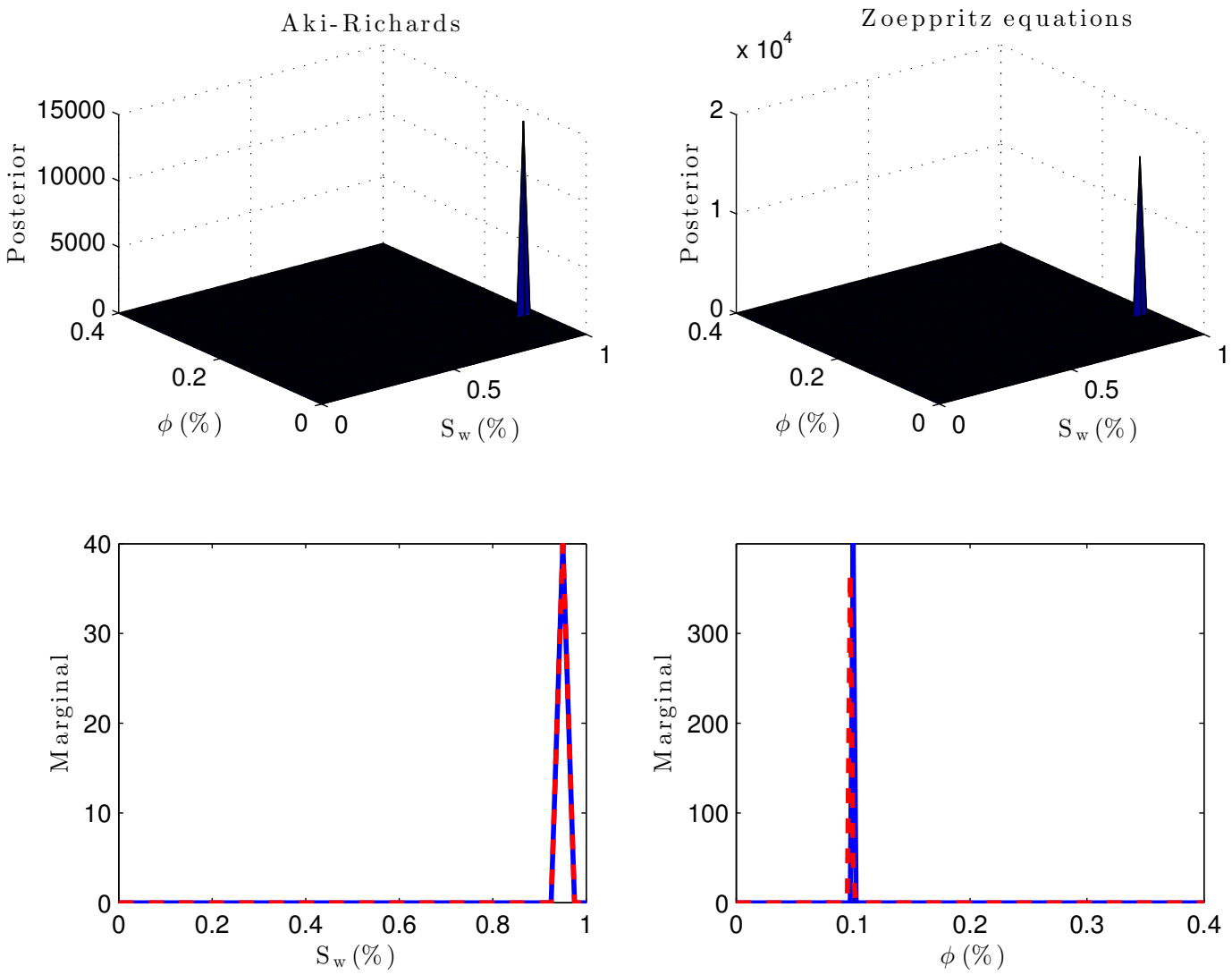

Figure 5.11: A gas and water saturated reservoir ($S_w = 95\%, \phi = 10\%$). The posterior distribution for Aki-Richards approximation (top left) and the Zoeppritz equations (top right). The corresponding marginal distributions for water saturation (bottom left) and porosity (bottom right). The dashed lines are for Aki-Richards approximation and the full line is for the Zoeppritz equations.

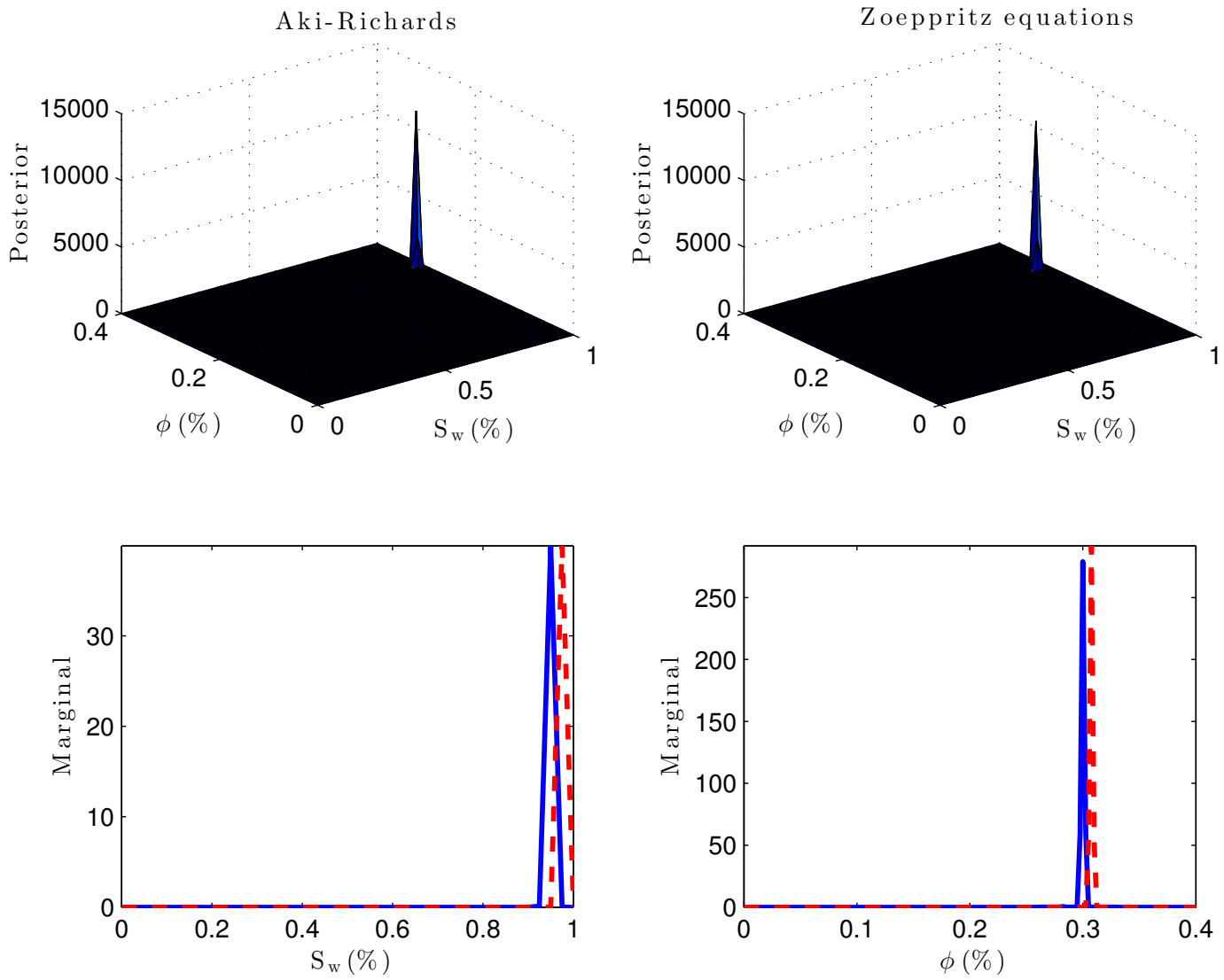

Figure 5.12: An oil and water saturated reservoir ($S_w = 95\%, \phi = 30\%$). The posterior distribution for Aki-Richards approximation (top left) and the Zoeppritz equations (top right). The corresponding marginal distributions for water saturation (bottom left) and porosity (bottom right). The dashed lines are for Aki-Richards approximation and the full line is for the Zoeppritz equations.

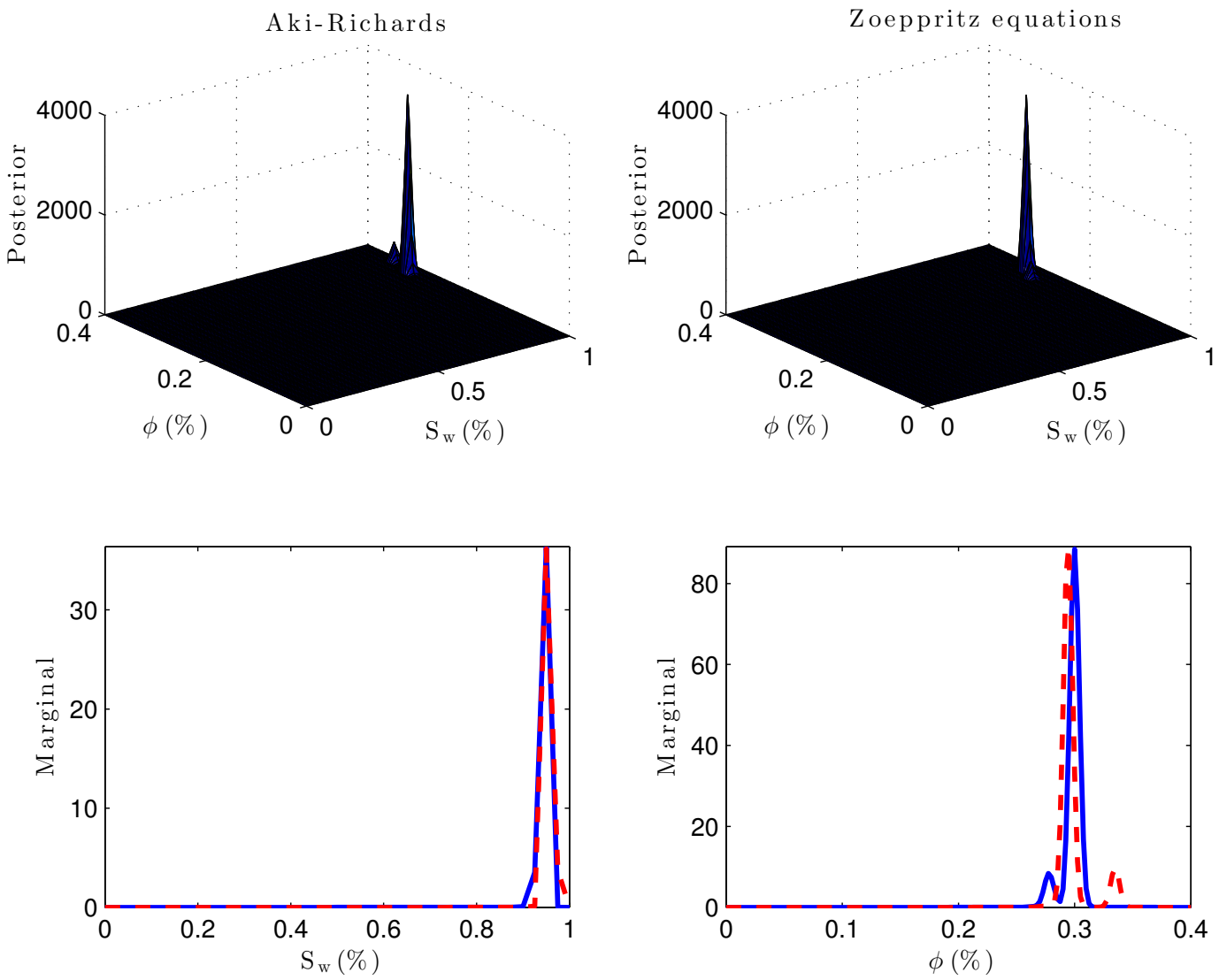

Figure 5.13: A gas and water saturated reservoir ($S_w = 95\%, \phi = 30\%$). The posterior distribution for Aki-Richards approximation (top left) and the Zoeppritz equations (top right). The corresponding marginal distributions for water saturation (bottom left) and porosity (bottom right). The dashed lines are for Aki-Richards approximation and the full line is for the Zoeppritz equations.

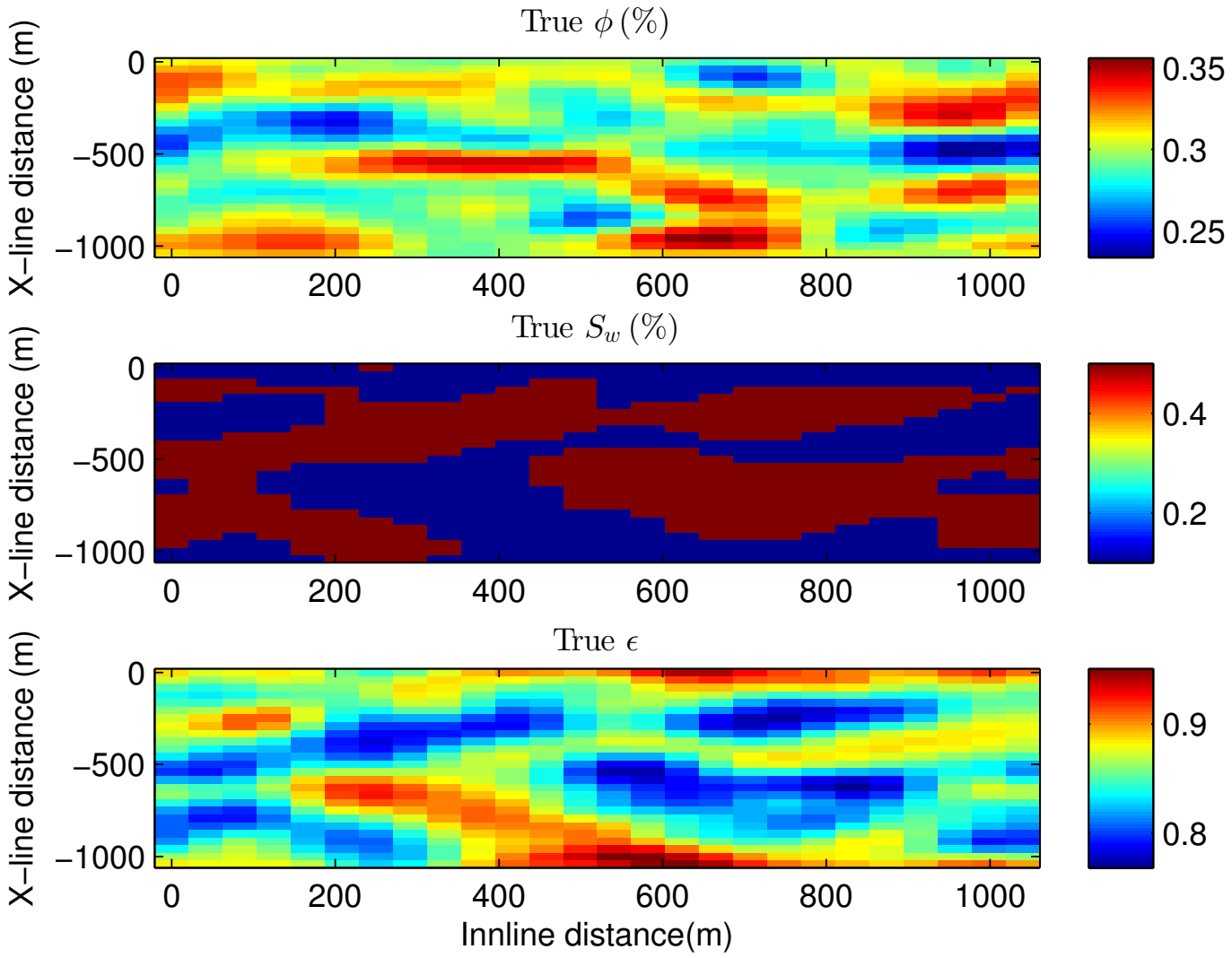

Figure 5.14: The true spatial distribution of the reservoir parameters for an oil and water saturated reservoir. Porosity (top), water saturation (centre) and the crack density (bottom).

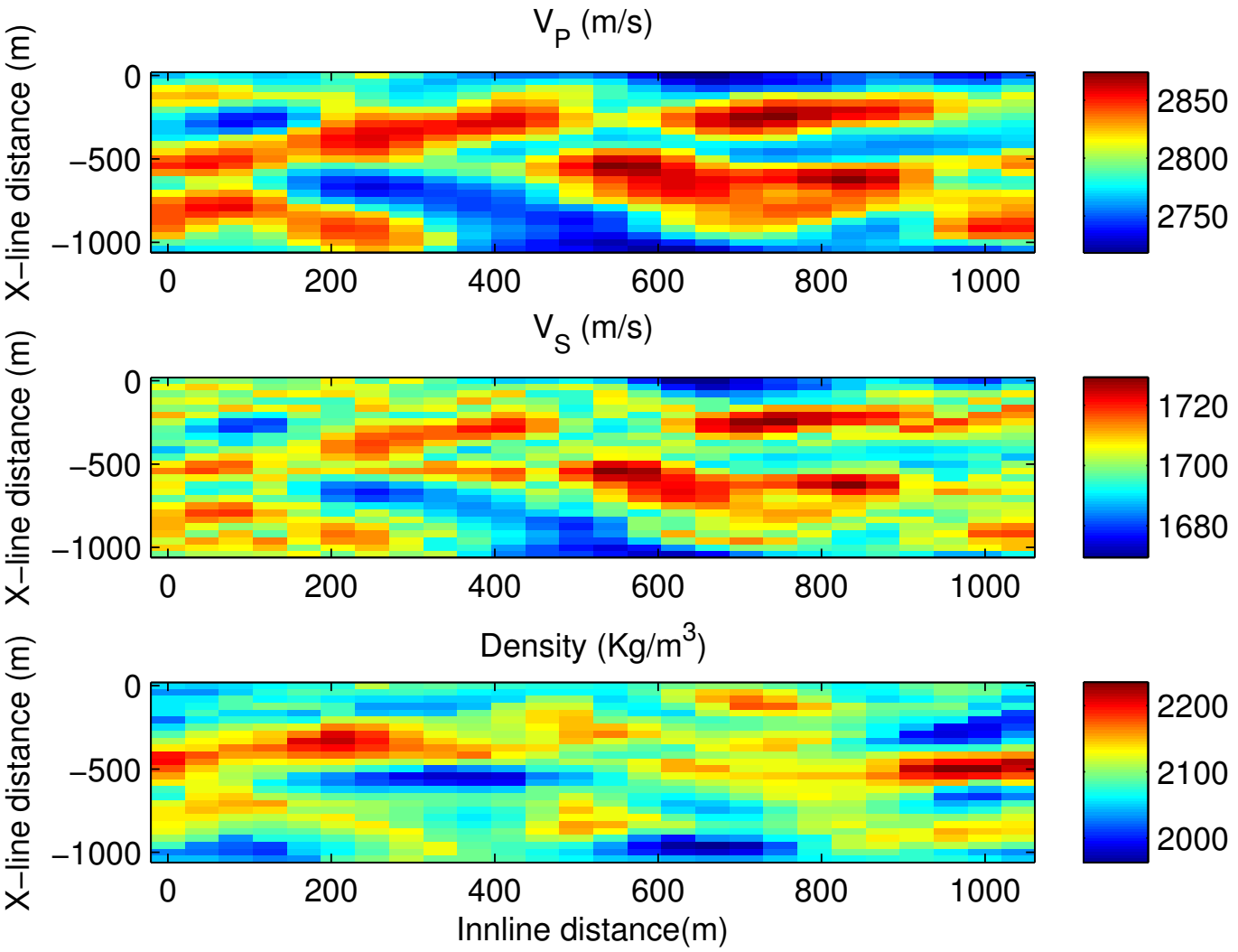

Figure 5.15: The effective elastic reservoir parameters. P-wave velocity (top), S-wave velocity (centre) and density (bottom).

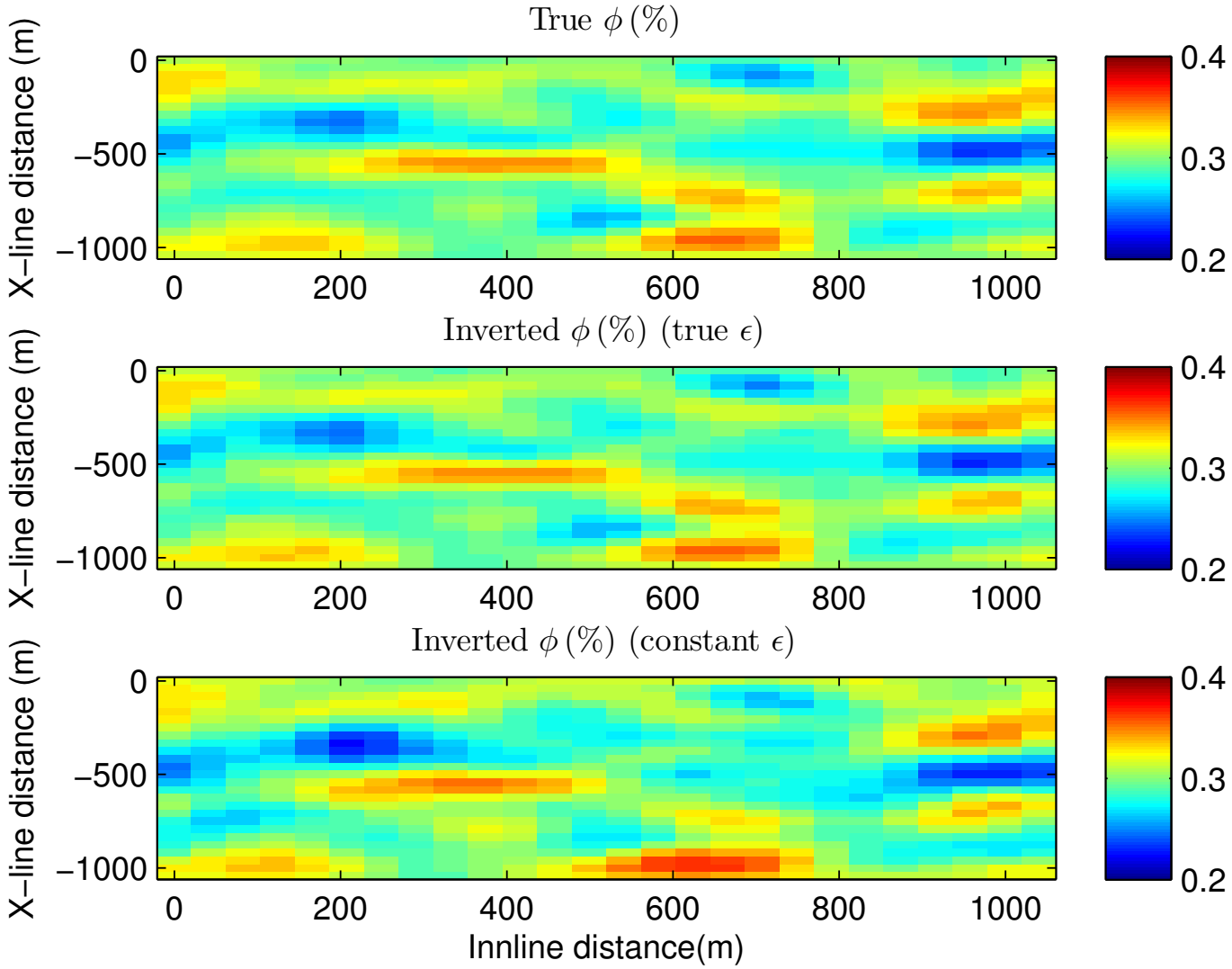

Figure 5.16: The map solutions for porosity from PP-reflection coefficient AVA data with 5% data uncertainty using the Zoeppritz equations for forward AVA modelling. True porosity (top), the inverted porosity using the true crack density (centre) and the inverted porosity using a constant crack density (bottom).

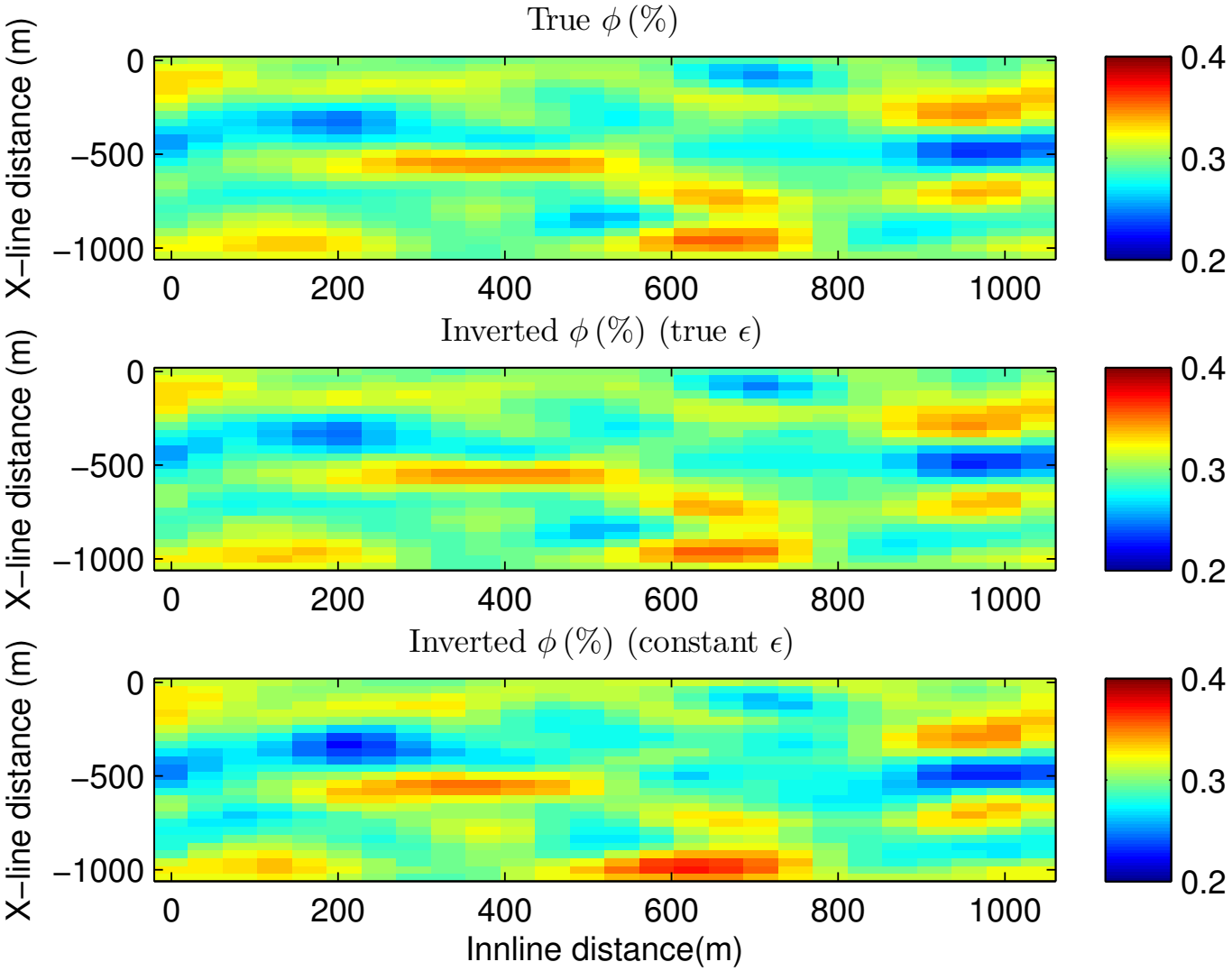

Figure 5.17: The map solutions for porosity from PP-reflection coefficient AVA data with 5% data uncertainty using Aki-Richards approximation for forward AVA modelling. True porosity (top), the inverted porosity using the true crack density (centre) and the inverted porosity using a constant crack density (bottom).

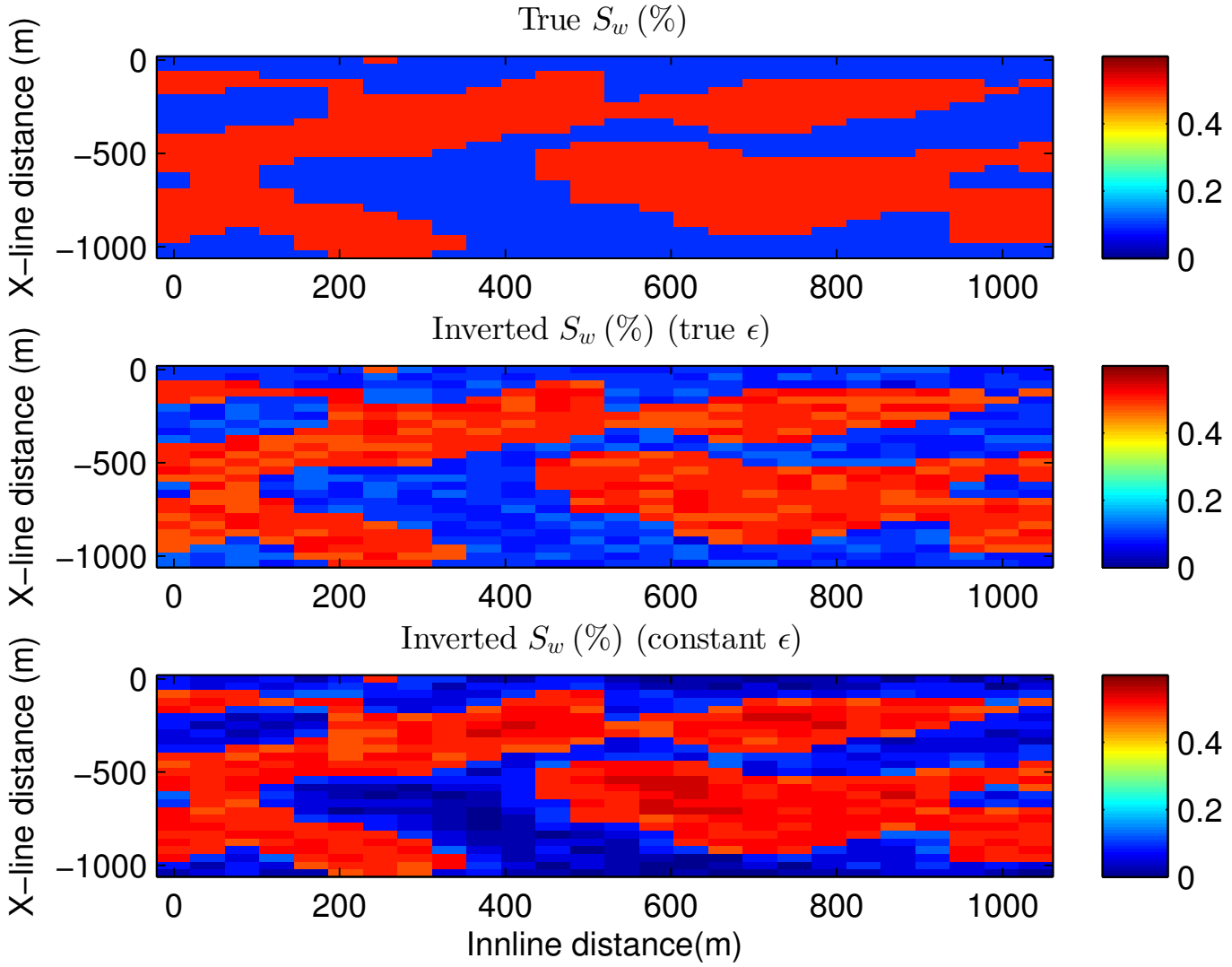

Figure 5.18: The map solutions for water saturation from PP-reflection coefficient AVA data with 5% data uncertainty using the Zoeppritz equations for forward modelling. True water saturation (top), the inverted water saturation using the true crack density (centre) and the inverted water saturation using a constant crack density (bottom).

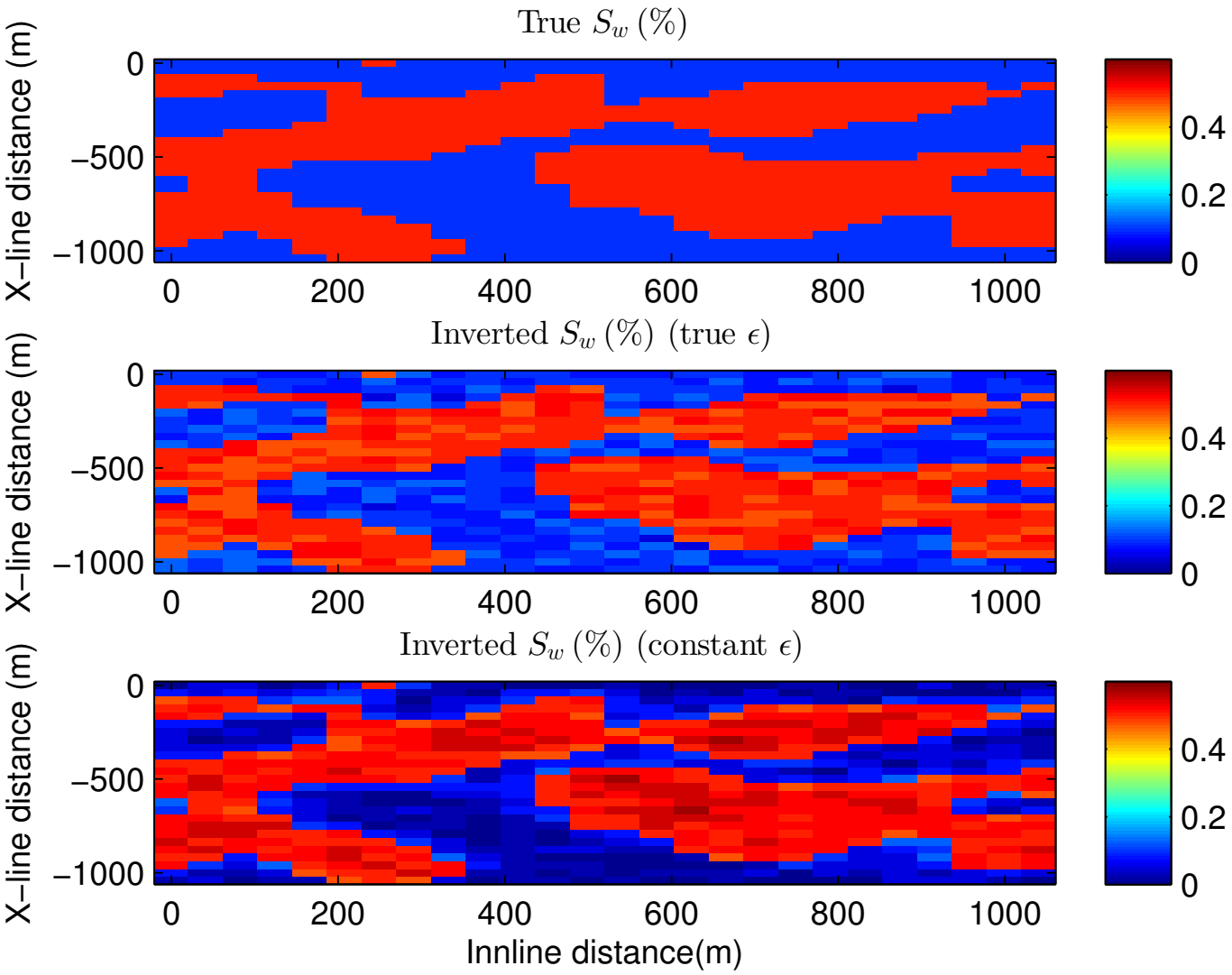

Figure 5.19: The map solutions for water saturation from PP-reflection coefficient AVA data with 5% data uncertainty using Aki-Richards approximation for forward modelling. True water saturation (top), the inverted water saturation using the true crack density (centre) and the inverted water saturation using a constant crack density (bottom).

Chapter 6

Two-step inversion methods

6.1 Introduction

In the following chapter, the aim is to perform two-step inversion procedures from AVA data modelled from a stratified elastic earth model with a reservoir section. The first inversion step is from AVA data to effective elastic reservoir parameters and the second inversion step is from effective elastic reservoir parameters to reservoir parameters, such as water saturation and porosity, using a rock physics model. The first step will follow a linearized inversion procedure based upon the algorithm presented by Buland and Omre (2003). An aim is to extend this algorithm by doing a rock physics inversion for an interface in the reservoir section in the inverted elastic earth model. Originally, the first inversion step was formulated in a Bayesian setting. This complicates the process of putting constraints on the temporal variability of the elastic earth models. The desired model properties are controlled by specification of the a priori model statistics. However, the length scale of the velocity and density variation is to a large extent unknown. This implies that our a priori knowledge of the earth's interior is rather poor (Scales and Sneider, 1997). A second aim will therefore be to reformulate the linearized inversion algorithm within the framework of a classical interpretation of statistics.

There are several aspects that advocate a two-step procedure rather than a one-step inversion procedure (Avseth et al., 2005). Linearized estimates are less computationally expensive than nonlinear estimates. Further, the effective elastic properties are very useful for many processing sequences of seismic data. In addition, it allows us verify the inversion results with other sources of information such as well logs and production data.

Lörtzer and Berkhout (1992) formulated a linearized inversion algorithm for relative contrasts in elastic properties for several interfaces in a time-window. This method was later extended to incorporate a time-continuous formulation of Aki-Richards approximation and a source wavelet (Buland and Omre, 2003; Stolt and Weglein, 1985). A major advantage of this formulation was that the time-continuous formulation of Aki-Richards approximation is a linear combination of the elastic parameters. Also, it

made it possible to put constraints on the temporal variation of the elastic parameters.

6.2 Forward modelling

6.2.1 The time-continuous reflectivity function

A depth dependent elastic earth model can be regarded as an ensemble of a large number of layers. Lörtzer and Berkhout (1992) formulated a linearized inversion algorithm from one-dimensional reflectivity function to relative contrasts in elastic properties for several interfaces in a time-window. The thickness of each layer should reflect the spatial variability such that the elastic parameters can be considered constant within each layer, and they should exhibit only small changes from one layer to the next. This method was later extended to incorporate a time-continuous formulation of Aki-Richards approximation and a source wavelet (Buland and Omre, 2003; Stolt and Weglein, 1985). A major advantage of this formulation was that the time-continuous formulation of Aki-Richards approximation is a linear combination of the elastic parameters. Also, it made it possible to put constraints on the temporal variation of the elastic parameters. This is done by assuming that a set of time dependent model parameters are logarithmic such that:

$$\mathbf{m}\left(\mathrm{t}\right) = \left[\ln \mathrm{V_P}\left(\mathrm{t}\right), \ln \mathrm{V_S}\left(\mathrm{t}\right), \ln \rho\left(\mathrm{t}\right)\right]^{\mathrm{T}} \tag{6.1}$$

The time-continuous PP-reflectivity function is then given as:

$$\begin{aligned} \mathrm{r_{PP}}\left(\mathrm{t},\theta\right) = & \frac{1}{2}\left(1+\tan^2\left(\mathrm{t},\theta\right)\right)\frac{\partial}{\partial \mathrm{t}}\ln \mathrm{V_P}\left(\mathrm{t}\right) - 4\left(\frac{\bar{\mathrm{V}}_{\mathrm{S}}^2\left(\mathrm{t}\right)}{\bar{\mathrm{V}}_{\mathrm{P}}^2\left(\mathrm{t}\right)}\sin^2\left(\mathrm{t},\theta\right)\right)\ln \mathrm{V_S}\left(\mathrm{t}\right) \\ & + \frac{1}{2}\left(1 - 4\frac{\bar{\mathrm{V}}_{\mathrm{S}}^2\left(\mathrm{t}\right)}{\bar{\mathrm{V}}_{\mathrm{P}}^2\left(\mathrm{t}\right)}\sin^2\left(\mathrm{t},\theta\right)\right)\frac{\partial}{\partial \mathrm{t}}\ln \rho\left(\mathrm{t}\right) \end{aligned} \tag{6.2}$$

Similar expressions are also straightforward for the converted reflectivity.

Buland and Omre (2003) implemented a matrix formulation of the time-continuous formulation of Aki-Richards approximation. Each of the model parameters (6.1) need to be discritized into NT time samples, and the dimension of the resulting column vector, $\mathbf{m}$, would be $(3 \times \mathrm{NT}) \times 1$:

$$\mathbf{m} = \left[\ln \mathrm{V_{P_1}} \cdots \ln \mathrm{V_{P_{NT}}}, \ln \mathrm{V_{S_1}} \cdots \ln \mathrm{V_{S_{NT}}}, \ln \rho_1 \cdots \ln \rho_{\mathrm{NT}}\right]^{\mathrm{T}} \tag{6.3}$$

If the values of a function are only given at a number of discrete points then the derivative can be computed numerically with the aid of finite-difference, discrete Taylor approximations. A simple choice is the forward finite-difference approximation to the first order derivative with a first-order accuracy.

The 1D derivative of a function, f, given at equidistant points is thus for a single point, x_i:

$$f'_i \approx \frac{(f_{i+1} - f_i)}{(x_{i+1} - x_i)} \tag{6.4}$$

It is possible to represent the derivative by an operator, $\mathbf{D}_{FD}$, a matrix that contains the coefficients in the finite-difference approximation to a derivative:

$$\mathbf{D}_{FD} = \begin{bmatrix} -1 & 1 & \cdots & 0 \\ 0 & \ddots & \ddots & 0 \\ 0 & \cdots & -1 & -1 \end{bmatrix} \tag{6.5}$$

A finite-difference operator with dimension $(NM = NT - 1) \times NT$, may be defined for each of the model parameters in (6.3). They can in turn be combined into a block-diagonal matrix with dimension $(3 \times NM) \times (3 \times NT)$:

$$\mathbf{D} = \begin{bmatrix} \mathbf{D}_{FD} & 0 & 0 \\ 0 & \mathbf{D}_{FD} & 0 \\ 0 & 0 & \mathbf{D}_{FD} \end{bmatrix} \tag{6.6}$$

The differentiated earth model represents a time-continuous model of fractional changes in elastic properties, $\mathbf{c}$:

$$\mathbf{c} = \begin{bmatrix} \mathbf{c}_{V_P} \\ \mathbf{c}_{V_S} \\ \mathbf{c}_{\rho} \end{bmatrix} = \begin{bmatrix} \mathbf{D}_{FD} & 0 & 0 \\ 0 & \mathbf{D}_{FD} & 0 \\ 0 & 0 & \mathbf{D}_{FD} \end{bmatrix} \begin{bmatrix} \ln \mathbf{V}_P \\ \ln \mathbf{V}_s \\ \ln \boldsymbol{\rho} \end{bmatrix} \tag{6.7}$$

Three coefficients may defined from the time-continuous P-to-P reflectivity function (6.2) for a discrete angle, na, and a time sample, nt:

$$a_{na,nt} = \frac{1}{2}\left(1 + \tan^2\theta_{na}\right)_{nt} \qquad b_{na,nt} = -4\left(\frac{\bar{V}_S^2}{\bar{V}_P^2}\sin^2\theta_{na}\right)_{nt} \qquad c_{na,nt} = \frac{1}{2}\left(1 - 4\frac{\bar{V}_S^2}{\bar{V}_P^2}\sin^2\theta_{na}\right)_{nt} \tag{6.8}$$

A set of diagonal matrices, $\mathbf{A}_{V_P}(\theta_{na})$, $\mathbf{A}_{V_S}(\theta_{na})$ and $\mathbf{A}_{\rho}(\theta_{na})$ containing discrete time samples for a fixed angle, are created for each of the three coefficients. Assuming there is NT discrete time samples

in (6.3), the dimension of each of the diagonal matrices is NT × NM:

$$\mathbf{A}_{\mathrm{V_P}}(\theta_{\mathrm{na}}) = \begin{bmatrix} \frac{1}{2}\left(1+\tan^2\theta_{\mathrm{na}}\right)_1 & \cdots & 0 \\ \vdots & \ddots & \vdots \\ 0 & \cdots & \frac{1}{2}\left(1+\tan^2\theta_{\mathrm{na}}\right)_{\mathrm{NM}} \end{bmatrix} \tag{6.9}$$

$$\mathbf{A}_{\mathrm{V_S}}(\theta_{\mathrm{na}}) = \begin{bmatrix} -4\left(\frac{\bar{\mathrm{V}}_{\mathrm{S}}^2}{\bar{\mathrm{V}}_{\mathrm{P}}^2}\sin^2\theta_{\mathrm{na}}\right)_1 & \cdots & 0 \\ \vdots & \ddots & \vdots \\ 0 & \cdots & -4\left(\frac{\bar{\mathrm{V}}_{\mathrm{S}}^2}{\bar{\mathrm{V}}_{\mathrm{P}}^2}\sin^2\theta_{\mathrm{na}}\right)_{\mathrm{NM}} \end{bmatrix} \tag{6.10}$$

$$\mathbf{A}_{\rho}(\theta_{\mathrm{na}}) = \begin{bmatrix} \frac{1}{2}\left(1-4\frac{\bar{\mathrm{V}}_{\mathrm{S}}^2}{\bar{\mathrm{V}}_{\mathrm{P}}^2}\sin^2\theta_{\mathrm{na}}\right)_1 & \cdots & 0 \\ \vdots & \ddots & \vdots \\ 0 & \cdots & \frac{1}{2}\left(1-4\frac{\bar{\mathrm{V}}_{\mathrm{S}}^2}{\bar{\mathrm{V}}_{\mathrm{P}}^2}\sin^2\theta_{\mathrm{na}}\right)_{\mathrm{NM}} \end{bmatrix} \tag{6.11}$$

They are in turn used to define a block-matrix, $\mathbf{A}$, that is built from such time dependent diagonal matrices for each of the discrete angles:

$$\mathbf{A} = \begin{bmatrix} \mathbf{A}_{\mathrm{V_P}}(\theta_1) & \mathbf{A}_{\mathrm{V_S}}(\theta_1) & \mathbf{A}_{\rho}(\theta_1) \\ \vdots & \vdots & \vdots \\ \mathbf{A}_{\mathrm{V_P}}(\theta_{\mathrm{NA}}) & \mathbf{A}_{\mathrm{V_S}}(\theta_{\mathrm{NA}}) & \mathbf{A}_{\rho}(\theta_{\mathrm{NA}}) \end{bmatrix} \tag{6.12}$$

The dimension of the block-matrix (6.12) in the case of NA discrete angles is then (NT × NA) × (3 × NM). The time-continuous PP-reflectivity function (6.2) can thus be given as a product between the block-matrix and the derivative of the model vector (6.7):

$$\mathbf{r}_{\mathrm{PP}} = \begin{bmatrix} \mathbf{r}_{\mathrm{PP}}(\theta_1) \\ \vdots \\ \mathbf{r}_{\mathrm{PP}}(\theta_{\mathrm{NA}}) \end{bmatrix} \begin{bmatrix} \mathbf{A}_{\mathrm{V_P}}(\theta_1) & \mathbf{A}_{\mathrm{V_S}}(\theta_1) & \mathbf{A}_{\rho}(\theta_1) \\ \vdots & \vdots & \vdots \\ \mathbf{A}_{\mathrm{V_P}}(\theta_{\mathrm{NA}}) & \mathbf{A}_{\mathrm{V_S}}(\theta_{\mathrm{NA}}) & \mathbf{A}_{\rho}(\theta_{\mathrm{NA}}) \end{bmatrix} \begin{bmatrix} \mathbf{c}_{\mathrm{V_P}} \\ \mathbf{c}_{\mathrm{V_S}} \\ \mathbf{c}_{\rho} \end{bmatrix} \tag{6.13}$$

The dimension of the resulting PP-reflectivity vector is (NT × NA) × 1.

6.2.2 Seismic waveform modelling by the convolutional model

The characteristic pressure wave created by an impulsive source is called the signature of the source, and it can be described as band-limited wavelets of finite duration. As the wavelet propagates through the subsurface its overall amplitude decays because of waveform dispersion and the frequency content changes due to absorption. A basic assumption in the convolutional model is that the source waveform is stationary, it does not change as it travels through the subsurface (Yilmaz, 2001). The reflectivity can then be regarded as a filter that acts on the source wavelet as it propagates through the subsurface. A spike as a source wavelet would give back the impulse response of the filter, which in this case would

be the reflectivity series. It is necessary to sample the functions associated with the source wavelet,$\mathbf{w}$, and reflectivity, $\mathbf{r}_{\mathrm{PP}}$, at regular intervals. Suppose that the length of the discrete time series is NT for the reflectivity and NW for the source wavelet. A linear convolution of them in the time domain would give a new time series associated with a recorded seismic trace, $\mathbf{s}$, that has $\mathrm{N} = (\mathrm{NW} + \mathrm{NT}) - 1$ samples (Mæland, 2005). The elements in the vector, $\mathbf{s}$**,** are given by:

$$\mathrm{s_n} = \sum_{\mathrm{k}=0}^{\mathrm{n}} \mathrm{r_k w_{n-k}} \tag{6.14}$$

for $\mathrm{n} = 0, \ldots, (\mathrm{N} - 1)$. The linear convolutional matrix for a single incident angle, $\mathbf{w}_{\theta_{\mathrm{na}}}$, is thus:

$$\mathbf{w}_{\theta_{\mathrm{na}}} = \begin{bmatrix} \mathrm{w}_1(\theta_{\mathrm{na}}) & 0 & & \cdots & & 0 \\ \mathrm{w}_2(\theta_{\mathrm{na}}) & \mathrm{w}_1(\theta_{\mathrm{na}}) & 0 & \cdots & & 0 \\ \vdots & \ddots & \ddots & \ddots & \cdots & 0 \\ \mathrm{w}_{\mathrm{NW}}(\theta_{\mathrm{na}}) & \cdots & \cdots & \mathrm{w}_1(\theta_{\mathrm{na}}) & \cdots & 0 \\ 0 & \ddots & \cdots & \cdots & \ddots & 0 \\ \vdots & \ddots & \mathrm{w}_{\mathrm{NW}}(\theta_{\mathrm{na}}) & \cdots & \cdots & \mathrm{w}_1(\theta_{\mathrm{na}}) \\ & & 0 & \ddots & \cdots & \vdots \\ & & \vdots & \ddots & \ddots & \vdots \\ 0 & & 0 & \cdots & 0 & \mathrm{w}_{\mathrm{NW}}(\theta_{\mathrm{na}}) \end{bmatrix} \tag{6.15}$$

It has dimensions $\mathrm{N} \times \mathrm{NT}$. A block-diagonal wavelet matrix, $\mathbf{W}$, that contains one linear convolution matrix for each angle, can be defined from this:

$$\mathbf{W} = \begin{bmatrix} \mathbf{w}_{\theta_1} & \cdots & \mathbf{0} \\ \vdots & \ddots & \vdots \\ \mathbf{0} & \cdots & \mathbf{w}_{\theta_{\mathrm{NA}}} \end{bmatrix} \tag{6.16}$$

It has dimensions $(\mathrm{NA} \times \mathrm{N}) \times (\mathrm{NA} \times \mathrm{NT})$. The convolution is performed by multiplying the PP-reflectivity vector, $\mathbf{r}$, with the block-diagonal wavelet matrix, $\mathbf{W}$, and the resulting seismic data is thus given by (Buland and El Ouair, 2006):

$$\mathbf{d} = \begin{bmatrix} \mathbf{d}(\theta_1) \\ \vdots \\ \mathbf{d}(\theta_{\mathrm{NA}}) \end{bmatrix} = \begin{bmatrix} \mathbf{w}_{\theta_1} & \cdots & \mathbf{0} \\ \vdots & \ddots & \vdots \\ \mathbf{0} & \cdots & \mathbf{w}_{\theta_{\mathrm{NA}}} \end{bmatrix} \begin{bmatrix} \mathbf{r}_{\mathrm{PP}}(\theta_1) \\ \vdots \\ \mathbf{r}_{\mathrm{PP}}(\theta_{\mathrm{NA}}) \end{bmatrix} \tag{6.17}$$

The dimension of the data vector is $(\mathrm{NA} \times \mathrm{N}) \times 1$. Following the preceding derivation, the symbolic form for the seismic data can be expressed as:

$$\mathbf{d} = \mathbf{Wr} = \mathbf{WAc} = \mathbf{WADm} \tag{6.18}$$

6.2.3 Numerical implementation

In the forward modelling, the first step was to generate a set of synthetic well logs for the elastic earth properties. It would represent a layered earth model with an oil-water saturated reservoir section. Effective elastic reservoir properties were first defined using the procedure in section 2.3. The water saturation and porosity were set to $S_w = 95\%$ and $\phi = 30\%$ for the reservoir section. It corresponds to a AVA inversion test that was successful, case 6a, in section 5.2.2. Thus, the overburden was also chosen to give similar contrasts in elastic properties at the layer boundary in order to create an analogue. However, the elastic properties were set to have a slight linear increase in elastic properties through the overburden. In addition, a homogeneous top layer and an underburden were chosen such that there were four layers in total. Also, the thicknesses of the layers were set such that the total depth through the earth model was 1000 meters. The synthetic well logs are summarized in table 6.1.

The synthetic well logs represented an earth model in depth, but the model parameters in the waveform forward modelling were required to be a function of time. Hence, the earth model was discretized into partitions of $dz = 10$ meters. Further, a vector of cumulative travel times, $\mathbf{T}$, was calculated by integrating the travel time to each interface. A one-way travel time vector, $\mathbf{t}$, with a constant sampling interval of $dt = 2$ ms was defined within the range of the cumulative travel times. Following this, the earth model was transformed from $\mathbf{T}$ to $\mathbf{t}$ using a linear interpolation scheme. The elastic 1D model in time is shown for an earth model with an oil and water saturated reservoir section in figure 6.2.

The true earth model was first made logarithmic and put as a column vector, $\mathbf{m}_t$ (6.3). Following this, every second angle in an interval of incident angles, θ, from 0° to 40° were chosen for the forward modelling, and the coefficients in the block-matrix formulation of Aki-Richards approximation, $\mathbf{A}$ (6.12), were calculated from the true model. This concluded the calculation of the reflectivity series, $\mathbf{r}$, for the earth model.

A Ricker wavelet with a centre frequency, $f_0 = 30$Hz, was chosen as the source wavelet. They are zero-phase wavelets with a central peak and two smaller side lobes. The mathematical formula for a Ricker wavelet is given by (Ryan, 1994):

$$w(t) = \left(1 - 2\pi^2 f_0^2 t^2\right) \exp\left(-\pi^2 f_0^2 t^2\right) \tag{6.19}$$

This wavelet was discretized using a sampling interval of $dt = 2$ms, and then it was put on block-diagonal wavelet form, $\mathbf{W}$ (6.16). Thus, we were able to calculate the seismic data by waveform forward modelling as (6.18):

$$\mathbf{d} = \mathbf{Wr} = \mathbf{WAc} = \mathbf{WADm} \tag{6.20}$$

The forward model operator, that relates the model and the data, is as such $\mathbf{G} = \mathbf{WAD}$. A seismogram for the earth model with an oil and water saturated reservoir section is shown in figure 6.3, and the work flow in the forward modelling is summarized in figure 6.1.

6.3 Inversion tests

The seismic data that was modelled from the set of synthetic well logs was contaminated by various amounts of zero mean Gaussian noise. In particular, we defined the data errors as a percentage, p, of the maximum amplitude in the seismic data such that they were identically distributed:

$$\sigma_{\mathrm{d}}^2 = \left(\mathrm{p} \cdot \max |\mathbf{d}|\right)^2 \tag{6.21}$$

The data covariance matrix, $\mathbf{C}_{\mathrm{d}}$, was then simply the variance times the identity matrix. Three different percentages of the maximum amplitude, $\mathrm{p} = 10^{-5}, 10^{-4}$ and 10^{-3}, provided increasing noise levels that was used to test the robustness of the inversion. Ultimately, the aim was to recover the reservoir parameters that were used in the forward modelling for the reservoir section. The first step was linearized waveform inversion for the elastic earth model and the second step was rock physics inversion for saturation and porosity for a known overburden. This was tested for two different inversion algorithms within the frequentist or Bayesian framework of statistics.

6.3.1 A classical approach to a two-step inversion with a prior model

Very ill-conditioned problems may be made more stable by searching for solutions that are close to a prior model, $\mathbf{m}_0$. A common choice is to smooth well logs that define the prior model (Buland and Omre, 2003). The modified optimization problem for Tikhonov regularization with a prior is given by:

$$\mathrm{J}\left(\mathbf{m}\right) = \frac{1}{2}\left|\left|\mathbf{G}\mathbf{m} - \mathbf{d}_{\mathrm{obs}}\right|\right|_2^2 + \frac{\lambda_0^2}{2}\left|\left|\mathbf{m} - \mathbf{m}_0\right|\right|_2^2 + \frac{\lambda_1^2}{2}\left|\left|\mathbf{L}\mathbf{m}\right|\right|_2^2 \tag{6.22}$$

A solution to this optimization problem is given by:

$$\mathbf{m}_\lambda = \left(\mathbf{G}^{\mathrm{T}}\mathbf{G} + \lambda_0^2\mathbf{I} + \lambda_1^2\mathbf{L}^{\mathrm{T}}\mathbf{L}\right)^{-1}\left(\mathbf{G}^{\mathrm{T}}\mathbf{d}_{\mathrm{obs}} + \lambda_0^2\mathbf{I}\mathbf{m}_0\right) \tag{6.23}$$

It was necessary to define a prior model in accordance with the logarithmic model parameters, $\mathbf{m}$ (6.3). Synthetic well logs were in our case obtained by smoothing the true earth model in depth by fitting a 3rd degree polynomial. The conversion from depth in meters to depth in time was done as in section 6.2.3. Following this, the prior model was made logarithmic and put on vector form as in (6.3).

The relation between the true data and the observed data was given by:

$$\mathbf{d}_{\mathrm{obs}} = \mathbf{d}_{\mathrm{true}} + \mathbf{e}, \mathbf{e} \sim \mathrm{N}\left(\mathbf{0}, \mathbf{C}_{\mathrm{d}}\right) \tag{6.24}$$

The optimal regularization parameters were found by Morozovs discrepancy principle (4.9). It was implemented by an iterative empirical procedure where $\mathrm{S} = 0.8$ was a decay constant and the regular-

ization parameters would be exponentially reduced by each iteration, n:

$$\begin{aligned} \lambda_0 &= \mathrm{S}^{\mathrm{n}} \\ \lambda_1 &= 2\lambda_0 \end{aligned} \tag{6.25}$$

After each iteration, the norm of the data residuals was calculated by: $||\mathbf{G}\mathbf{m}_\lambda - \mathbf{d}_{\mathrm{obs}}||$. An optimal choice of regularization parameters was reached when the norm of the data residuals was less than or equal to the norm of the noise, $||\mathbf{e}||$. A threshold level for when to stop the iterations was therefore chosen as $\delta = ||\mathbf{e}||$. Thus, we could conclude the first inversion step to an elastic earth model using a classical Tikhonov inversion with prior for minimization.

Following this, the logarithm was removed from all the model parameters by multiplying each component by an exponential function. The inverted elastic earth model, $\mathbf{m}_\lambda$, from the first step was split into three parts corresponding to the elastic parameters. Time samples from the middle of the reservoir sections were subsequently chosen from each of them into a vector of observed elastic reservoir properties, $\mathbf{m}_{\mathrm{calc}}$. The reservoir model was further discretized into K grid points for ϕ, such that $\Delta\phi = 0.0025$, and into L grid points for $\mathrm{S_w}$, such that $\Delta\mathrm{S_w} = 0.025$. An unconstrained least squares procedure, (4.5), was chosen for the second inversion step from elastic parameters to saturation and porosity. Effective elastic reservoir properties, $\mathbf{m}_{\mathrm{calc}} = \mathbf{G}\left(\mathrm{S_w}.\phi\right)$, was calculated for each combination of saturation and porosity and compared to the observed elastic properties:

$$\mathrm{J}\left(\mathbf{m}_{\mathrm{calc}}\right) = ||\mathbf{m}_{\mathrm{obs}} - \mathbf{m}_{\mathrm{calc}}||_2^2 \tag{6.26}$$

Finally, the inverted reservoir model was the combination of water saturation and porosity that gave the smallest residual norm. The work flow for a classical approach to a two-step inversion with a prior model is summarized in figure 6.4.

Inversion results

The classical approach to a two-step inversion with a prior model was tested on seismic data (figure 6.3) that had been modelled from an earth model (figure 6.2) with an oil and water saturated reservoir section which corresponded to case 6a in table 3.2. Figures 6.6 to 6.8 show the the first inversion step to elastic earth models for three cases dealing with increasing noise levels in the seismic data. In each figure, the left plot is the P-wave velocity, the centre plot is the S-wave velocity and the right plot is the density. The solid red line is the true model, the dashed green line is the prior model and the solid blue line is the inverted model, $\mathbf{m}_\lambda$.

Case 1a. The percentage noise of the maximum amplitude in the seismic data was set to $\mathrm{p} = 10^{-5}$ using (6.21). Figure 6.6 shows the result for the first inversion step for this particular case. A selection of the regularization parameters for this noise level is shown in the top plot of figure 6.5. The regularization

level was minor due to such a low noise level: $\lambda_0 = 0.8^{40}$ and $\lambda_1 = 2 \cdot \lambda_0$. Clearly, the inverted model (solid blue) followed the true model (solid red) for all three elastic parameters. There were only small deviations from the true model. Following this, the second inversion step from the elastic earth model to water saturation and porosity gave $S_w = 95\%$ and $\phi = 29.75\%$. Compared to the true values, that was exactly the water saturation and only a minor deviation in porosity. We may conclude that both the inverted elastic earth model and the inverted water saturation and porosity were very satisfactory in this case.

Case 2a. The percentage noise of the maximum amplitude in the seismic data was set to $p = 10^{-4}$ using (6.21). Figure 6.7 shows the result for the first inversion step for this particular case. A selection of the regularization parameters for this noise level is shown in the centre plot of figure 6.5. It was necessary to increase the regularization parameters, $\lambda_0 = 0.8^{27}$ and $\lambda_1 = 2 \cdot \lambda_0$, in order to stabilize the solution for the higher noise level. Clearly, the inverted model (solid blue) followed the true model (solid red) for all three elastic parameters. There were only small deviations from the true solution. Following this, the second inversion step from the elastic earth model to water saturation and porosity gave $S_w = 97.5\%$ and $\phi = 30\%$. Compared to the true values, that was exactly the porosity and only a minor deviation in water saturation. We may conclude that both the inverted elastic earth model and the inverted water saturation and porosity were very satisfactory in this case.

Case 3a. The percentage noise of the maximum amplitude in the seismic data was set to $p = 10^{-3}$ using (6.21). Figure 6.8 hows the result for the first inversion step for this particular case. A selection of the regularization parameters for this noise level is shown in the centre plot of figure 6.5. It was necessary to increase the regularization parameters substantially, $\lambda_0 = 0.8^{7}$ and $\lambda_1 = 2 \cdot \lambda_0$, in order to stabilize the solution. The inverted model (solid blue) appeared to be very biased towards the prior model: the deviations from the true model (solid red) increased substantially for the sections were the prior model was more inaccurate. Following this, the second inversion step from the elastic earth model to water saturation and porosity gave $S_w = 97.5\%$ and $\phi = 29.5\%$. Compared to the true values, that was only a minor deviation in water saturation and porosity. We may conclude that the inverted elastic earth model was satisfactory for a sufficiently accurate prior model and the inverted water saturation and porosity was very satisfactory in this case.

6.3.2 A Bayesian approach to a two-step inversion

Inversion Procedure

A Bayesian linearized inversion procedure was used for the first inversion step from seismic data to elastic earth models. In section 4.2.2, an analytical solution for a Bayesian linearized inversion was presented. A prerequisite is that both the prior model and the data has multivariate normal distributions. The expectation of the prior model, $\mathbf{m}_0$, was defined in the same manner as for Tikhonov with prior. In addition, an associated block-diagonal prior model covariance matrix, $\mathbf{C}_{m_0}$, was defined

as:

$$\mathbf{C}_{\mathrm{m}_0} = \begin{bmatrix} \mathbf{C}_{\mathrm{V_P}} & \mathbf{0} & \mathbf{0} \\ \mathbf{0} & \mathbf{C}_{\mathrm{V_S}} & \mathbf{0} \\ \mathbf{0} & \mathbf{0} & \mathbf{C}_{\rho} \end{bmatrix} \tag{6.27}$$

The parameter distributions were assumed identical such that $\sigma^2_{\mathrm{m}_0} = 0.05^2$. The optimization problem is given by the following objective function (4.21):

$$\mathrm{J}(\mathbf{m}) = \frac{1}{2}(\mathbf{G}\mathbf{m} - \mathbf{d})^{\mathrm{T}} \mathbf{C}_{\mathrm{d}}^{-1} (\mathbf{G}\mathbf{m} - \mathbf{d}) + \frac{1}{2}(\mathbf{m} - \mathbf{m}_0)^{\mathrm{T}} \mathbf{C}_{\mathrm{m}_0}^{-1} (\mathbf{m} - \mathbf{m}_0) \tag{6.28}$$

A maximum a posteriori solution, $\mathbf{m}_{\mathrm{map}}$, is then given by (4.22):

$$\mathbf{m}_{\mathrm{map}} = \left(\mathbf{G}^{\mathrm{T}}\mathbf{C}_{\mathrm{d}}^{-1}\mathbf{G} + \mathbf{C}_{\mathrm{m}_0}^{-1}\right)^{-1} \left(\mathbf{G}^{\mathrm{T}}\mathbf{C}_{\mathrm{d}}^{-1}\mathbf{d} + \mathbf{C}_{\mathrm{m}_0}^{-1}\mathbf{m}_0\right) \tag{6.29}$$

and the corresponding posterior covariance matrix, $\mathbf{C}_{\mathrm{m}'}$ (4.23):

$$\mathbf{C}_{\mathrm{m}'} = \left(\mathbf{G}^{\mathrm{T}}\mathbf{C}_{\mathrm{d}}^{-1}\mathbf{G} + \mathbf{C}_{\mathrm{m}_0}^{-1}\right)^{-1} \tag{6.30}$$

It was important to keep in mind that the model parameters were logarithmic when the 95% confidence interval for the posterior distribution was calculated:

$$\mathbf{m}_{\mathrm{map}} \pm \mathrm{e}^{\mathbf{m}_{\mathrm{map}} + 1.96 \cdot \mathrm{diag}(\mathbf{C}_{\mathrm{m}'})} \tag{6.31}$$

A nonlinear Bayesian inversion procedure with an uninformative prior, as discussed in section 4.3, was adopted for the second inversion step from elastic parameters to saturation and porosity. Two column vectors of expectation values, $\boldsymbol{\mu}_{\mathrm{m}'}$, and variances, $\boldsymbol{\sigma}^2_{\mathrm{m}'}$, for the inverted elastic earth models, were split into parts corresponding to the elastic parameters. Time samples from the middle of the reservoir sections were subsequently chosen from each of them. Following this, a vector of observed elastic reservoir properties, $\mathbf{m}_{\mathrm{obs}}$, and a corresponding diagonal covariance matrix, $\mathbf{C}_{\mathrm{obs}}$, could be defined. Further, it had been assumed that the effective elastic properties were a function of only saturation and porosity, $\mathbf{m}_{\mathrm{res}} = [\mathrm{S_w}, \phi]$, in the forward modelling, $\mathbf{m}_{\mathrm{calc}} = \mathbf{G}(\mathbf{m}_{\mathrm{res}})$. In order to find an optimal choice of reservoir parameters for the observed effective elastic reservoir properties, an objective function $\mathrm{J}(\mathbf{m}_{\mathrm{res}})$, was defined as:

$$\mathrm{J}(\mathbf{m}_{\mathrm{res}}) = (\mathbf{m}_{\mathrm{calc}} - \mathbf{m}_{\mathrm{obs}})^{\mathrm{T}} \mathbf{C}_{\mathrm{obs}}^{-1} (\mathbf{m}_{\mathrm{calc}} - \mathbf{m}_{\mathrm{obs}}) \tag{6.32}$$

A solution of a posterior PDF based on Gaussian statistics is given by (4.25).

$$\mathrm{q}(\mathbf{m}|\mathbf{d}) = \mathrm{N} \cdot e^{-\mathrm{J}(\mathbf{m})} \tag{6.33}$$

The posterior and marginal PDFs for porosity and saturation were calculated by following the same

procedure as in section 5.2. The work flow for both inversion steps are summarized in figure 6.9.

Inversion results

The Bayesian approach to a two-step inversion was tested on seismic data (figure 6.3) that had been modelled from an earth model (figure 6.2) with an oil and water saturated reservoir section which corresponded to case 6a in table 3.2. Figures 6.10 to 6.12 show the results for the first inversion step for the three cases with increasing noise levels. In each figure, the left plot is the P-wave velocity, the centre plot is the S-wave velocity and the right plot is the density. The solid blue lines are the maximum a posteriori solution, the dashed blue lines are 95% confidence intervals for the map solution, the dashed green lines are 95% confidence intervals for the prior model and solid red lines is the true model. Figures 6.13 to 6.15 show the corresponding results for the second inversion step from elastic earth models to water saturation and porosity. In each figure, the top plot is the posterior distribution, the centre plot is the marginal distribution of water saturation (solid blue line) and the bottom plot is the marginal distribution of porosity (solid blue line). The true values are marked as solid red lines in the centre and bottom plot.

Case 1c. The percentage noise of the maximum amplitude in the seismic data was set to $\mathrm{p} = 10^{-5}$ using (6.21). Figure 6.10 shows the result for the first inversion step for this particular case. The percent wise decrease of the mean width of the 95% confidence intervals from the prior model to the posterior model was 83% for P-wave velocity, 82% for S-wave velocity and 83% for density. Clearly, the inverted model (solid blue) match the true model (solid red) perfectly for all three elastic parameters. Figure 6.13 shows the result for the second inversion step for this particular case. The maxima of the marginal distributions for both water saturation and porosity (solid blue lines) were close to the true values (solid red lines). Also, the width of the marginal distributions were relatively narrow, which indicates low uncertainty. We may conclude that both inversion steps gave very satisfactory results.

Case 2c. The percentage noise of the maximum amplitude in the seismic data was set to $\mathrm{p} = 10^{-4}$ using (6.21). Figure 6.11 shows the result for the first inversion step for this particular case. The percent wise decrease of the mean width of the 95% confidence intervals from the prior model to the posterior model was 54% for P-wave velocity, 50% for S-wave velocity and 54% for density. Clearly, the inverted model (solid blue) match the true model (solid red) almost perfectly for all three elastic parameters. Figure 6.14 shows the result for the second inversion step for this particular case. The maxima of the marginal distributions for both water saturation and porosity (solid blue lines) were close to the true values (solid red lines). There was only a small underestimate in porosity. However, the width of the marginal distributions were considerably wider than for case 1c. We may conclude that both inversion steps gave satisfactory results.

Case 3c. The percentage noise of the maximum amplitude in the seismic data was set to $\mathrm{p} = 10^{-3}$ using (6.21). Figure 6.12 shows the result for the first inversion step for this particular case. The percent wise decrease of the mean width of the 95% confidence intervals from the prior model to the

posterior model was reduced to 42% for P-wave velocity, only 27% for S-wave velocity and 32% for density. Clearly, the inverted model (solid blue) match the true model (solid red) closely for all three elastic parameters. Figure 6.15 shows the result for the second inversion step for this particular case. The maxima of the marginal distributions for both water saturation and porosity (solid blue lines) were close to the true values (solid red lines). There was only a small underestimate in porosity. However, the width of the marginal distributions were very wide, which indicates high uncertainty. We may conclude that both inversion steps gave satisfactory results. However, the second inversion step had very high uncertainties in water saturation and porosity.

6.4 Discussion

Three parameter AVA inversion is a very ill-conditioned problem for conventional noise levels and acquisition geometries. That is, a small amount of noise will result in large parameter deviations. A common approach to this problem has been to rearrange Aki-Richards approximation for other parameterizations (Fatti et al., 1994; Shuey, 1985; Smith and Gidlow, 1987). Following this, hard constraints were generally put on the density reflectivity in order to improve the stability of the problem. This is undesirable since density estimates are necessary in order to quantify several rock physical parameters such as saturation (Avseth et al., 2005). An alternative approach could be to increase the range of incident angles in the AVA data since the density reflectivity is associated with large incident angles (Drufuca and Mazzotti, 1995; Shuey, 1985). However, the accuracy of linearized approximations to the reflection coefficients, such as Aki-Richards approximation, decreases with higher incident angles as demonstrated in chapter 3. The best option would be to improve the stability by inclusion of mode converted waves and shear waves into the inversion algorithm (De Haas and Berkhout, 1988). This is often not an option in marine seismic surveys since shear waves cannot travel trough water. A final option, and the most viable alternative (Martinez and McMechan, 1991), would be to stabilize the solution by inclusion of a prior model into the object function as was chosen here.

The classical approach to a two-step inversion with a prior gave very satisfactory results for the two lowest noise levels. It was evident that the choice of prior model would determine the chance of success for highest noise. An advantage of choosing a classical approach to inversion is that the regularization parameters are determined from the observed data. Further, we do not put any statistical constraints on the prior model. However, the Bayesian approach to a two-step inversion presents a good framework for statistical analysis of the inversion results. Also, all questions about model resolution are addressed by the posterior PDFs in each inversion step. In the first inversion step, the reduction in the mean width of the 95% confidence intervals from the prior model to the posterior model implied that the resolution of P-wave velocity is superior to that of the S-wave velocity and density. As for the second inversion step, the width of the distributions implied that the water saturation and porosity may be determined for low to medium data uncertainty. High data uncertainties would likely not give any good estimates of water saturation and porosity since the marginal PDFs are very wide.

The main conclusion is that linearized inversion from PP-reflection coefficients AVA data to three elastic parameters may be stabilized by prior models from well logs. Inversion from elastic reservoir properties to water saturation and porosity is feasible was feasible for the two lowest noise levels. A Bayesian two-step inversion algorithm should only be used when you can justify characterizing the prior information probabilistically. A classical two-step inversion algorithm is a viable alternative, but does not provide the same framework for statistical analysis of the inversion results.

Table 6.1: The elastic properties of an earth model with an oil and water saturated reservoir section.

Layer	$V_P\,(ms^{-1})$	$V_S\,(ms^{-1})$	$\rho\,(Kgm^{-3})$	Thickness (m)
1	3050	1800	2470	290
2 (Top)	3120	1870	2490	
2 (Bottom)	3150	1900	2500	200
3 (Reservoir rock)	2948	1675	2158	410
4 (Underburden)	3120	1870	2490	100

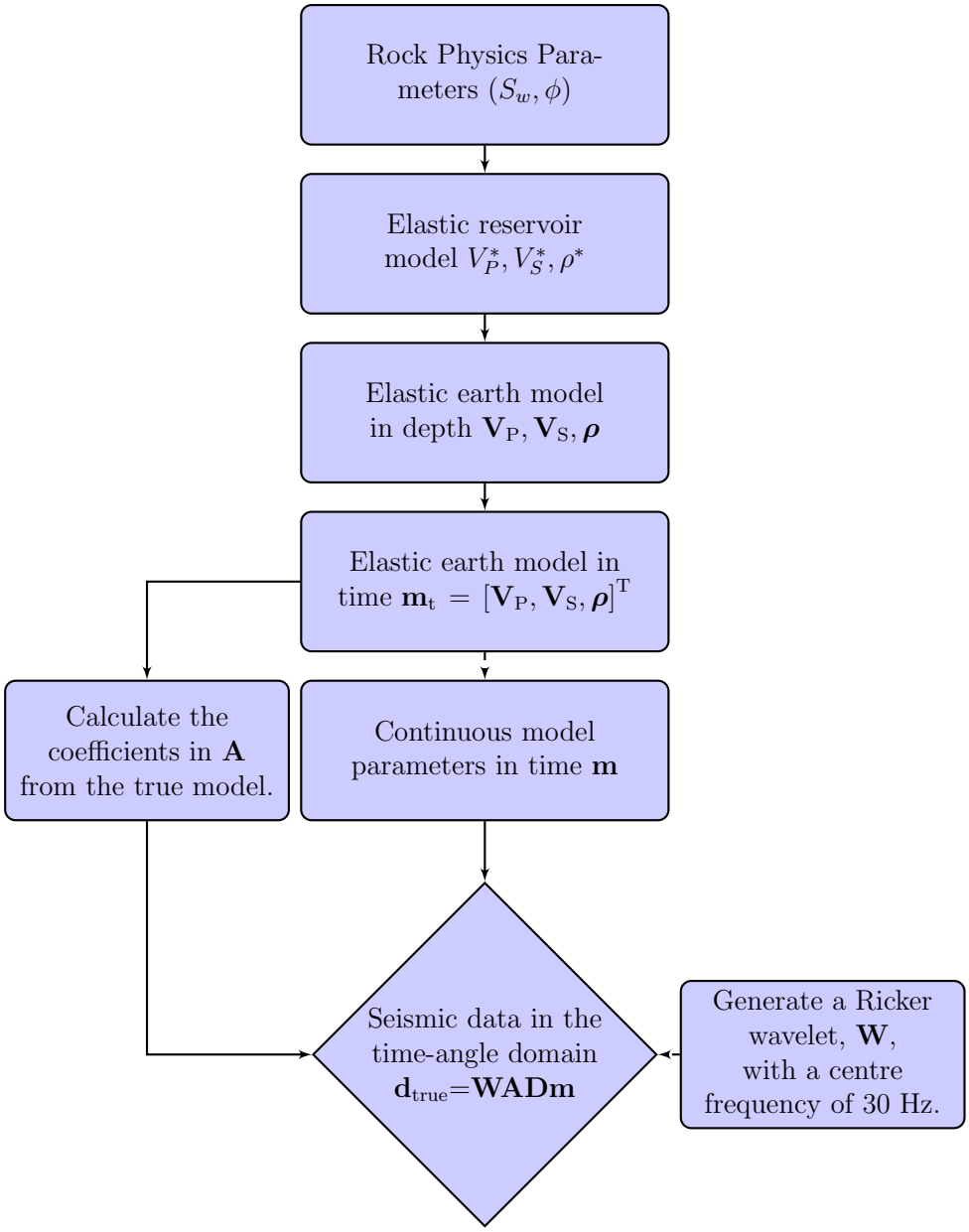

Figure 6.1: The work flow for waveform modelling with Aki-Richards approximation in the time-angle domain.

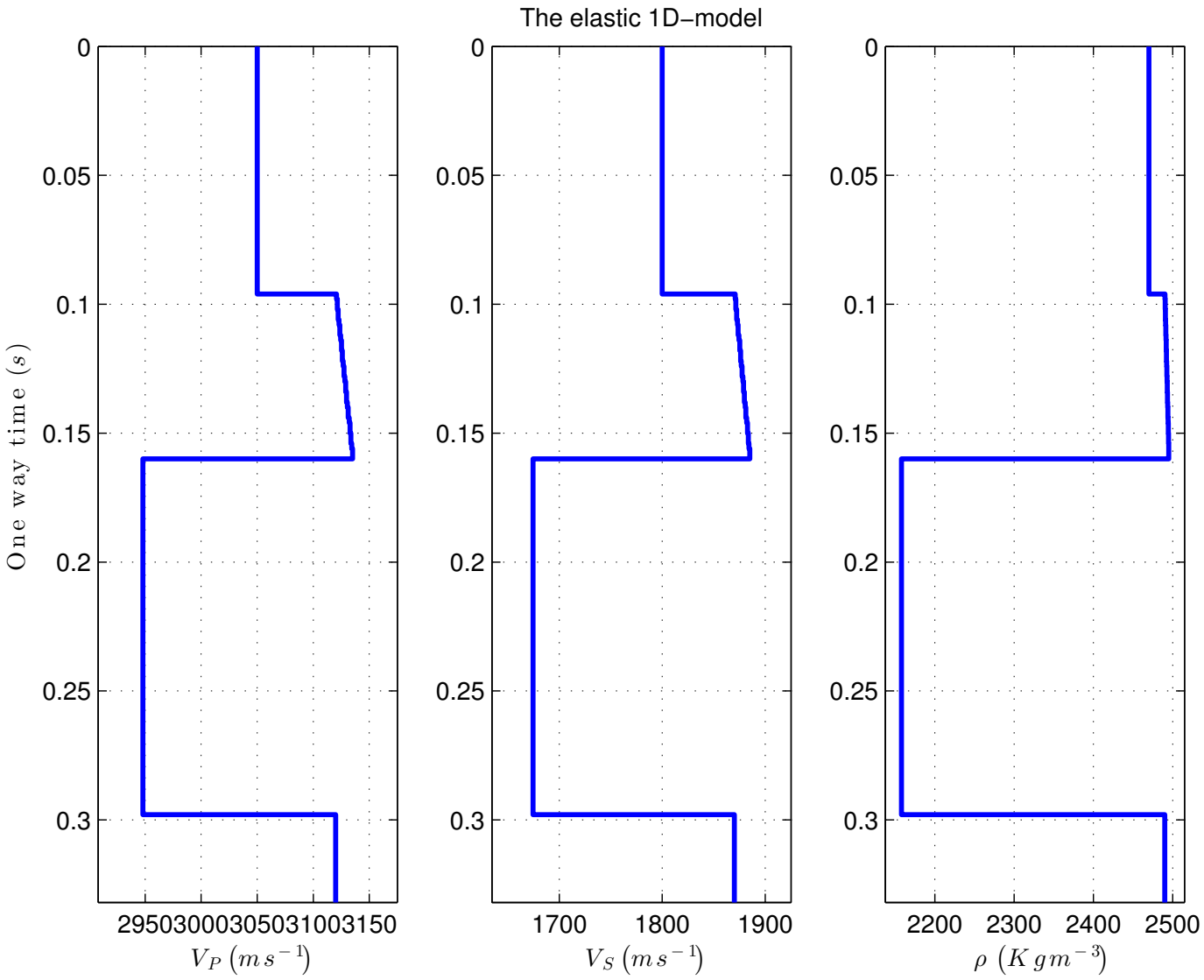

Figure 6.2: An elastic earth model with an oil and water saturated reservoir section ($\phi = 30\%, \mathrm{S_w} = 95\%$). P-wave velocity (left), S-wave velocity (centre) and density (right).

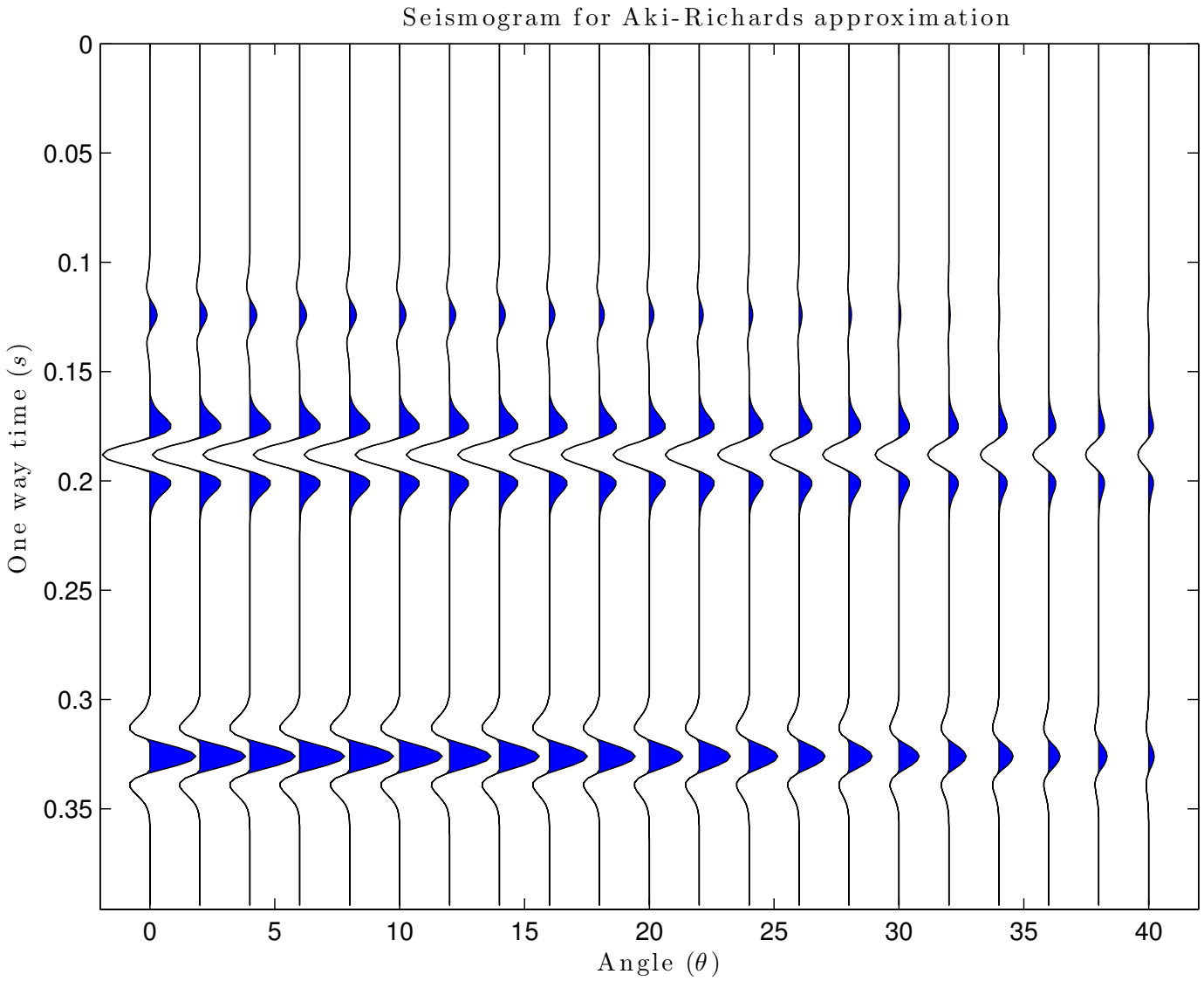

Figure 6.3: The synthetic seismogram obtained by waveform modelling with Aki-Richards approximation. An earth model with an oil and water saturated reservoir section.

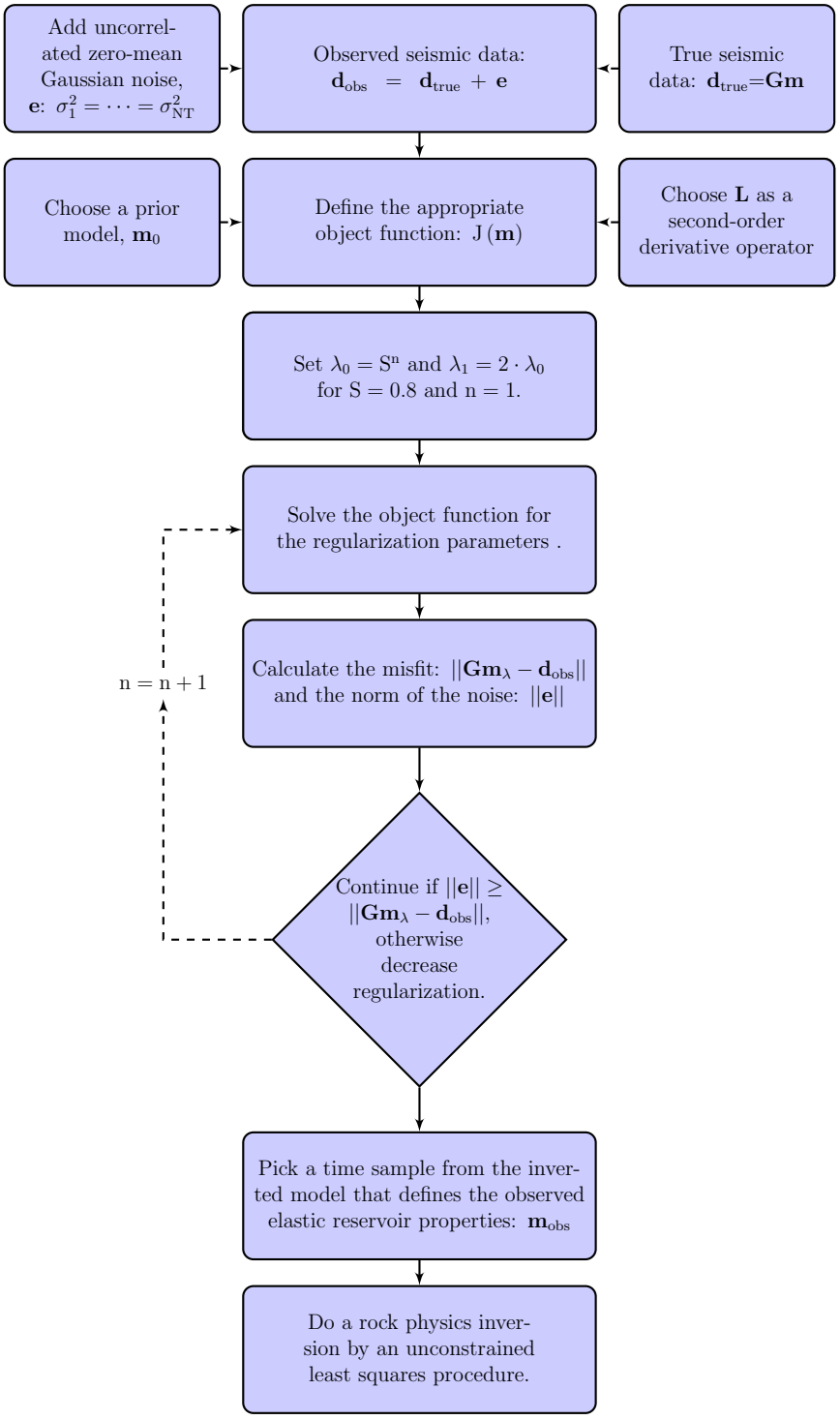

Figure 6.4: A work flow for a classical approach to a two step inversion with a prior model. The first inversion step is from AVA data for a stratified earth model to an elastic 1D model using Tikhonov inversion with prior. The second inversion step is from a time sample corresponding to the reservoir section to water saturation and porosity by an unconstrained least squares procedure.

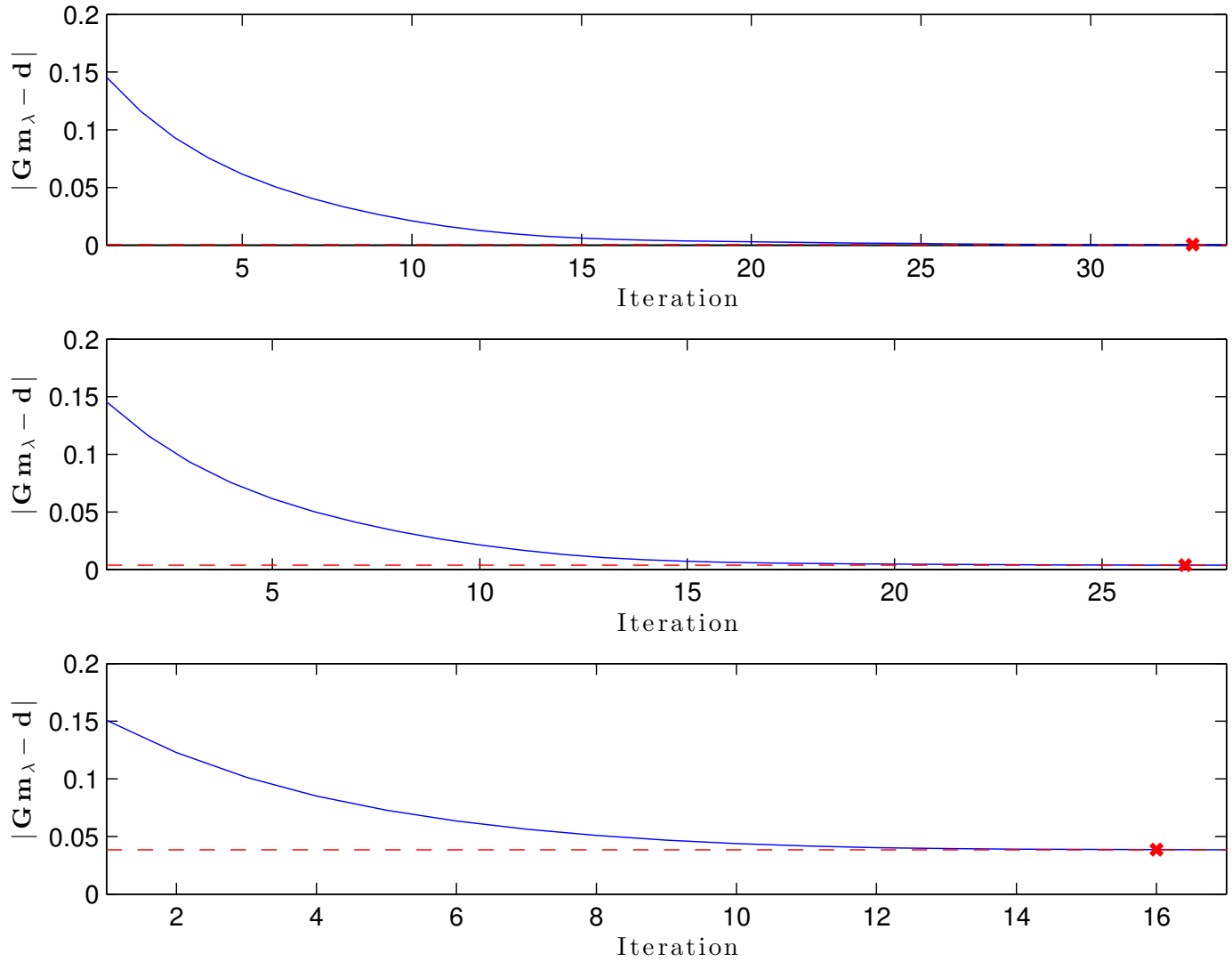

Figure 6.5: Selection of the regularization parameters for the penalty functionals in the Tikhonov solution. Every iteration, n, reduces the them exponentially as: $\lambda_0 = \mathrm{J}^{\mathrm{n}}$ and $\lambda_1 = 2 \cdot \lambda_0$. The red dotted line is a threshold which marks the norm of the gaussian data errors. A model with an oil and water saturated reservoir section: Case 1 (top), case 2 (center) and case 3 (bottom).

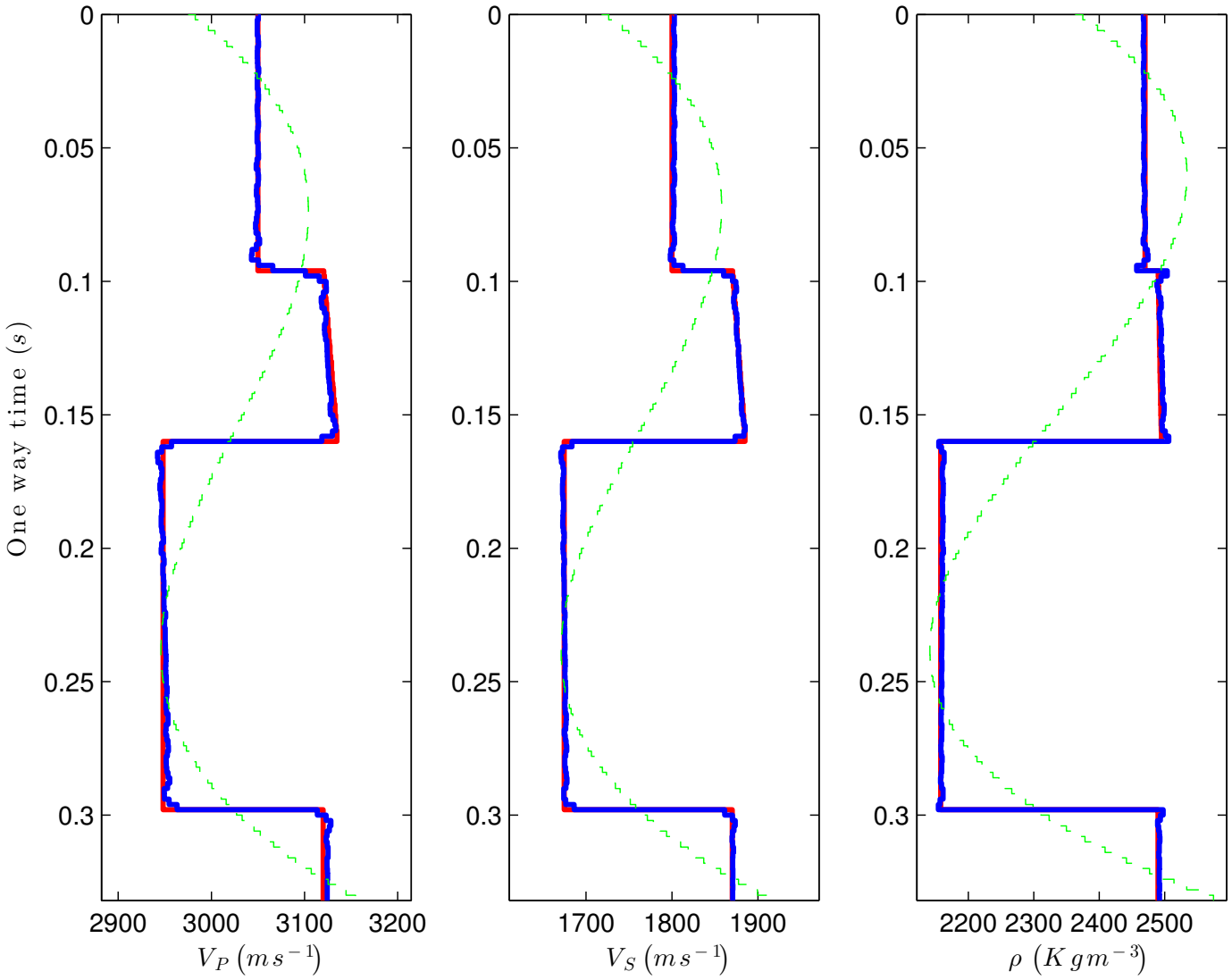

Figure 6.6: The inverted model (solid blue line), the true model (solid red) and the prior model (dashed green lines). A case with the noise level set to $\sigma_{\mathrm{d}}^2 = (10^{-5} \cdot \max|\mathbf{d}|)^2$ (case 1a).

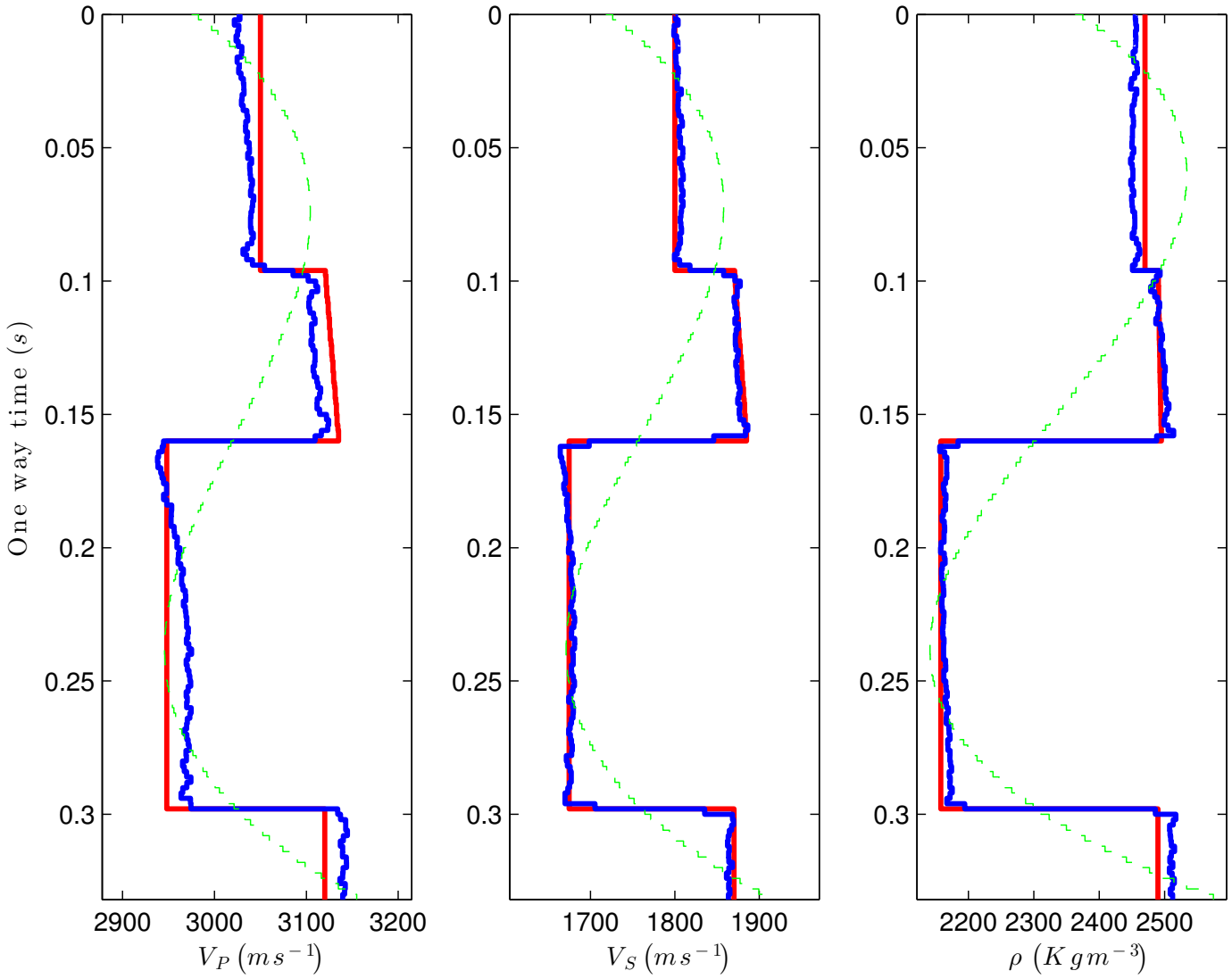

Figure 6.7: The inverted model (solid blue line), the true model (solid red) and the prior model (dashed green lines). A case with the noise level set to $\sigma_{\mathrm{d}}^2 = (10^{-4} \cdot \max|\mathbf{d}|)^2$ (case 2a).

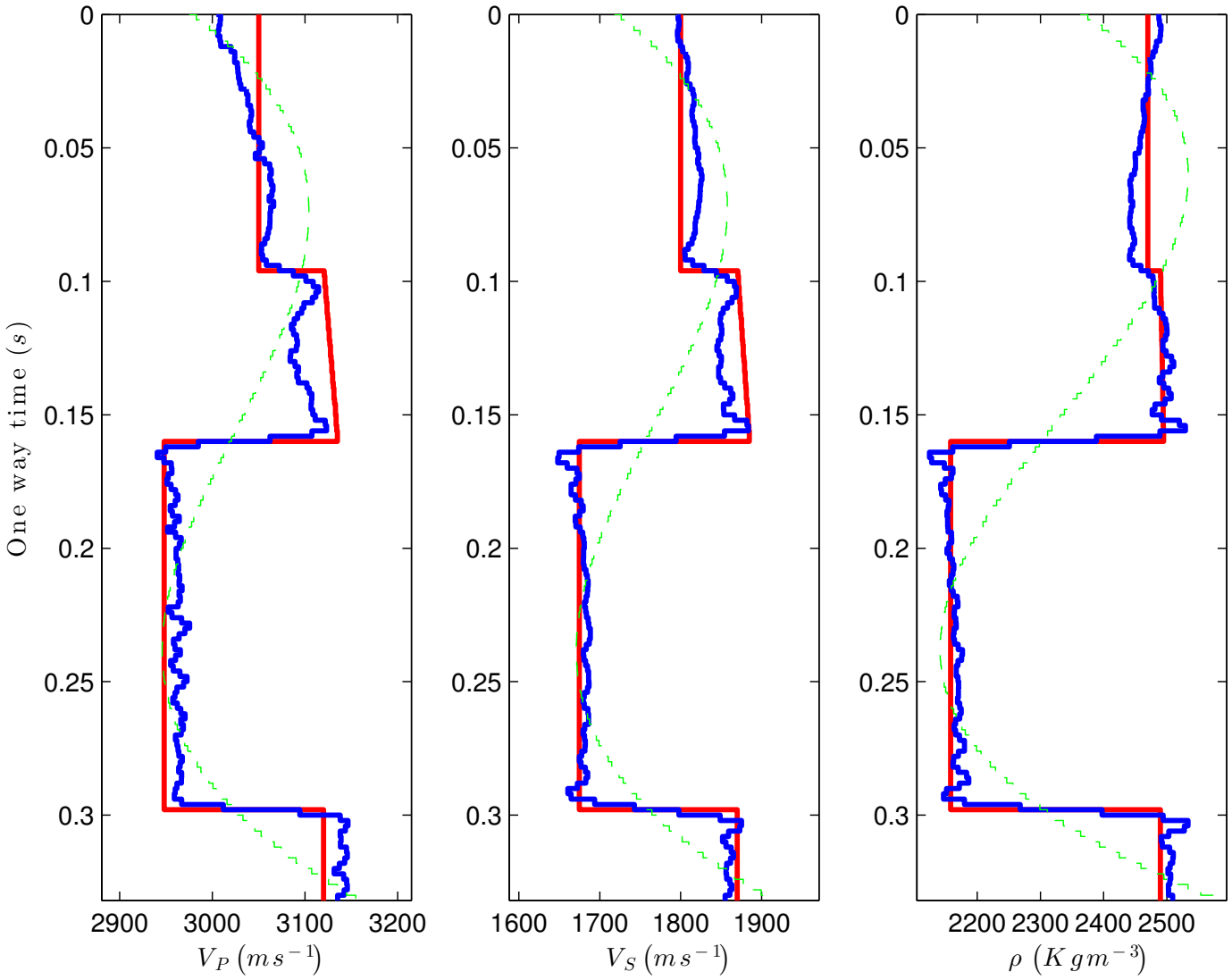

Figure 6.8: The inverted model (solid blue line), the true model (solid red) and the prior model (dashed green lines). A case with the noise level set to $\sigma_{\mathrm{d}}^2 = (10^{-3} \cdot \max|\mathbf{d}|)^2$ (case 3a).

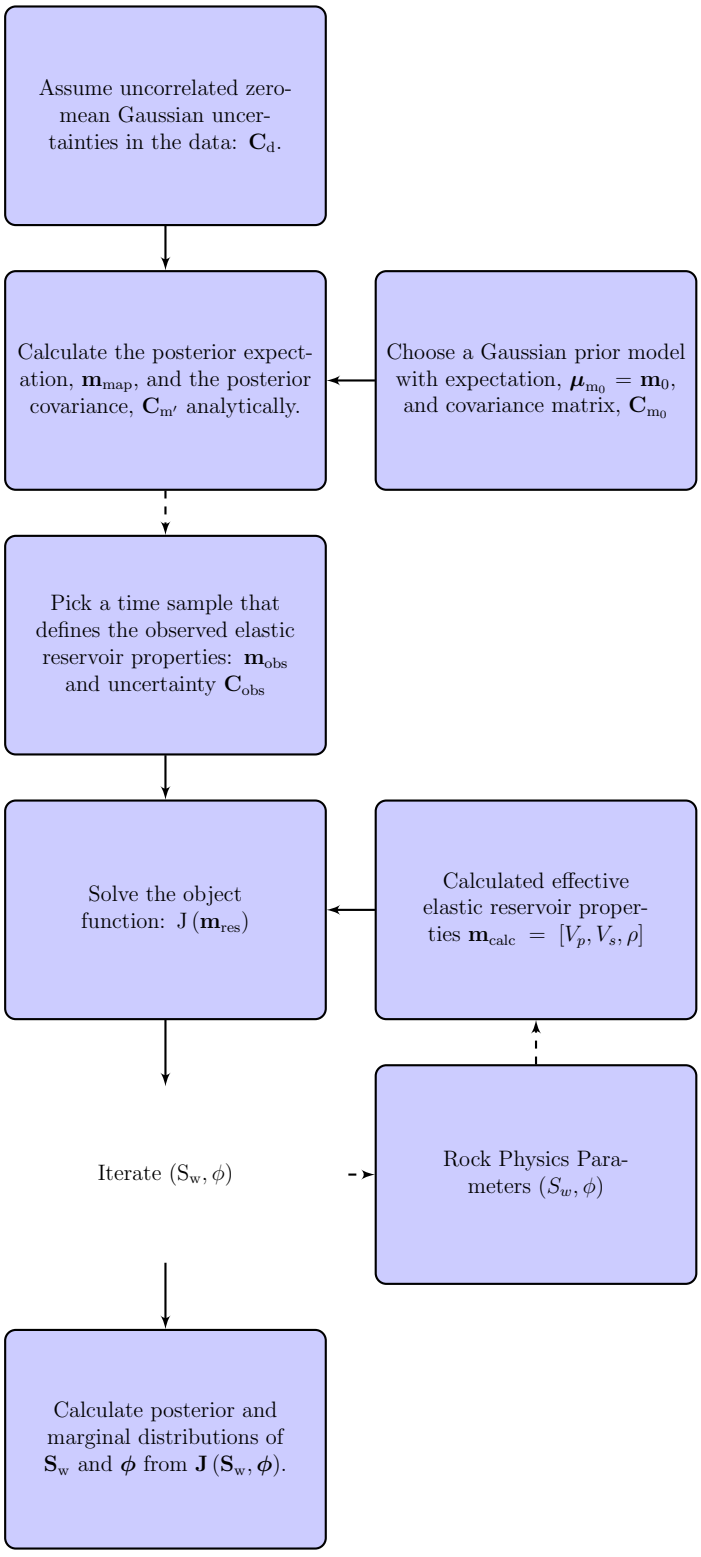

Figure 6.9: A work flow for a Bayesian approach to a two step inversion. The first inversion step is from AVA data for a stratified earth model to an elastic 1D model using a linearized Bayesian procedure for minimization. The second inversion step is from a time sample corresponding to the reservoir section to water saturation and porosity by an nonlinear Bayesian inversion with an uninformative prior.

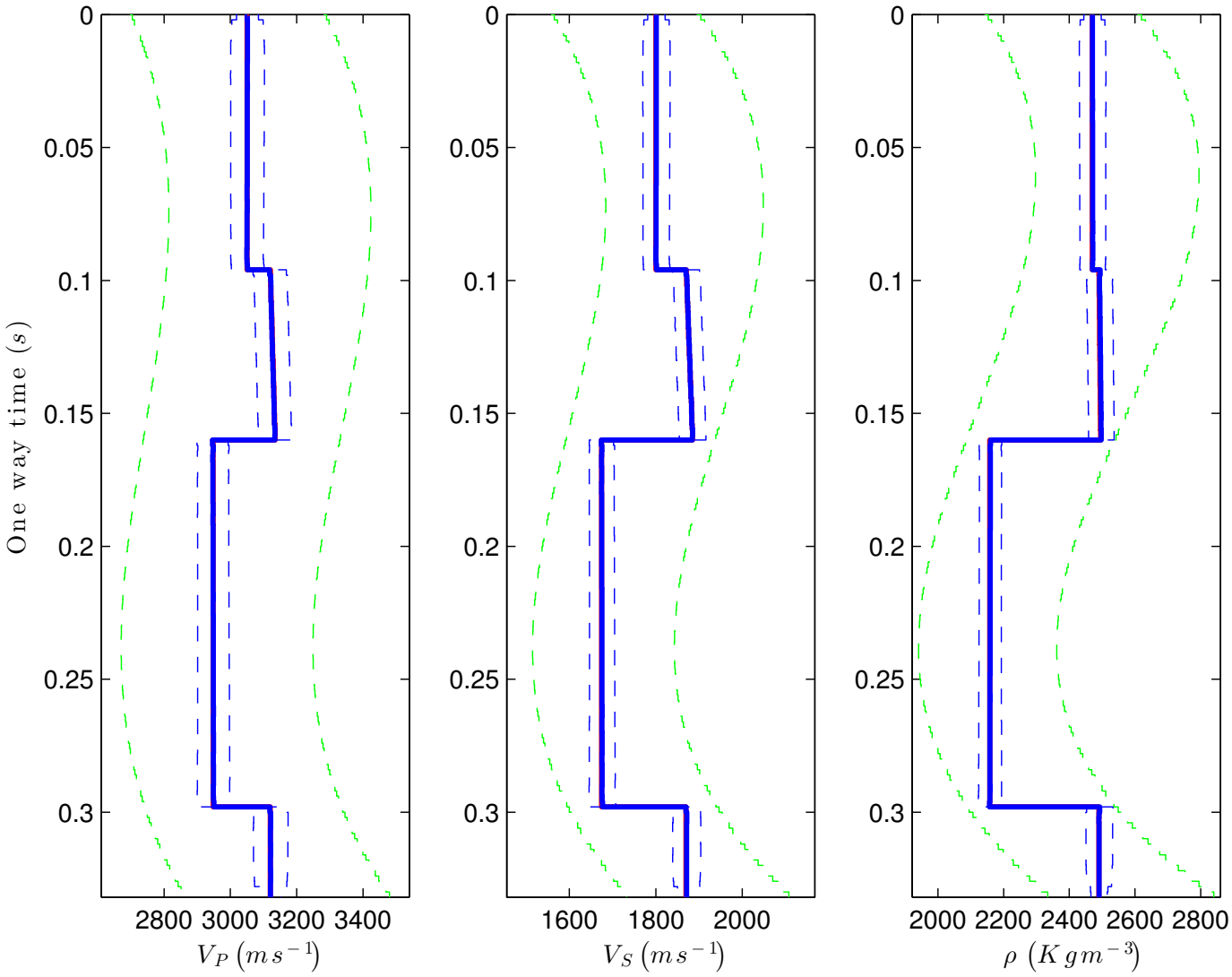

Figure 6.10: The map solution (solid blue line) with 95% prediction intervals (dashed blue lines) and 95% prediction intervals for the prior model (dashed green lines). A model with an oil and water saturated reservoir section ($\phi = 30\%, \mathrm{S_w} = 95\%$) (solid red line) and the noise level set to $\sigma_{\mathrm{d}}^2 = (10^{-5} \cdot \max|\mathbf{d}|)^2$ (case 1b).

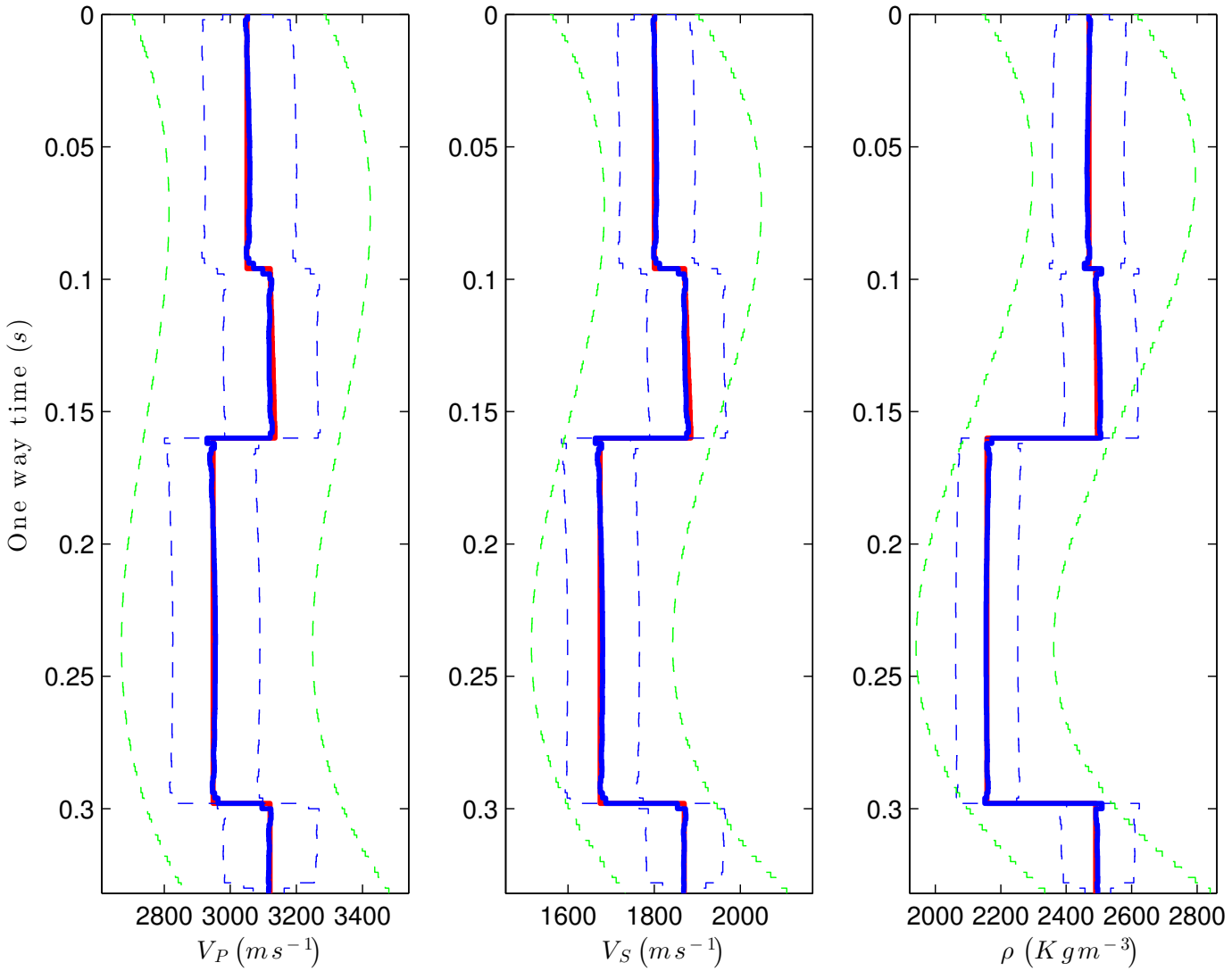

Figure 6.11: The map solution (solid blue line) with 95% prediction intervals (dashed blue lines) and 95% prediction intervals for the prior model (dashed green lines). A model with an oil and water saturated reservoir section ($\phi = 30\%, \mathrm{S_w} = 95\%$) (solid red line) and the noise level set to $\sigma_{\mathrm{d}}^2 = (10^{-4} \cdot \max|\mathbf{d}|)^2$ (case 2b).

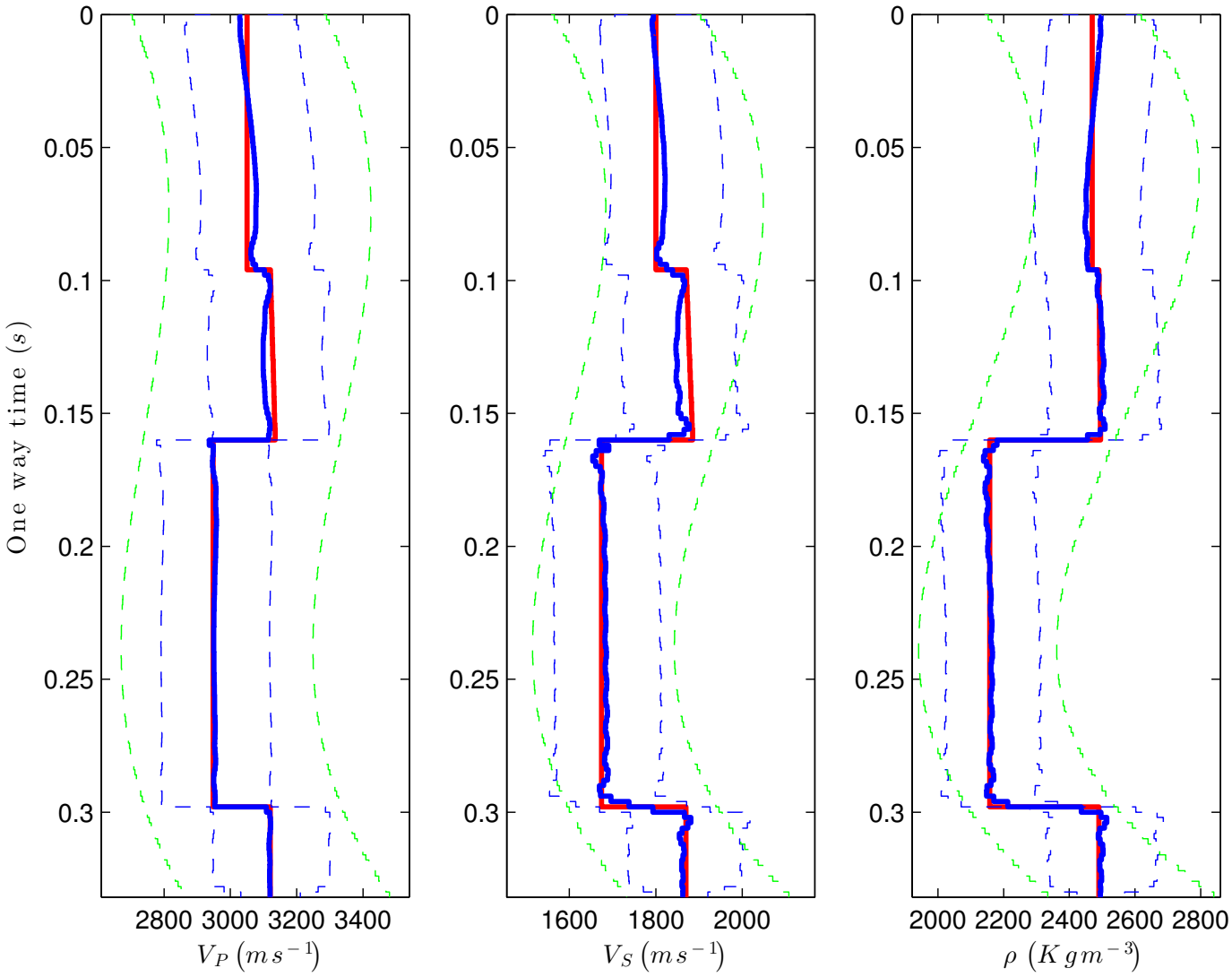

Figure 6.12: The map solution (solid blue line) with 95% prediction intervals (dashed blue lines) and 95% prediction intervals for the prior model (dashed green lines). A model with an oil and water saturated reservoir section ($\phi = 30\%, \mathrm{S_w} = 95\%$) (solid red line) and the noise level set to $\sigma_{\mathrm{d}}^2 = (10^{-3} \cdot \max|\mathbf{d}|)^2$ (case 3b).

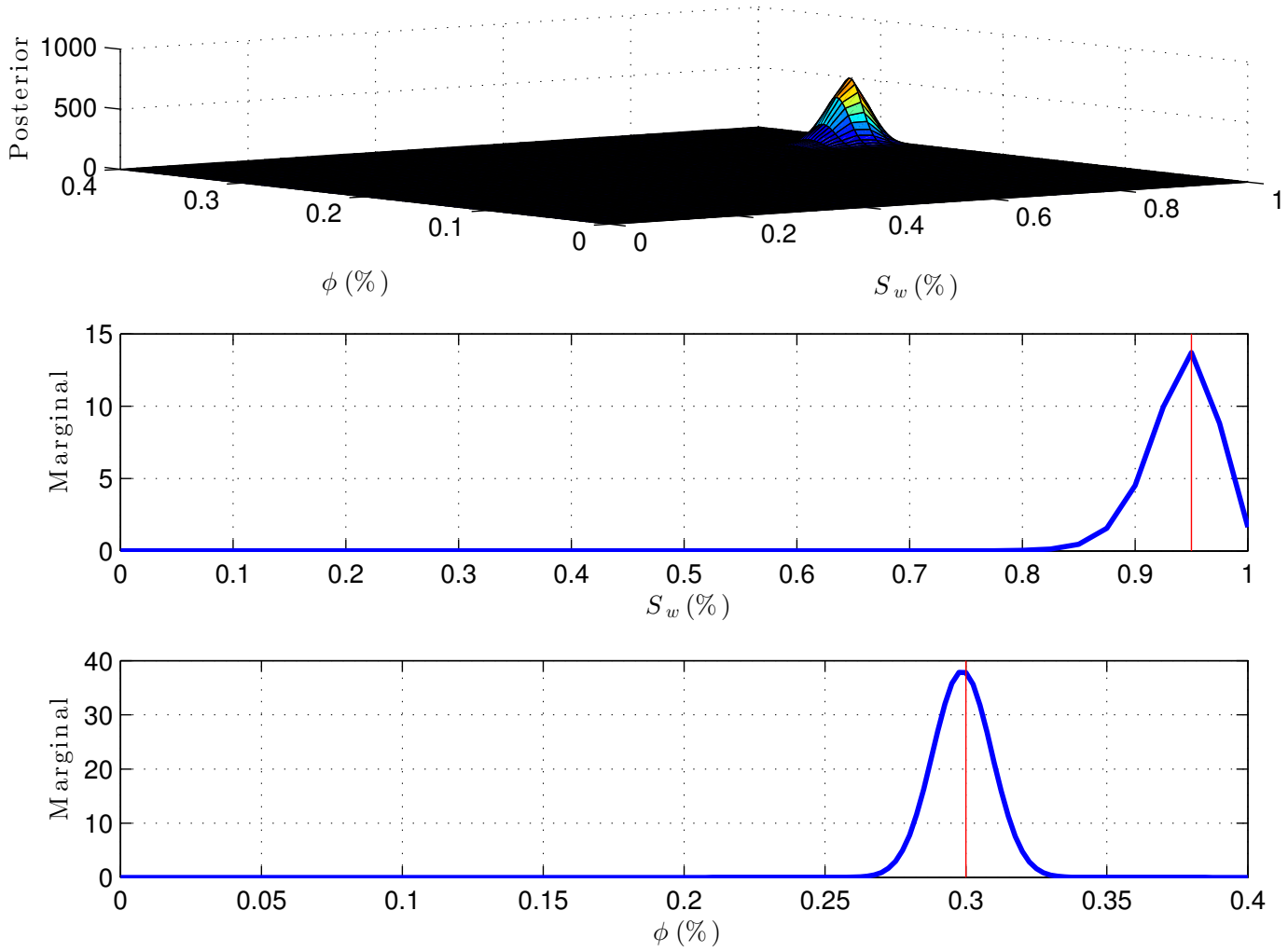

Figure 6.13: The rock physics inversion for a model with an oil and water saturated reservoir section ($\phi = 30\%, \mathrm{S_w} = 95\%$) (solid red lines) and the noise level set to $\sigma_{\mathrm{d}}^2 = (10^{-5} \cdot \max|\mathbf{d}|)^2$ case (1b). The posterior distribution (top), marginal distribution of saturation (center) and marginal distribution of porosity (bottom). A Bayesian approach to a two-step inversion was adopted.

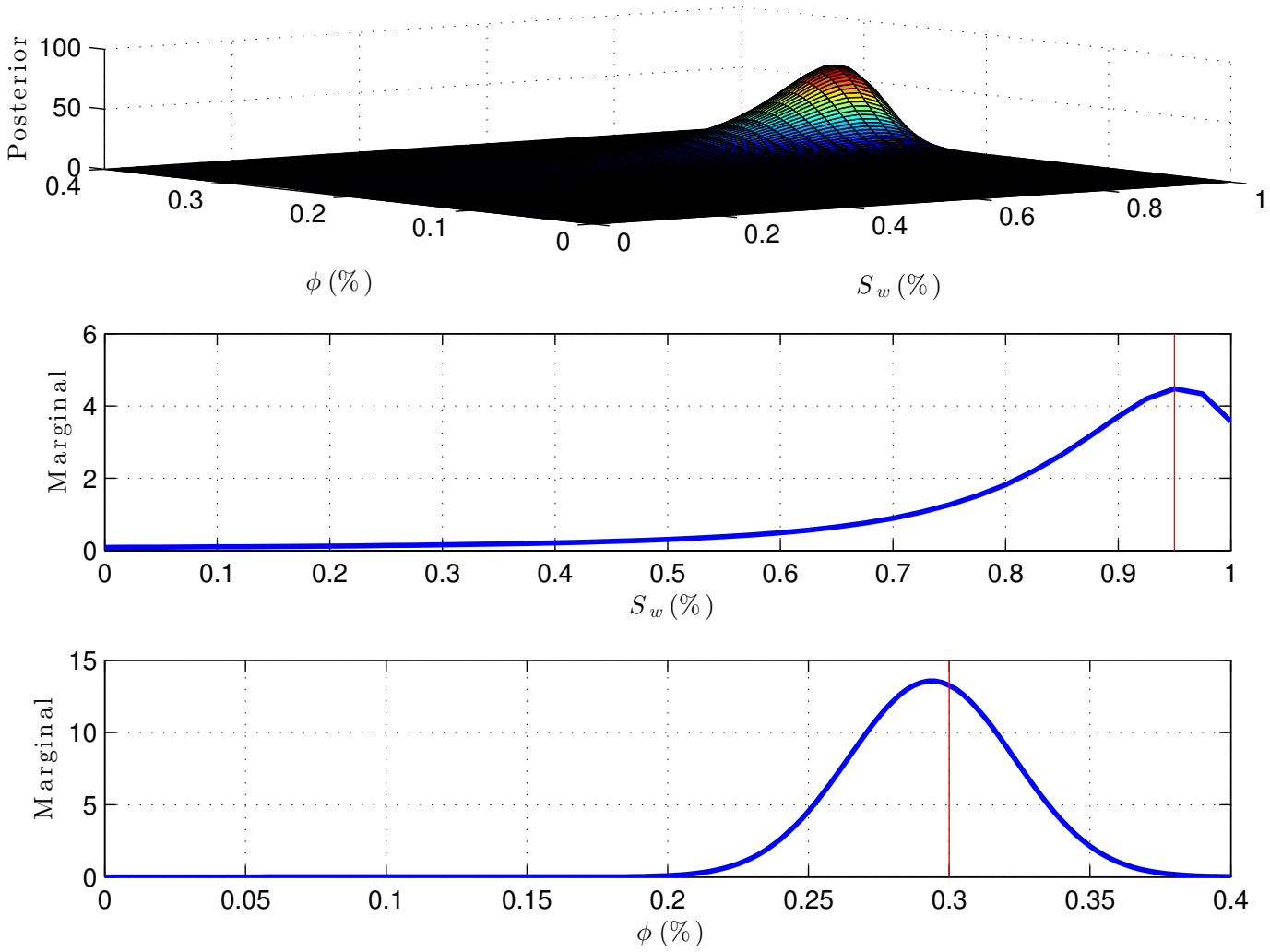

Figure 6.14: The rock physics inversion for a model with an oil and water saturated reservoir section ($\phi = 30\%, \mathrm{S_w} = 95\%$) (solid red lines) and the noise level set to $\sigma_{\mathrm{d}}^2 = (10^{-4} \cdot \max|\mathbf{d}|)^2$ (case 2b). The posterior distribution (top), marginal distribution of saturation (center) and marginal distribution of porosity (bottom). A Bayesian approach to a two-step inversion was adopted.

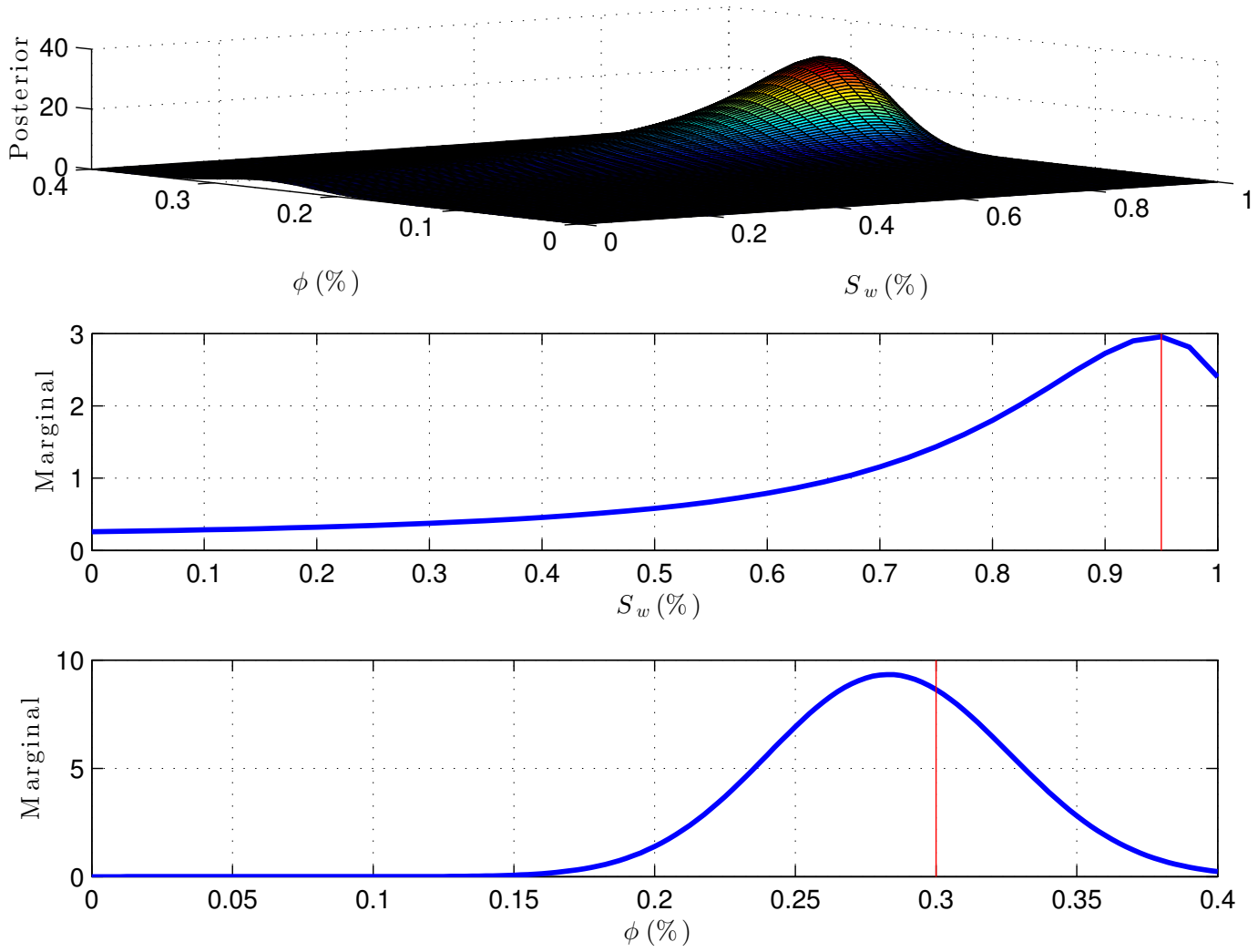

Figure 6.15: The rock physics inversion for a model with an oil and water saturated reservoir section ($\phi = 30\%, \mathrm{S_w} = 95\%$) (solid red lines) and the noise level set to $\sigma_{\mathrm{d}}^2 = (10^{-3} \cdot \max|\mathbf{d}|)^2$ (case 3b). The posterior distribution (top), marginal distribution of saturation (center) and marginal distribution of porosity (bottom). A Bayesian approach to a two-step inversion was adopted.

Chapter 7

Concluding remarks and suggestions for future work

7.1 Concluding remarks

The main topic of this thesis was to perform inversion of seismic AVA data to saturation and porosity using a rock physics model. Along with this, three secondary objectives were investigated. First, the effect of the error introduced by Aki-Richards approximation in AVA modelling for determination of saturation and porosity by a one-step inversion procedure. Secondly, the effect of spatial variations in crack density for determination of saturation and porosity. Following this, two-step inversions algorithms from AVA data to stratified elastic earth models with a reservoir section and on to saturation and porosity were demonstrated.

It was demonstrated that the deviation from the exact reflection coefficient increases as the angle of incidence increases. The error depends on the combination of relative contrasts in elastic properties. There are other modelling errors which have not been taking into account in this thesis: First, the incident angles and the coefficients in both the Zoeppritz equations and Aki-Richards approximation need to be assessed prior to AVA inversion (Yilmaz, 2001). Secondly, rocks often are often weakly anisotropic due to preferred orientation of features such as the presence of clay minerals and cracks (Hornby et al., 1994; Thomsen, 1993). However, this is beyond the scope of this thesis since they would severely increase the complexity of the modelling and the inversion.

Inversion tests from AVA data to saturation and porosity using either Aki-Richards approximation or the full Zoeppritz equations were performed. The accuracy of the estimates depended on the relative contrasts in elastic properties as well as the sensitivity of the effective elastic reservoir properties for varying saturation and porosity. It was found that it is generally safer to use the Zoeppritz equations for both water saturation and porosity. However, Aki-Richards approximation gave satisfactory results for porosity estimates in a less computationally expensive manner. The sensitivity of the effective

elastic reservoir properties with varying saturation and porosity pose a major uncertainty in this analysis. Another choice of rock physics model would change the outcome. Also, for a given rock physics model, the static reservoir parameters provide a second complication as one would expect uncertainties associated with spatial variability and measurement errors. This was demonstrated for a reservoir with variable crack density.

Finally, two-step inversion procedures were tested on AVA data that had been modelled for a stratified elastic earth model with a reservoir section. The first inversion step was from AVA data to effective elastic reservoir parameters and the second inversion step was from effective elastic reservoir parameters to water saturation and porosity. Prior models were therefore included as additional information into the objective functions. The inversions were then successful for the two lowest noise levels. A Bayesian two-step inversion algorithm provided an excellent framework for statistical analysis. However, it is not always feasible to justify characterizing the prior information probabilistically. The classical approach to a two-step algorithm was a viable alternative, but it does not provide the same framework for statistical analysis of the inversion results. There also exists methods for assessing confidence intervals for the inverted model in a classical interpretation of uncertainty (Aster et al., 2005). However, the bias introduced by the regularization may cause us to severely underestimate the uncertainty (Van Wijk et al., 2002). Also, where the classical approach requires a separate analysis, all questions about model resolution are answered by the posterior PDFs in a Bayesian setting.

7.2 Suggestions for further work

A suggestion for further work would be to incorporate shear and mode converted waves into a joint AVA inversion procedure for rock physics parameters. A further aim could be to extend a two-step inversion algorithm to time-lapse AVA inversion for changes in saturation and pressure. Alternatively joint inversion of PP-reflection AVA data and CSEM data for determination of saturation and porosity could have been investigated. Also, it would be interesting to implement a rock physical model that incorporates second order effects.

Bibliography

Aki, K. and P. Richards (1980). *Quantative seismology: Theory and methods*, Volume 2. Freeman and Company.

Aster, R., B. Borchers, and C. Thurber (2005). *Parameter estimation and inverse problems*. International Geophysics Series 90. Elsevier Academic Press.

Auld, B. (1990). *Acoustic fields and waves in solids* (2 ed.), Volume 2. RE Krieger.

Avseth, P., T. Mukerji, and G. Mavko (2005, March). *Quantitative seismic interpretation*, Volume 1. Cambridge University Press.

Baig, A. and F. Dahlen (2004). Traveltime biases in random media and the s-wave discrepancy. *Geophysical Journal International 158*(3), 922–938.

Berryman, J. G. (1980). Long-wavelength propagation in composite elastic media i. spherical inclusions. *The Journal of the Acoustical Society of America 68*, 1809.

Biot, M. (1956). Theory of propagation of elastic waves in a fluid-saturated porous solid. ii. higher frequency range. *The Journal of the Acoustical Society of America 28*(2), 179–191.

Bortfeld, R. (1961). Approximations to the reflection and transmission coefficients of plane longitudinal and transverse waves*. *Geophysical Prospecting 9*(4), 485–502.

Bruggeman, V. D. (1935). Berechnung verschiedener physikalischer konstanten von heterogenen substanzen. i. dielektrizitätskonstanten und leitfähigkeiten der mischkörper aus isotropen substanzen. *Annalen der Physik 416*(7), 636–664.

Budansky, B. (1965). On the elastic moduli of some heterogenous materials. *J. Mech. Phys. Solids 14*, 223–227.

Buland, A. and Y. El Ouair (2006). Bayesian time-lapse inversion. *Geophysics 71*(3), R43–R48.

Buland, A. and H. Omre (2003). Bayesian linearized avo inversion. *Geophysics 68*(1), 185–198.

Dahl, T. and B. Ursin (1991). Parameter estimation in a one-dimensional anelastic medium. *Journal of Geophysical Research: Solid Earth 96*(B12), 20217–20233.

De Haas, J. and A. Berkhout (1988). On the information content of pp, p-sv, sv-sv, and sv-p reflections. In *SEG Annual Meeting*.

Downton, J. and C. Ursenbach (2006). Linearized amplitude variation with offset (avo) inversion with supercritical angles. *Geophysics 71*(5), E49–E55.

Drufuca, G. and A. Mazzotti (1995). Ambiguities in avo inversion of reflections from a gas-sand. *Geophysics 60*(1), 134–141.

Eshelby, J. (1957). The determination of the elastic field of an ellipsoidal inclusion, and related problems. *Proceedings of the Royal Society of London. Series A. Mathematical and Physical Sciences 241*(1226), 376–396.

Fatti, J. L., G. C. Smith, P. J. Vail, P. J. Strauss, and P. R. Levitt (1994). Detection of gas in sandstone reservoirs using avo analysis: A 3-d seismic case history using the geostack technique. *Geophysics 59*(9), 1362–1376.

Gassmann, F. (1951). Elastic waves through a packing of spheres. *Geophysics 16*(4), 673–685.

Gouveia, W. and J. Scales (1998). Bayesian seismic waveform inversion: Parameter estimation and uncertainty analysis. *Journal of Geophysical Research 103*, 2759–2779.

Guéguen, Y. and V. Palciauskas (1994). *Introduction to the Physics of Rocks*. Princeton University Press.

Hill, R. (1963). Elastic properties of reinforced solids: some theoretical principles. *Journal of the Mechanics and Physics of Solids 11*(5), 357–372.

Hornby, B., L. Schwartz, and J. Hudson (1994). Anisotropic effective-medium modeling of the elastic properties of shales. *Geophysics 59*(10), 1570–1582.

Hudson, J. (1991). Overall properties of heterogeneous material. *Geophysical journal international 107*(3), 505–511.

Hudson, J. and L. Knopoff (1989). Predicting the overall properties of composite materials with small-scale inclusions or cracks. *Pure and Applied Geophysics 131*(4), 551–576.

Jakobsen, M., J. Hudson, and T. Johansen (2003). T-matrix approach to shale acoustics. *Geophysical Journal International 154*(2), 533–558.

Larsen, M. (2010). Inversjon av syntetiske og reelle 4d-seismiske data med hensyn på trykk- og meningseffekter. Master's thesis, Institutt for geovitenskap, Universitetet i Bergen.

Lörtzer, G. and A. Berkhout (1992). An integrated approach to lithologic inversion-part i: Theory. *Geophysics 57*(2), 233–244.

Mæland, E. (2005). *Signalteori* (3rd ed.). Institutt for den faste jords fysikk, UiB.

Martinez, R. D. and G. A. McMechan (1991). τ-p seismic data for viscoelastic media - part 2: Linearized inversion. *Geophysical Prospecting 39*(2), 157–181.

Mavko, G., T. Mukerji, and J. Dvorkin (2003). *The rock physics handbook: Tools for seismic analysis of porous media*. Cambridge University Press.

Menke, W. (2012). *Geophysical data analysis: discrete inverse theory* (3rd ed.). Academic press.

Morozov, V. A., Z. Nashed, and A. Aries (1984). *Methods for solving incorrectly posed problems*. Springer-Verlag New York.

Ryan, H. (1994, September). Ricker, ormsby; klander, butterworth -a choice of wavelets. *CSEG Recorder*, 8–9.

Sambridge, M. and K. Mosegaard (2002). Monte carlo methods in geophysical inverse problems. *Rev. Geophys 40*(3), 1009.

Sayers, C. M. (1994). The elastic anisotropy of shales. *Journal of Geophysical Research: Solid Earth 99*, 767–774.

Scales, J. A. and R. Sneider (1997). To bayes or not to bayes? *Geophysics 62*(4), 1045–1046.

Shuey, R. (1985). A simplification of the zoeppritz equations. *Geophysics 50*(4), 609–614.

Smith, G. and P. Gidlow (1987). Weighted stacking for rock property estimation and detection of gas*. *Geophysical Prospecting 35*(9), 993–1014.

Stolt, R. and A. Weglein (1985). Migration and inversion of seismic data. *Geophysics 50*(12), 2458–2472.

Tarantola, A. (2005). *Inverse problem theory and methods for model parameter estimation*. Society for Industrial Mathematics.

Thomsen, L. (1993). *Weak anisotropic reflections*, Volume 8 of *Investigations in Geophysics*. Society of Exploration Geophysicists.

Tod, S. (2002). The effects of stress and fluid pressure on the anisotropy of interconnected cracks. *Geophysical Journal International 149*(1), 149–156.

Torquato, S. (2002). *Random heterogeneous materials: microstructure and macroscopic properties*, Volume 16 of *Interdisciplinary applied mathematics*. Springer-Verlag New York, Inc.

Van Wijk, K., J. Scales, W. Navidi, and L. Tenorio (2002). Data and model uncertainty estimation for linear inversion. *Geophysical Journal International 149*(3), 625–632.

Wood, A. (1955). *A textbook of sound: being an account of the physics of vibrations with special reference to recent theoretical and technical developments*. Bell and Sons.

Yilmaz, Ö. (2001). *Seismic data analysis: processing, inversion, and interpretation of seismic data*. Number 10 in Investigations in Geophysics. SEG Books.

Zoeppritz, K. (1919). Erdbebenwellen vii. *Nachrichten von der Gesellschaft der Wissenschaften zu Göttingen, Mathematisch-Physikalische Klasse 1919*, 57–65.

Appendix A

Matlab scripts

The scripts that have been used in this thesis have been coded in Matlab. The majority of them have been coded by the author with some exemptions: I wish to thank Associate Professor Henk Keers for the script for plotting the seismogram and the script for calculating Gaussian autocorrelations (not included). Further, Professor Morten Jakobsen have contributed with a script for calculating the G-tensor, 'G_iso', and the isotropic average, 'iso_av'. Finally, the script to compute discrete derivative operators, 'get_l', have been coded by Per Christian Hansen.

A.1 Rock physics modelling

```
function [Vp_eff,Vs_eff,rho_eff]= effective_properties(P_d,v1,S_f1,K_f1,...
    rhof1,K_f2,rhof2)

%QUARTZ MATRIX
K0 = 37E9;%Pa
my0 = 16.6E9;%Pa
rho0 = 2670.6;%kg/m^3
ap_c=0.001;%initial aspect ratio of cracks
ap_p=1;%aspect ratio of pores
poisson= (3*K0-2*my0)/(6*K0+2*my0);
P_0 = 18.8E6;%reference differential pressure
eps_0 = 0.9;%crack density at zero differential pressure
epsilon = eps_0*exp(-(P_d/(P_0)));

%FRAME MODULI
c11 = K0+(4/3)*my0;
c44 = my0;
c12 = c11-2*c44;
I= eye(6);
c0 = [c11 c12 c12 0 0 0;
    c12 c11 c12 0 0 0;
    c12 c12 c11 0 0 0;
    0 0 0 2*c44 0 0;
    0 0 0 0 2*c44 0;
```

```
    0 0 0 0 0 2*c44];%2 factor for matrix inversion
s0 = inv(c0);
G1= G_iso(c0,ap_p,poisson);
k1= iso_av((I+G1*c0)\s0);
G2= G_iso(c0,ap_c,poisson);
k2 = iso_av((I+G2*c0)\s0);
v2 = (4/3)*pi*epsilon*ap_c;%crack volume (very small)
fi = v1 + v2;%total porosity
s_eff= s0+v1*k1+v2*k2;
c_eff= inv(s_eff);
%frame moduli(see. AULD p. 169)
my= c_eff(4,4)/2;
K= c_eff(1,1)-(4/3)*my;

%UNDRAINED MODULI
%Wood (p.176 Rock Physics handbook)
S_f2= 1-S_f1;
K_f = 1/((S_f1/K_f1)+(S_f2/K_f2));
rho_f = rhof1*S_f1+rhof2*S_f2;
%Gassmann
alfa= 1-(K/K0);
K_u= K+((alfa^2)/((fi/K_f)+((alfa-fi)/K0)));
%my undrained is identical to the frame moduli

%EFFECTIVE PROPERTIES
rho_eff= rho0*(1-fi)+rho_f*fi;
Vp_eff=sqrt((K_u+(4/3)*my)/rho_eff);
Vs_eff=sqrt(my/rho_eff);

%
% input  - stiffness tensor C
%        - aspect ratio a
%        - poisson ratio v
%
% return - G tensor
%

function ans = G_iso(C,a,v)

if a==1
    S11 = ((5*v-1)/15*(1-v))*(1)+((4-5*v)/(15*(1-v)))*(2);
    S33 = ((5*v-1)/15*(1-v))*(1)+((4-5*v)/(15*(1-v)))*(2);
    S12 = ((5*v-1)/15*(1-v))*(1);
    S13 = ((5*v-1)/15*(1-v))*(1);
    S31 = ((5*v-1)/15*(1-v))*(1);
    S66 = ((4-5*v)/(15*(1-v)));
    S44 = ((4-5*v)/(15*(1-v)));
else
    b = (a*a)/(a*a-1);
    q = (a/((1-a*a)^(3/2)))*(acos(a)-a*(sqrt(1-a*a)));
    S11 = (3/(8*(1-v)))*b+(1/(4*(1-v)))*(1-2*v-(9/(4*(a*a-1))))*q;
    S33 = (1/(2*(1-v)))*(1-2*v+(3*a*a-1)/(a*a-1)-(1-2*v+3*b)*q);
```

```
    S12 = (1/(4*(1-v)))*((1/2)*b-(1-2*v+(3/(4*(a*a-1))))*q);
    S13 = (1/(2*(1-v)))*(-b+(1/2)*(3*b-(1-2*v))*q);
    S31 = (1/(2*(1-v)))*(2*v-1-1/(a*a-1)+(1-2*v+(3/(2*(a*a-1))))*q);
    S66 = (1/(4*(1-v)))*((1/2)*b+(1-2*v-(3/(4*(a*a-1))))*q);
    S44 = (1/(4*(1-v)))*(1-2*v-((a*a+1)/(a*a-1))-(1/2)*(1-2*v-3*((a*a+1)/(a*a-1)))*q);
end


S=[
S11 S12 S13 0   0   0;
S12 S11 S13 0   0   0;
S31 S31 S33 0   0   0;
0   0   0   2*S44 0   0;
0   0   0   0   2*S44 0;
0   0   0   0   0   2*S66;
];

ans = -S*inv(C);
```

```
function ans = iso_av(t);

% February 1, 2001.
% Input is a fourth-rank tensor t
% Output is the orientation avarage of the tensor t.

lambda = (t(1,1)+t(3,3)+5*t(1,2)+8*t(1,3)-2*t(4,4))/15;
mu = (7*t(1,1)+2*t(3,3)-5*t(1,2)-4*t(1,3)+6*t(4,4))/30;
c11 = lambda + 2*mu;
c12 = lambda;
c44 = mu;
ans = [
   c11 c12 c12 0     0     0;
   c12 c11 c12 0     0     0;
   c12 c12 c11 0     0     0;
   0   0   0   2*c44 0     0;
   0   0   0   0     2*c44 0;
   0   0   0   0     0     2*c44;
];
```

A.2 AVA modelling and one-step inversion

```
%Nonlinear Bayesian inversion with an uninformative prior for saturation
%and porosity

%MODEL PARAMETERS
dt=0.004;%sampling interval(sec)
NR = 0.05;%noise as percentage of max amplitude
theta = 0:2:40;
NA = length(theta);
```

```
dfi = 0.0025;
fi_p = 0:dfi:0.4;
dSw=0.025;
Sw=0:dSw:1;
Pd = 2E6;
fluids = struct('water',{2173.9E6 997.9},'gas',{35.9E6 221.5},...
    'oil',{409.85E6 671});
[K_f1,rhof1] = fluids.water;
[K_f2,rhof2] = fluids.oil;
[K_f3,rhof3] = fluids.gas;

%Overburden
vp_s = 3150;
vs_s = 1900;
rho_s = 2500;

%ROCK PHYSICS FORWARD MODELLING
N = length(fi_p);
M = length(Sw);
%oil and water
vp = zeros(N,M);
vs = zeros(N,M);
rho = zeros(N,M);
%gas and water
vp2 = zeros(N,M);
vs2 = zeros(N,M);
rho2 = zeros(N,M);
for n = 1:N
    for m = 1:M
        [vp(n,m),vs(n,m),rho(n,m)] = effective_properties(Pd,...
            fi_p(n),Sw(m),K_f1,rhof1,K_f2,rhof2);
        [vp2(n,m),vs2(n,m),rho2(n,m)] = effective_properties(Pd,...
            fi_p(n),Sw(m),K_f1,rhof1,K_f3,rhof3);
    end
end

%(plot variations of elastic parameters with saturation and porosity)

%Variations of reflection coefficients with saturation and porosity
%for fixed angles
N = length(fi_p);
M = length(Sw);
for n = 1:N
    for m = 1:M
    vp_trial = [vp_s vp(n,m)];
    vs_trial = [vs_s vs(n,m)];
    rho_trial = [rho_s rho(n,m)];
    vp_trial2 = [vp_s vp2(n,m)];
    vs_trial2 = [vs_s vs2(n,m)];
    rho_trial2 = [rho_s rho2(n,m)];
```

```
    %oil and water
    [raki_near(n,m),rzoepp_near(n,m)] = getreflection(theta(1),vp_trial...
        ,vs_trial,rho_trial);
    [raki_mid(n,m),rzoepp_mid(n,m)] = getreflection(theta(11),vp_trial...
        ,vs_trial,rho_trial);
    [raki_far(n,m),rzoepp_far(n,m)] = getreflection(theta(21),vp_trial...
        ,vs_trial,rho_trial);
    %gas and water
    [raki_near2(n,m),rzoepp_near2(n,m)] = getreflection(theta(1),...
        vp_trial2,vs_trial2,rho_trial2);
    [raki_mid2(n,m),rzoepp_mid2(n,m)] = getreflection(theta(11)...
        ,vp_trial2,vs_trial2,rho_trial2);
    [raki_far2(n,m),rzoepp_far2(n,m)] = getreflection(theta(21)...
        ,vp_trial2,vs_trial2,rho_trial2);
    end
end
%(plot variations of reflection coefficients with saturation and porosity
%for fixed angles here)

%LOOP OVER SELECTED CASES
for sat_index = [5 21 39]
    for phi_index = [41 121]

        %velocity models
        vp_o = [vp_s vp(phi_index,sat_index)];
        vs_o = [vs_s vs(phi_index,sat_index)];
        rho_o = [rho_s rho(phi_index,sat_index)];

        vp_g = [vp_s vp2(phi_index,sat_index)];
        vs_g = [vs_s vs2(phi_index,sat_index)];
        rho_g = [rho_s rho2(phi_index,sat_index)];

        %reflection coefficients
        thetao = asind(vp_o(1)/vp_o(2));
        I = theta <=thetao;
        thetao = theta(I);
        NA = length(thetao);
        [raki_o,rzoepp_o] = getreflection(thetao,vp_o,vs_o,rho_o);
        rpp_o = rzoepp_o(1:NA);
        rppaki_o = raki_o(1:NA);
        drpp_o = (rpp_o-rppaki_o)./rpp_o*100;

        thetag = asind(vp_g(1)/vp_g(2));
        I = theta <=thetag;
        thetag = theta(I);
        NA2 = length(thetag);
        [raki_g,rzoepp_g] = getreflection(thetag,vp_g,vs_g,rho_g);
        rpp_g = rzoepp_g(1:NA2);
        rppaki_g = raki_g(1:NA2);
        drpp_g = (rpp_g-rppaki_g)./rpp_g*100;
```

```
        %(plot comparisons of reflections coefficients here)

        %BAYESIAN INFERENCE
        %oil and water pore fluid
        %add noise
        std_inv = NR*abs(rpp_o);
        %data covariance matrix
        Cd_o = diag(std_inv.^-2);
        %MARGINAL DISTRIBUTIONS: Uninformative prior, but known overburden
        [m1aki_o,m2aki_o,m1zoepp_o,m2zoepp_o,postaki_o,postzoepp_o] =...
            getmarginals2(rpp_o,Cd_o,fi_p,Sw,thetao,vp_o,vs_o...
            ,rho_o,vp,vs,rho);
        %gas and water pore fluid
        %add noise
        std_inv = NR*rpp_g;
        %data covariance matrix
        Cd_g = diag(std_inv.^-2);
        %MARGINAL DISTRIBUTIONS: Uninformative prior, but known overburden
        [m1aki_g,m2aki_g,m1zoepp_g,m2zoepp_g,postaki_g,postzoepp_g] = ...
            getmarginals2(rpp_g,Cd_g,fi_p,Sw,thetag,vp_g...
            ,vs_g,rho_g,vp2,vs2,rho2);

        %(plot posterior and marginal PDFs here)

    end
end

function [raki,rzoepp] = getreflection(theta,vp,vs,rho)

NA=length(theta);
vs_ave = 0.5*(vs(1)+vs(2));
vp_ave = 0.5*(vp(1)+vp(2));
rho_ave= 0.5*(rho(1)+rho(2));
vp_diff= vp(2)-vp(1);
vs_diff= vs(2)-vs(1);
rho_diff= rho(2)+rho(1);
ave = vs_ave/vp_ave;
ave_sq = ave^2;

%Make empty arrays
A_11 = zeros(NA,1);
A_12 = zeros(NA,1);
A_13 = zeros(NA,1);
A = cell(1,3);
rpp = zeros(NA,1);
for n=1:NA
    %AKI-RICHARDS
    A_11(n) = 0.5*(1+(tand(theta(n)))^2);%App - vp
    A_12(n) = -4*ave_sq*(sind(theta(n))^2);%App - vs
    A_13(n) = 0.5*(1-4*ave_sq*(sind(theta(n))^2));%App - rho

    %Solve the Zoeppritz equations for an incident angle
```

```
    coeff = zoeppritz(theta(n),rho(1),rho(2),vs(1),vs(2),vp(1),vp(2));
    rpp(n) = coeff(1);
end

A{1,1} = A_11;
A{1,2} = A_12;
A{1,3} = A_13;
A = cell2mat(A);
%TRUE DATA
c=[vp_diff/vp_ave; vs_diff/vs_ave; rho_diff/rho_ave];%contrast vector
raki = A*c;
rzoepp = [rpp;];

%The medium parameters for the layers above and below the interface are
%input to the function. It will return the corresponding reflection and
%transmission coefficients. See Auld

function coeff=zoeppritz(theta,rho1,rho2,v_s1,v_s2,v_p1,v_p2)
theta = theta/180*pi;
%REFLECTED AND TRANSMITTED ANGLES FOR INCIDENT P-WAVE
%reflected p-wave
theta_l1 = theta;
%reflected s-wave
theta_s1 = asin((v_s1/v_p1)*sin(theta));
%transmitted p-wave
theta_l2 = asin((v_p2/v_p1)*sin(theta));
%transmitted s-wave
theta_s2 = asin((v_s2/v_p1)*sin(theta));

%ZOEPPRITZ MATRIX
A = zeros(4,4);
%The Zoeppritz matrix for a P incident wave is identical to the matrix for
%an incident SV wave.
Z1 = rho1*v_p1;
Z2 = rho2*v_p2;
W1 = rho1*v_s1;
W2 = rho2*v_s2;
a1 = (v_p1/v_s1);
b1 = v_s2*v_p1*W2/(v_p2*v_s1*W1);
c1 = v_p1*W2/(v_s1*W1);
a2 = v_s1/v_p1;
b2 = Z2/Z1;
c2 = W2/Z1;

A(1,1) = sin(theta_l1);
A(1,2) = cos(theta_s1);
A(1,3) = -sin(theta_l2);
A(1,4) = cos(theta_s2);
A(2,1) = cos(theta_l1);
A(2,2) = -sin(theta_s1);
A(2,3) = cos(theta_l2);
A(2,4) = sin(theta_s2);
```

```
A(3,1) = sin(2*theta_l1);
A(3,2) = a1*cos(2*theta_s1);
A(3,3) = b1*sin(2*theta_l2);
A(3,4) = -c1*cos(2*theta_s2);
A(4,1) = cos(2*theta_s1);
A(4,2) = -a2*sin(2*theta_s1);
A(4,3) = -b2*cos(2*theta_s2);
A(4,4) = -c2*sin(2*theta_s2);
%The left hand side of the equations from the boundary conditions differ
%from the SV wave
b_p =[-sin(theta_l1);
    cos(theta_l1);
    sin(2*theta_l1);
    -cos(2*theta_s1)];

%REFLECTION AND TRANSMISSION COEFFICIENTS
%p-ref,s-ref,p-trans,s-trans
coeff= A\b_p;

function [m1aki,m2aki,m1zoepp,m2zoepp,postaki,postzoepp] =getmarginals2(...
    rpp,Cd_inv,m1,m2,theta,vp_true,vs_true,rho_true,vp,vs,rho)

%make empty arrays
N = length(m1);%porosities
M = length(m2);%saturations
NA = length(theta);%angles
J1 = zeros(N,M);
J2 = zeros(N,M);
obj1 = zeros(N,M);
obj2 = zeros(N,M);

for n = 1:N
    for m = 1:M
        %elastic model
        vp_trial = [vp_true(1) vp(n,m)];
        vs_trial = [vs_true(1) vs(n,m)];
        rho_trial = [rho_true(1) rho(n,m)];
        %reflection coefficients
        [raki_trial,rzoepp_trial] = getreflection(theta,vp_trial,...
            vs_trial,rho_trial);
        rppaki_trial = raki_trial(1:NA);
        rpp_trial = rzoepp_trial(1:NA);
        %Objective function for Aki-Richards
        J1(n,m) = 1/2*((rppaki_trial-rpp)'*Cd_inv*...
            (rppaki_trial-rpp));
        obj1(n,m) = exp(-J1(n,m));
        %Objective function exact Zoeppritz
        J2(n,m) = 1/2*((rpp_trial-rpp)'*Cd_inv*...
            (rpp_trial-rpp));
        obj2(n,m) = exp(-J2(n,m));

    end
```

```
end
%numerical integration according to the trapezoidal rule
%define the integration intervals
b1 = max(m1);
a1 = min(m1);
b2 = max(m2);
a2 = min(m2);
h1 = (b1-a1)/(N-1);%porosity partitions
h2 = (b2-a2)/(M-1);%saturation partitions

%the first objective function
int1 = h1/2*sum(obj1(2:N,:)+obj1(1:(N-1),:),1);%integrate over porosity
int2 = h2/2*sum(int1(1,2:M)+int1(1,1:(M-1)),2);%integrate over saturation
const1 = 1/int2;
postaki = const1*obj1;
%the second objective function
int1 = h1/2*sum(obj2(2:N,:)+obj2(1:(N-1),:),1);%integrate over porosity
int2 = h2/2*sum(int1(1,2:M)+int1(1,1:(M-1)),2);%integrate over saturation
const2 = 1/int2;
postzoepp = const2*obj2;

%marginal distribution of saturation
m2aki = const1.*h1/2*sum(obj1(2:N,:)+obj1(1:(N-1),:),1);
%marginal distribution of porosity
m1aki = const1.*h2/2*sum(obj1(:,2:M)+obj1(:,1:(M-1)),2);

%marginal distribution of saturation
m2zoepp = const2.*h1/2*sum(obj2(2:N,:)+obj2(1:(N-1),:),1);
%marginal distribution of porosity
m1zoepp = const2.*h2/2*sum(obj2(:,2:M)+obj2(:,1:(M-1)),2);

%DEFINE THE SPATIAL VARIABILITY OF THE ROCK PHYSICS PARAMETERS
dt=0.004;%sampling interval(sec)
NR = 0.05;%noise as percentage of max amplitude
theta = 0:2:40;
NA = length(theta);

nn = 51;
x = linspace(0,1040,nn);
y = linspace(0,-1040,nn);
[X Y] = meshgrid(x,y);
fluids = struct('water',{2173.9E6 997.9},'gas',{35.9E6 221.5},...
    'oil',{409.85E6 671});
[K_f1,rhof1] = fluids.water;
[K_f2,rhof2] = fluids.oil;
[K_f3,rhof3] = fluids.gas;
rphi = 0.3;
reps = 0.8533;
nres = nn-1;
phi_res = gaussianphi(rphi,nres);
cracd_res = gaussianeps(reps,nres);
Sw_res = cracd_res;
```

```
dummy = Sw_res >= reps;
dummy2 = Sw_res < reps;
dummy = dummy*0.1;
dummy2 = dummy2*0.5;
Sw_res = dummy + dummy2;

%DISCRITIZE THE MODEL SPACE
dphi = 0.005;
phii = 0:dphi:0.4;
dSw=0.025;
Swi=0:dSw:1;
K = length(phii);
L = length(Swi);
vp2 = zeros(K,L);
vs2 = zeros(K,L);
rho2 = zeros(K,L);
for k = 1:K;
    for l = 1:L
    [vp2(k,l),vs2(k,l),rho2(k,l)] = effective_properties2(reps,phii(k),...
        Swi(l),K_f1,rhof1,K_f2,rhof2);
    end
end
%FORWARD MODELLING
[N,M] = size(phi_res);
%velocity model with true crack density
vp = zeros(N,M);
vs = zeros(N,M);
rho = zeros(N,M);
%Overburden
vp_s = 3150;
vs_s = 1900;
rho_s = 2500;
Swa = zeros(N,M);
phia = zeros(N,M);
Swa2 = zeros(N,M);
phia2 = zeros(N,M);
Swz = zeros(N,M);
phiz = zeros(N,M);
Swz2 = zeros(N,M);
phiz2 = zeros(N,M);
parfor n = 1:N
    for m = 1:M
        %ROCK PHYSICS
        [vp(n,m),vs(n,m),rho(n,m)] = effective_properties2(cracd_res(n,m),...
            phi_res(n,m),Sw_res(n,m),K_f1,rhof1,K_f2,rhof2);
        %AVA
        vpm = [vp_s vp(n,m)];
        vsm = [vs_s vs(n,m)];
        rhom = [rho_s rho(n,m)];
        [raki,rzoepp] = getreflection(theta,vpm,vsm,rhom);
        %THE INVERSION
```

```
        std = NR*abs(rzoepp);
        %data covariance matrix
        Cd_inv = diag(std.^-2);
        % inversions with constant crack density
        [phia(n,m),Swa(n,m),phiz(n,m),Swz(n,m)] = getmap(rzoepp,raki,...
            Cd_inv,phii,Swi,theta,vp_s,vs_s,rho_s,vp2,vs2,rho2);
        % inversions with variable crack density
        [phia2(n,m),Swa2(n,m),phiz2(n,m),Swz2(n,m)] = getmap2(rzoepp,...
            raki,Cd_inv,phii,Swi, theta,vp_s,vs_s,rho_s,...
            cracd_res(n,m),K_f1,rhof1,K_f2,rhof2);
    end
end
```

A.3 Waveform forward modelling

```
%ACQUISITION PARAMETERS
dt = 0.002;%data sampling interval(sec)
f0 = 30;%Hz
theta = 0:2:40;
PMA = [10E-5 10E-4 10E-3];

%THE MODEL DISCRETIZATION
dfi = 0.0025;
fi = 0:dfi:0.4;
dSw=0.025;
Sw=0:dSw:1;
fluids = struct('water',{2173.9E6 997.9},'gas',{35.9E6 221.5},...
    'oil',{409.85E6 671});
dz=10;
z = 0:dz:1000;
NZ = length(z);
VP = zeros(NZ,1);
VS = zeros(NZ,1);
RHO = zeros(NZ,1);

%THE RESERVOIR PARAMETERS
[K_f1,rhof1] = fluids.water;
[K_f2,rhof2] = fluids.oil;
P_d = 2E6;
fi_p = 121;%index pore porosity
Sw_true = 39;%index water saturation

%ROCK PHYSICS FORWARD MODELLING
N = length(fi);
M = length(Sw);
for n = 1:N
    for m = 1:M
        [vp(n,m),vs(n,m),rho(n,m)] = effective_properties2(P_d,...
            fi(n),Sw(m),K_f1,rhof1,K_f2,rhof2);
    end
```

```
end

%THE ELASTIC MODEL IN DEPTH
VP(1:30) = 3050;
VS(1:30) = 1800;
RHO(1:30) = 2470;
VP(31:50) = 3120 + 30/40*[1:20];
VS(31:50) = 1870 + 30/40*[1:20];
RHO(31:50) = 2490 + 10/40*[1:20];
VP(51:91) = vp(fi_p,Sw_true);
VS(51:91) = vs(fi_p,Sw_true);
RHO(51:91) = rho(fi_p,Sw_true);
VP(92:end) = 3120;
VS(92:end) = 1870;
RHO(92:end) = 2490;

%THE ELASTIC MODEL IN TIME
T = zeros(NZ,1);
delta_t= dz./(0.5*(VP(1:NZ-1)+VP(2:NZ)));%travel time through each grid block
T(2:end) = cumsum(delta_t,1);%cumulative traveltime for each grid point

%(PLOT THE ELASTIC MODEL IN TIME)

%interpolate from T to t
NT = ceil(max(max(T))/dt +1);%number of time steps for our sampling interval
t = 0:dt:(NT-1)*dt;%time vector with a constant sampling interval in time
vpi = interp1(T,VP,t','nearest','extrap');
vsi = interp1(T,VS,t','nearest','extrap');
rhoi = interp1(T,RHO,t','nearest','extrap');

%The model parameters
m = [log(vpi)' log(vsi)' log(rhoi)']';

%COMPUTE THE DIFFERENCE MATRIX
D = block_l(NT,3);

%WEAK CONTRAST REFLECTION COEFFICIENT APPROXIMATION

%Find the incident angles for each reflector
NA=length(theta);
%Calculate the coefficients that depend on the background model
aa=(vsi./vpi).^2;

%Make empty arrays and matrices
A = cell(NA,3);
%Diagonal matrices
A_vp = zeros(NT,NT-1);
A_vs = zeros(NT,NT-1);
A_rho = zeros(NT,NT-1);

for n=1:NA;
```

```
    %First layer
    for nt = 1:NT-1
        A_vp(nt,nt) = 0.5*(1+(tand(theta(n)))^2);
        A_vs(nt,nt) = -4*aa(nt)*(sind(theta(n))^2);
        A_rho(nt,nt) = 0.5*(1-4*aa(nt)*(sind(theta(n))^2));
    end
    %Store in cell array
    A{n,1} = sparse(A_vp);
    A{n,2} = sparse(A_vs);
    A{n,3} = sparse(A_rho);

end
A = cell2mat(A);

%B. D. WAVELET MATRIX
W = blockwavelet(dt,f0,NT,NT,NA);
W = full(W);

%THE CONVOLUTION
%Multi-trace convolutional model with block matrices
r_true = A*D*m;
G = (W*A*D);
d_aki = G*m;

%PLOT THE SEISMOGRAMS
plotseismograms(d_aki,theta,dt)

function [L,W] = get_l(n,d)
%GET_L Compute discrete derivative operators.
%
% [L,W] = get_l(n,d)
%
% Computes the discrete approximation L to the derivative operator
% of order d on a regular grid with n points, i.e. L is (n-d)-by-n.
%
% L is stored as a sparse matrix.
%
% Also computes W, an orthonormal basis for the null space of L.

% Per Christian Hansen, IMM, 02/05/98.

% Initialization.
if (d<0), error ('Order d must be nonnegative'), end

% Zero'th derivative.
if (d==0), L = speye(n); W = zeros(n,0); return, end

% Compute L.
c = [-1,1,zeros(1,d-1)];
nd = n-d;
for i=2:d, c = [0,c(1:d)] - [c(1:d),0]; end
```

```
L = sparse(nd,n);
for i=1:d+1
  L = L + sparse(1:nd,(1:nd)+i-1,c(i)*ones(1,nd),nd,n);
end

% If required, compute the null vectors W via modified Gram-Schmidt.
if (nargout==2)
  W = zeros(n,d);
  W(:,1) = ones(n,1);
  for i=2:d, W(:,i) = W(:,i-1).*(1:n)'; end
  for k=1:d
     W(:,k) = W(:,k)/norm(W(:,k));
     W(:,k+1:d) = W(:,k+1:d) - W(:,k)*(W(:,k)'*W(:,k+1:d));
  end
end
```

```
function W = blockwavelet(dt,f0,NT,NM,NA)
%Make an array for the non-empty diagonal blocks. Copy the contents of the
%linear convolution matrix onto each of the cells. Then make a block
%diagonal array of them.
wavelet = ricker(dt,f0);
NR = length(wavelet);
conv_mat = zeros((NR+NT)-1,NM);%Linear convolution matrix. Extend the
%shortest time series with zeros
for k = 1:(NM)
    j = NR+(k-1);
    conv_mat(k:j,k) = wavelet';
end
W = cell(1,NA);
[W{:}] = deal(sparse(conv_mat));
W = blkdiag(W{:});
```

```
function wavelet=ricker(dt,f0)

%f0=center frequency of the source (Hz)
%dt sampling interval

%parameters
T=0.5;
b=(sqrt(6)/pi)/f0;%breadth of ricker wavelet (ms)
t=0:dt:T;

%output
ricker=(1-2*pi^2*f0^2.*(t-b).^2).*exp(-pi^2*f0^2*(t-b).^2);
%Keep nonzero components of source wavelet
m=0;
l=1;
while m==0
    if abs(ricker(l))<0.0001 && abs(ricker(l+1))<0.0001
        last_index=l-1;
        m=1;
    end
```

```
    l=l+1;
end
%output
wavelet=ricker(1:last_index);
```

A.4 Two-step inversion algorithms

```
%TWO-STEP INVERSION
for nl = 1:length(PMA)

    %THE PRIOR MODEL
    P = polyfit(t',vpi,3);
    mu_vp = polyval(P,t');
    mu_vp = log(mu_vp);
    P = polyfit(t',vsi,3);
    mu_vs = polyval(P,t');
    mu_vs = log(mu_vs);
    P = polyfit(t',rhoi,3);
    mu_rho = polyval(P,t');
    mu_rho = log(mu_rho);
    mu_mp = [mu_vp' mu_vs' mu_rho']';
    %THE DATA UNCERTAINTIES
    var_n = (PMA(nl)*max(abs(d_aki)))^2;
    d_n = sqrt(var_n)*rand(size(d_aki));
    eta = norm(d_n);%norm of the error
    d_obs = d_aki+ d_n;

    %ZEROTH + SECOND ORDER TIKHONOV INVERSION WITH PRIOR
    L = block_l2(NT,3);%Roughening matrix
    J = 0.8;%Decay constant in regularization parameter
    NIT = 100;
    lam0 = zeros(NIT,1);
    lam1 = zeros(NIT,1);
    data_misfit = zeros(NIT,1);
    for iter = 1:NIT
        lam0(iter) = J^iter;
        lam1(iter) = 2*lam0(iter);
        m_bf = inv(G'*G + lam0(iter)^2*eye(size(G'*G)) + lam1(iter)^2*...
            L'*L)*(G'*d_obs + lam0(iter)^2*eye(size(G'*G))*mu_mp);
        data_misfit(iter) = norm(G*m_bf-d_obs);
        if eta >= data_misfit(iter)
            break
        end
    end
    %(plot resolution matrix and choice of regularization parameters)

    m_bf = exp(m_bf);
    m_bf = reshape(m_bf,NT,3);
    mu_mp = exp(mu_mp);
    mu_mp = reshape(mu_mp,NT,3);
```

```
    %(plot inverted elastic model)

    %INVERSION FROM ELASTIC EARTH MODEL TO SATURATION AND POROSITY
    I = find(vpi == vp(fi_p,Sw_true));
    II = round(median(I));%pick a sample in the middle of the reservoir
    m_res = m_bf(II,:);
    J = zeros(N,M);
    for n = 1:N
        for m = 1:M
            m_trial = [vp(n,m) vs(n,m) rho(n,m)]';
            %Objective function for Aki-Richards
            J(n,m) = 0.5*(m_trial-m_res')'*(m_trial-m_res');
        end
    end
    %find the minimum of the objective function
    [~,ind] = min(J(:));
    [k,l] = ind2sub(size(J),ind);
    fi_inv = fi(k)
    Sw_inv = Sw(l)
end

function L = block_l2(NT,no_m)
%GET_L Compute discrete derivative operators.

L = cell(1,no_m);
[diffmat,W] = get_l(NT,2);
[L{:}]=deal((diffmat));
L=blkdiag(L{:});
L = full(L);

%THE BAYESIAN INVERSION TWO-STEP
for nl = 1:3%loop over noise level
    % PRIOR INFORMATION
    P = polyfit(t',vpi,3);
    mu_vp = polyval(P,t');
    mu_vp = log(mu_vp);
    P = polyfit(t',vsi,3);
    mu_vs = polyval(P,t');
    mu_vs = log(mu_vs);
    P = polyfit(t',rhoi,3);
    mu_rho = polyval(P,t');
    mu_rho = log(mu_rho);
    mu_mp = [mu_vp' mu_vs' mu_rho']';
    var_mp = 0.05^2;
    C_mp = eye(length(mu_mp))*var_mp;

    %Observed data zero mean Gaussian noise
    var_n = (PMA(nl)*max(abs(d_aki)))^2;
    C_dobs = eye(length(d_aki))*(var_n);

    %THE FIRST INVERSION STEP
    %MAP solution
```

```
    C_mpinv = inv(C_mp);
    C_dinv = eye(length(d_aki))*(var_n).^-1;
    C_map = inv(G'*C_dinv*G + C_mpinv);
    m_map = (G'*C_dinv*G + C_mpinv)\(G'*C_dinv*d_aki + C_mpinv*mu_mp);

    %Confidence intervals
    %posterior
    var_map = diag(C_map);
    sigma_map = sqrt(var_map);
    dummy = abs(exp(m_map-1.96*sigma_map)-exp(m_map));
    confint = [exp(m_map-1.96*sigma_map) exp(m_map) exp(m_map+1.96*sigma_map)];
    confint_vp = confint(1:NT,:);
    confint_vs = confint((NT+1):2*NT,:);
    confint_rho = confint((2*NT+1):3*NT,:);
    %prior
    sigma_mp = sqrt(var_mp);
    dummy2 = abs(exp(mu_mp-1.96*sigma_mp)-exp(mu_mp));
    cimp = [exp(mu_mp-1.96*sigma_mp) exp(mu_mp) exp(mu_mp+1.96*sigma_mp)];
    cimp_vp = cimp(1:NT,:);
    cimp_vs = cimp((NT+1):2*NT,:);
    cimp_rho = cimp((2*NT+1):3*NT,:);

    %reduction in confidence intervals
    red_vp = (mean(dummy2(1:NT))-mean(dummy(1:NT)))...
        /mean(dummy2(1:NT))*100
    red_vs = (mean(dummy2((NT+1):2*NT))-mean(dummy((NT+1):2*NT)))/...
        mean(dummy2((NT+1):2*NT))*100
    red_rho = (mean(dummy2((2*NT+1):3*NT))-mean(dummy((2*NT+1):3*NT)))/...
        mean(dummy2((2*NT+1):3*NT))*100

    %THE SECOND INVERSION STEP
    I = find(vpi == vp(fi_p,Sw_true));
    II = round(median(I));%pick a sample in the middle of the reservoir
    var_res = (dummy/1.96).^2;
    var_res = reshape(var_res,NT,3);
    var_res = var_res(II,:);
    m_res = reshape(exp(m_map),NT,3);
    m_res = m_res(II,:);
    [posterior,Sw_marg,fi_marg] = getmarginals(vp,vs,rho,fi,Sw,m_res,...
        var_res);

    %(plot the MAP solution here)

    %(Plot posterior and marginal PDFs here)
end

function [posterior,Sw_marg,fi_marg] = getmarginals(vp,vs,rho,fi,Sw,...
    m_res,sigma_res)

%make empty arrays
N = length(fi);%porosities
M = length(Sw);%saturations
```

```
J = zeros(N,M);
obj1 = zeros(N,M);
Cd_inv = diag(sigma_res.^-1);
for n = 1:N
    for m = 1:M
        m_trial = [vp(n,m) vs(n,m) rho(n,m)]';
        %Objective function for Aki-Richards
        J(n,m) = 0.5*(m_trial-m_res')'*Cd_inv*(m_trial-m_res');
        obj1(n,m) = exp(-J(n,m));

    end
end
%numerical integration according to the trapezoidal rule
%define the integration intervals
b1 = max(fi);
a1 = min(fi);
b2 = max(Sw);
a2 = min(Sw);
h1 = (b1-a1)/(N-1);%porosity partitions
h2 = (b2-a2)/(M-1);%saturation partitions

%the first objective function
int1 = h1/2*sum(obj1(2:N,:)+obj1(1:(N-1),:),1);%integrate over porosity
int2 = h2/2*sum(int1(1,2:M)+int1(1,1:(M-1)),2);%integrate over saturation
const1 = 1/int2;
posterior = const1*obj1;

%marginal distribution of saturation
Sw_marg = const1.*int1;
%marginal distribution of porosity
fi_marg = const1.*h2/2*sum(obj1(:,2:M)+obj1(:,1:(M-1)),2);
```